UNIVERSIDADE ESTADUAL DE CAMPINAS
Faculdade de Engenharia Química

VITOR PIROVANI PAIXÃO

PROJETO DE UM REATOR DE DESLOCAMENTO GÁS-ÁGUA COM TROCA TÉRMICA INTEGRADA E USO DE CALOR RESIDUAL

SHIFT REACTOR DESIGN WITH INTEGRATED HEAT EXCHANGE AND WASTE HEAT USAGE

CAMPINAS
2022

VITOR PIROVANI PAIXÃO

PROJETO DE UM REATOR DE DESLOCAMENTO GÁS-ÁGUA COM TROCA TÉRMICA INTEGRADA E USO DE CALOR RESIDUAL

SHIFT REACTOR DESIGN WITH INTEGRATED HEAT EXCHANGE AND WASTE HEAT USAGE

Tese apresentada à Faculdade de Engenharia Química da Universidade Estadual de Campinas como parte dos requisitos para a obtenção do título de Doutor em Engenharia Química.

Thesis presented to the School of Chemical Engineering of the University of Campinas in partial fulfillment of the requirements for the degree of Doctor in Chemical Engineering

Advisor: Prof. Dr. José Vicente Hallak D'Angelo
Co-Advisor: Prof. Dr. Luís Fernando Mercier Franco

ESTE TRABALHO CORRESPONDE À VERSÃO FINAL DA TESE DEFENDIDA PELO ALUNO VITOR PIROVANI PAIXÃO, ORIENTADO PELO PROF. DR. JOSÉ VICENTE HALLAK D'ANGELO.

CAMPINAS
2022

Ficha catalográfica
Universidade Estadual de Campinas
Biblioteca da Área de Engenharia e Arquitetura
Rose Meire da Silva - CRB 8/5974

Paixão, Vitor Pirovani, 1992-
P167s Shift reactor design with integrated heat exchange and waste heat usage / Vitor Pirovani Paixão. – Campinas, SP : [s.n.], 2022.

Orientador: José Vicente Hallak D'Angelo.
Coorientador: Luís Fernando Mercier Franco.
Tese (doutorado) – Universidade Estadual de Campinas, Faculdade de Engenharia Química.

1. Reação de deslocamento gás-água. 2. Reatores químicos. 3. Comportamento de gás real. 4. Ciclo Rankine. I. D'Angelo, José Vicente Hallak, 1967-. II. Franco, Luís Fernando Mercier. III. Universidade Estadual de Campinas. Faculdade de Engenharia Química. IV. Título.

Informações para Biblioteca Digital

Título em outro idioma: Projeto de um reator de deslocamento gás-água com troca térmica integrada e uso de calor residual
Palavras-chave em inglês:
Water-gas shift reaction
Catalytic reactor
Rankine cycle
Área de concentração: Engenharia Química
Titulação: Doutor em Engenharia Química
Banca examinadora:
José Vicente Hallak D'Angelo [Orientador]
Maria Teresa Moreira Rodrigues
Argimiro Resende Secchi
Mauricio Bezerra de Souza Junior
Giselle Patrícia Sancinetti
Data de defesa: 22-08-2022
Programa de Pós-Graduação: Engenharia Química

Identificação e informações acadêmicas do(a) aluno(a)
- ORCID do autor: https://orcid.org/0000-0003-4469-6153
- Currículo Lattes do autor: http://lattes.cnpq.br/7219271922018083

Folha de Aprovação da Defesa de Tese de Doutorado defendida por **VITOR PIROVANI PAIXÃO** e aprovada em 22 de agosto de 2022 pela Comissão Examinadora constituída pelos doutores:

Prof. Dr. José Vicente Hallak D'Angelo
FEQ/UNICAMP

Profa. Dra. Maria Teresa Moreira Rodrigues
FEQ/UNICAMP
(Videoconferência)

Prof. Dr. Argimiro Resende Secchi
COPPE/UFRJ
(Videoconferência)

Prof. Dr. Mauricio Bezerra de Souza Junior
Escola de Química/UFRJ
(Videoconferência)

Profa. Dra. Giselle Patricia Sancinetti
Instituto de Ciência e Tecnologia/UNIFAL
(Videoconferência)

ATA da defesa com as respectivas assinaturas dos membros encontra-se no SIGA/Sistema de Fluxo de Dissertação / Tese e na Secretaria do Programa da Unidade.

To my parents

Acknowledgments

To my parents for the tremendous effort, encouragement, and unconditional support so that I could accomplish my goals.

To my wife Deyse for being supportive and patient.

To professor José Vicente for the guidance, for always being available and for his support with both technical and life aspects, which were crucial during the development of this theses.

To professor Luís Fernando for the valuable discussions and help with technical issues, which allowed me to become a better engineer.

To my colleagues Fernando and Romero for the productive conversations throughout the past years, mostly during the recurrent "pauses for coffee".

To my colleagues from the thermodynamics research group for the constructive advises and comments.

To the Brazilian National Council for Scientific and Technological Development (CNPq) for the financial support under the process number 141396/2018-0 and to the Coordination for the Improvement of Higher Education Personnel (CAPES).

Resumo

Nas últimas décadas tem havido uma crescente preocupação com fontes de energias alternativas. Os ciclos de potência desenvolvidos durante a revolução industrial precisam de fontes de calor a altas temperaturas para alcançar uma eficiência aceitável. Portanto, certa quantidade de calor gerado em plantas químicas e de potência é inapropriada para ser utilizada na geração de eletricidade através de ciclos convencionais. Na indústria química, reações exotérmicas ocorrem com remoção de calor para que alcancem as conversões desejadas. Esse calor é geralmente usado para gerar vapor de baixa pressão que possui baixo valor agregado se não houver sua utilização imediata. Na Parte I deste trabalho é proposto um projeto de um reator catalítico multitubular para a reação de deslocamento gás-água (WGSR). WGSR é uma reação exotérmica conduzida em dois reatores adiabáticos com refrigeração intermediária de modo a atingir a conversão desejada. O objetivo é estudar a viabilidade de substituir tal configuração por um reator com troca térmica integrada. Primeiro, foi feita uma seleção de possíveis catalisadores, sendo escolhido o mais apropriado um baseado em cobre. O reator foi modelado, considerando fenômenos de transporte de movimento, calor e massa. Além disso, o comportamento do gás é descrito pela equação de estado de Peng-Robinson-Stryjek-Vera. Após uma validação contra dados experimentais e industriais, o modelo foi utilizado em um procedimento de otimização para três diferentes casos (OPT1, OPT2 e OPT3). Os resultados mostram que usar tal reator para uma baixa temperatura (430-520 K) não é vantajoso frente à configuração usual, pois requer mais catalisador. No entanto, seu uso tende a ser desejado caso se utilize um catalisador mais ativo ou se conduza uma reação mais exotérmica. Na Parte II o fluido de refrigeração do reator da Parte I foi utilizado como fonte de calor para o ciclo orgânico de Rankine usual (ORC) e recuperativo (RORC). Considerando a temperatura da fonte quente, aspectos ambientais e de segurança, 6 fluidos de uma lista de 78 foram selecionados para as análises. O desempenho de ORC com metanol e etanol foi melhor, enquanto que o desempenho dos outros fluidos se tornou competitivo com a utilização do recuperador (RORC). Na análise econômica, a geração de potência se mostrou fator de extrema importância. Para os casos OPT2 ($\approx$250 kW) e OPT3 ($\approx$850 kW), a receita obtida com a geração de potência não foi suficiente para cobrir as despesas operacionais, resultando em cenários inviáveis. Entretanto, para o caso OPT1 ($\approx$2,5 MW), a viabilidade foi alcançada até mesmo para baixas pressões de operação. O melhor desempenho foi obtido com metanol na pressão de operação mais elevada. Nesse cenário, uma atrativa taxa de retorno interna de 14,5% e um tempo de *pay-back* de 7 anos foram alcançados.

Palavras-chave: Reação de Deslocamento Gás-Água, Reator Catalítico, Comportamento de Gás Real, Ciclo Orgânico de Rankine, Valor Presente Líquido.

Abstract

In the past decades, there has been a growing concern about alternative energy sources. Power cycles developed during the industrial revolution require thermal sources with elevated temperatures to achieve an acceptable efficiency. Therefore, some of the heat generated in chemical and power plants is unsuitable for such cycles. In the chemical industry, several exothermic chemical reactions take place and the heat released by them must be removed to obtain better conversions. This heat is usually used to produce low pressure steam, which has a low capital value if there is no immediate application. In Part I of this work, a design procedure for a multitubular catalytic reactor for the Water-Gas Shift Reaction (WGSR) is proposed. WGSR is an exothermic reaction conducted in two adiabatic reactors with intermediate cooling so that it can achieve the desired conversion. The goal is to study the feasibility of replacing the usual configuration by one reactor with integrated heat exchange. Firstly, a catalyst screening procedure was carried out and the Cu-based catalyst was chosen as the most appropriate one. The reactor was modeled considering mass and heat transport phenomena. In addition, gas behavior was modeled by the Peng-Robinson-Stryjek-Vera equation of state. After proper validation against experimental and industrial data, the model was used in an optimization procedure for 3 different cases (OPT1, OPT2 and OPT3). The optimization results have upmost shown that using the multitubular reactor within the low temperature range of 430 K to 520 K is disadvantageous because of the considerable increase in the catalyst required amount. However, the use of such reactor tends to be desirable if a more active catalyst is used or for a more exothermic reaction. In Part II, a thermoeconomic assessment was carried out. The Part I's reactor cooling fluid was used as heat source for either e regular Organic Rankine Cycle (ORC) or for a recuperative one (RORC). By considering the heat source temperature, environmental and safety aspects, from 78 initial potential working fluids, 6 were selected. After the power cycle simulations, methanol and ethanol had shown the best performance in the ORC configuration, whereas the other fluids performance became competitive only with the addition of a recuperator (RORC). In the economic analysis, net power generation plays a major role. For case OPT2 (≈250 kW net) and OPT3 (≈850 kW net), the power generation revenue was insufficient to cover the operational expenses, yielding unfeasible scenarios. However, for OPT1 (≈2.5 MW net), economic feasibility was achieved even for low operating pressures. Power cycle thermoeconomic performance was the best for methanol as working fluid. In the best scenario, an attractive internal rate of return of 14.5% and a pay-back period of 7 years were achieved.

Keywords: Water-Gas Shift Reaction, Catalytic Reactor, Non-ideal Gas Behavior, Organic Rankine Cycle, Net Present Value.

List of Figures

List of Tables

Acronyms

CEPCI	Chemical Engineering Plant Cost Index
CC	Contingency Costs
EC	Engineering Costs
FT	Fischer-Tropsch
GHSV	Gas Hourly Space Velocity
GWP	Global Warming Potential
HTSR	High Temperature Shift Reactor
ISBL	Inside Battery Limits
LTSR	Low Temperature Shift Reactor
NPV	Net Present Value
OC	Orthogonal Collocation
ODP	Ozone Depletion Potential
ORC	Organic Rankine Cycle
OSBL	Outside Battery Limits
PRSV-EoS	Peng-Robinson-Stryjek-Vera Equation of State
SJP	Shifted Jacobi Polynomial
SLP	Shifted Legendre Polynomial
TCI	Total Capital Investment
TCP	Total Cost of Production
WGSR	Water Gas Shift Reaction

Nomenclature

$\dot{E}x$	Exergy (kW)
$\dot{E}x_{\mathrm{d}}$	Exergy destruction rate (kW)
$\dot{m}$	Mass flow rate (kg·s^{-1})
$\dot{Q}$	Heat rate (kW)
$\dot{W}_{\mathrm{net}}$	Net power (kW)
η_{II}	Second Law efficiency
η_{I}	First Law efficiency
η_{pump}	Pump isentropicw efficiency
η_{turbine}	Turbine isentropic efficiency
ξ	Reduced inverse viscosity (Pa^{-1}·s^{-1})
$\ddot{q}$	Heat flux (kW·m^{-2})
ΔT_{LM}	Logarithmic mean temperature difference (K)
δ	H_2O/CO molar ratio
$\Delta_{\mathrm{r}} h$	Enthalpy of reaction (kJ·mol^{-1})
$\dot{n}$	Molar flow (kmol·s^{-1})
$\dot{V}$	Volumetric flow rate (m^3·s^{-1})
η	Effectiveness factor
γ	Tortuosity
κ	Mass transfer coefficient (m·s^{-1})

λ_{eff}	Effective thermal conductivity of the catalyst particle ($\mathrm{W \cdot m^{-1} \cdot K^{-1}}$)
λ^0	Static contribution to the effective heat conduction coefficient ($\mathrm{W \cdot m^{-1} \cdot K^{-1}}$)
λ_r^D	Dynamic contribution to the radial effective heat conduction coefficient ($\mathrm{W \cdot m^{-1} \cdot K^{-1}}$)
λ_z^D	Dynamic contribution to the axial effective heat conduction coefficient ($\mathrm{W \cdot m^{-1} \cdot K^{-1}}$)
λ_r	Effective radial heat conduction coefficient ($\mathrm{W \cdot m^{-1} \cdot K^{-1}}$)
λ_z	Effective axial heat conduction coefficient ($\mathrm{W \cdot m^{-1} \cdot K^{-1}}$)
$\mathscr{D}$	Effective diffusion inside the catalytic particle ($\mathrm{m^2 \cdot s^{-1}}$)
μ	Viscosity ($\mathrm{Pa \cdot s}$)
ρ	Density ($\mathrm{kg \cdot m^{-3}}$)
$\sum V$	Diffusion volume
τ	Shear stress (kPa)
ε	Bed void fraction
ε_{p}	Catalyst particle void fraction
a_v	Catalyst particle surface area per unit volume ($\mathrm{m^{-1}}$)
A	Heat exchanger area ($\mathrm{m^2}$)
A_{t}	Reactor tube cross sectional area ($\mathrm{m^2}$)
c_p	Specific heat at constant pressure ($\mathrm{kJ \cdot kmol^{-1} \cdot K^{-1}}$)
c_v	Specific heat at constant volume ($\mathrm{kJ \cdot kmol^{-1} \cdot K^{-1}}$)
C	Concentration ($\mathrm{kmol \cdot m^{-3}}$)
C_{BM}	Bare module cost (US$)
C_{BT}	Benefits and training cost (US$)
C_{CW}	Cooling water cost (US$)
C_{L}	Labor cost (US$)
C_{M}	Maintenance cost (US$)

C_p	Purchase cost (US$)
C_R	Real equipment cost (US$)
D_{ji}	Binary diffusion coefficient ($\mathrm{cm^2 \cdot s^{-1}}$)
D_r	Effective radial diffusion coefficient ($\mathrm{m^2 \cdot s^{-1}}$)
D_z	Effective axial diffusion coefficient ($\mathrm{m^2 \cdot s^{-1}}$)
d	Heat exchanger tube diameter (m)
D_K	Knudsen diffusion ($\mathrm{cm^2 \cdot s^{-1}}$)
$D_{\mathrm{m},j}$	Diffusion of the jth component in the fluid mixture ($\mathrm{cm^2 \cdot s^{-1}}$)
d_pore	Pore diameter (cm)
d_p	Catalyst particle diameter (m)
d_t	Reactor tube diameter (m)
E_a	Activation energy ($\mathrm{kJ \cdot kmol^{-1}}$)
e_y	Yearly electricity production (kW·h)
F_p	Pressure correction factor for intrinsic reaction rate (atm)
f	Fouling factor ($\mathrm{W \cdot m^{-2} \cdot K^{-1}}$)
F_P	Correction factor to account for polarity
F_Q	Correction factor to account for quantum effects
g	Gravitational acceleration ($\mathrm{m \cdot s^{-2}}$)
h	Convective heat transfer coefficient ($\mathrm{W \cdot m^{-2} \cdot K^{-1}}$)
h	Specific ethalpy ($\mathrm{kJ \cdot kg^{-1}}$)
h_0	Specific ethalpy at T_0 and P_0 ($\mathrm{kJ \cdot kg^{-1}}$)
J	Molar flux ($\mathrm{kmol \cdot m^{-2} \cdot s^{-1}}$)
k_0	Frequency factor ($\mathrm{kmol \cdot m^{-3}{}_{cat} \cdot h^{-1}}$)
$k_{i,j}$	Binary interaction parameter

K	Equilibrium constant
k	Rate constant (kmol·m$^{-3}_{\text{cat}}$ ·h^{-1})
k_{w}	Tube wall thermal conductivity (W·m^{-1}·K^{-1})
L	Heat exchanger tube length (m)
L_{t}	Reactor tube length (m)
M	Molar mass (kg·kmol^{-1})
N_t	Total number of tubes
Nu	Nusselt number
Pr	Prandtl number
P	Pressure (bar)
P_0	Environment pressure (bar)
P_{c}	Critical pressure (bar)
P_{r}	Reduced pressure
Re	Reynolds number
R	Reactor tube radius (m)
r	Real reaction rate (kmol·m^{-3}·s^{-1})
R_{g}	Ideal gas constant
r_{int}	Intrinsic reaction rate (kmol·m$^{-3}_{\text{cat}}$·h^{-1})
Sc	Schmidt number
Sh	Sherwood number
S	Entropy (kJ·K^{-1})
s	Specific etropy (kJ·kg^{-1}·K^{-1})
s_0	Specific etropy at T_0 and P_0 (kJ·kg^{-1}·K^{-1})
T	Temperature (K)

t	Time (s)
T_0	Environment temperature (K)
T_{cf}	Temperature of the reactor cooling fluid (K)
T_{c}	Critical temperature (K)
T_{r}	Reduced temperature
U	Overall heat transfer coefficient ($\mathrm{W \cdot m^{-2} \cdot K^{-1}}$)
v	Velocity ($\mathrm{m \cdot s^{-1}}$)
y	Molar fraction

Table of Contents

Chapter 1

Introduction

The application of solid catalysts for reaction conversion enhancement in the beginning of the last century has boosted the chemical industry production capacity. The reactors capacities have also greatly increased ever since. For example, in the 1950's, an ammonia converter had a capacity of 50,000 tons/year. Nowadays, this reactor capacity has increased to approx. 1,500,000 tons/year. The improvement in the production capacity is due to the development of new catalysts, use of new material of construction, improvement of auxiliary equipment and the development of accurate reactor models for better designing (Froment et al., 2011).

The Water Gas Shift Reaction (WGSR) is a catalytic enhanced reaction, which plays a vital role in the synthesis gas (syngas) purification. This reaction was first reported by Felice Fontana more than two centuries ago. It has gained importance in the chemical industry mainly after the development of the Haber-Bosch process for ammonia production. In this process, the WGSR is used to reduce the syngas CO content to tolerated levels - this compound is a poison to the ammonia reactor catalyst. The WGSR is of significant importance for other processes such as the methanol synthesis, the Fischer-Tropsch (FT) synthesis, in hydrocracking of petroleum fractions, and, more recently, for syngas final purification for fuel cell applications (Smirniotis and Reddy, 2015).

The WGSR is usually conducted in two adiabatic reactors (Smirniotis and Reddy, 2015). Since the reaction is exothermic, intermediate cooling between the reactors is required in order to increase the final conversion. An alternative to the usual configuration is to perform the WGSR in one single reactor. This can be accomplished in a shift reactor with integrated heat exchange. Since the WGSR is exothermic, the heat released must be transferred to a cooling media to assure a reduced fluid temperature increase inside the reactor. A report of the European Commission pointed out this reactor as one of the equipment that could improve the performance of chemical plants by saving energy and reducing plant startup time

(IPPC, 2007).

To better understand the reactor performance, simulations can be very helpful. Reactor modeling is a useful tool, which can drastically reduce the number of experimental tests to predict the reactor behavior by simply performing simulations. Different studies about reactor performance are available in the literature. Some of them are based on thermodynamic equilibrium, e.g., Gibbs energy minimization, which are unable to predict in detail the fluid behavior inside the reactor. Others are phenomenological models, which are able to describe in detail the fluid behavior but are considerably more complex to be solved. Regarding the WGSR reactor, the studies available in the literature consider ideal gas behavior which is acceptable for syngas purification in fuel cells but might lead to prediction errors in industrial plants where the operating pressure is considerably above atmospheric. In addition, none of them consider the possibility of heat exchange with a cooling fluid to keep the reactor temperature inside an optimal range.

The heat released by the WGSR is normally used to produce low pressure steam, which might be of low economic value for the plant due to its limited application. The low pressure steam along with flaring gas, cooling air, etc., are carriers of what is called "waste heat". This is because of its low temperature (approx. 250 °C), the heat that they carry cannot be converted into useful forms of energy by conventional power plants. In addition, since they are wasted at a temperature considerably above the ambient, they generate the so-called "thermal pollution".

Since the beginning of the industrial revolution, thermodynamic cycles have been studied and different configurations are proposed in literature. The most common cycle used in the industry to transform heat into power is the Rankine cycle, also known as the Clausius-Rankine cycle (Çengel and Boles, 2007). The Rankine cycle has been used for more than one century but recently, in the last three decades at least, a concern about thermal pollution and better usage of thermal resources for efficiency improvement and, consequently, cost reduction has become more evident. The necessity of using other energy sources, e.g., solar and geothermal, to produce power is growing. However, to use such resources, different working fluids, better efficiencies, higher flexibility, adaptability and different configurations of the power cycles are required.

Since the 70's, scientists have been developing alternative power cycles to use heat sources with lower temperatures than that required by the conventional Rankine cycle. These alternative cycles are able to operate at temperatures as low as 100 °C, which make them feasible to be applied in solar and geothermal power plants and to be used to recover the heat wasted by the chemical industry. In this work the WGSR is under consideration, but any other exothermic reaction, e.g., the hydrodealkylation of toluene and the ammonia synthesis, can benefit from the concept of "waste heat into power", provided that there is no other use for the low-grade heat inside the plant.

1.1 Thesis Arrangement

This work is divided into three parts. Part I and Part II have their own independent objective and structure consisting of literature and theory review, methodology, results and discussion, and conclusion. In Part III, a closure is provided with the overall conclusion and suggestions for future work.

In Part I, the possibility of replacing the original WRGS adiabatic catalytic reactors configuration by one single multitubular catalytic reactor with integrated heat exchange is evaluated. To perform the evaluation a literature review about the WGSR kinetics is carried out so that the most appropriated catalyst for the temperature range under consideration can be chosen. With the WGSR kinetics, a 2D pseudo-homogeneous reactor model is built and validated against literature-available experimental and industrial data. The optimum reactor size and catalyst mass for three different operational scenarios are found using the validated model in an optimization procedure which aims at minimizing both operational and capital expenditures. Finally, with the optimization results a comparison between the proposed and the actual reactor arrangement is accomplished .

In Part II, the cooling fluid of each reactor from Part I is used as heat source for two different Organic Rankine Cycle (ORC) arrangements. The goal is to evaluated the economic feasibility of using such heat source to generate electricity. Due to the wide range of working fluids available, a preliminary screening based on environmental and safety aspects is carried out. Afterwards, a model based on the First and Second Law of Thermodynamics is built for the two ORCs arrangements under consideration. The fluids with the best thermodynamic performance are selected for a final economic assessment based on the power cycle's Net Present Value (NPV). To estimate the power cycle's capital cost with an acceptable accuracy, all heat exchangers are designed considering literature-available correlation for overall heat transfer coefficient calculation.

Part I

The Reactor

Chapter 2

Main Objective

Evaluate the possibility of replacing the original Water-Gas Shift Reaction (WGSR) adiabatic catalytic reactors with intermediate cooling by one multitubular catalytic reactor with integrated heat exchange.

2.1 Specific Objectives

- Define an operational temperature range and select an appropriate catalyst;
- Develop a mathematical model able to predict the actual reaction rate, taking into account mass and heat transfer resistances between bulk fluid and catalyst surface, diffusion resistance inside the catalyst particle and non-ideal gas behavior;
- Develop, simulate, validate, and optimize a phenomenological model able to predict the reactor outlet composition, catalyst mass, and heat exchange area for a specified capacity;
- Compare the optimized multitubular reactor performance with the usual High Temperature Shift Reactor (HTSR) - Low Temperature Shift Reactor (LTSR) configuration.

Chapter 3

Literature Review and Fundamentals

3.1 Water Gas Shift Reaction (WGSR)

The WGSR is an exothermic, equilibrium controlled, and catalytic enhanced reaction (Eq. 3.1.1). It is vastly used in the chemical industry to either remove CO simultaneously increasing the H_2 content in the synthesis gas or to regulate the H_2/CO ratio (Smirniotis and Reddy, 2015).

$$H_2O + CO \rightleftharpoons CO_2 + H_2 \qquad \Delta_\mathrm{r} h_{(\mathrm{at\ 298\,K\ and\ 1\,bar})} = -41.1\ \mathrm{kJ{\cdot}mol^{-1}} \tag{3.1.1}$$

When the reaction was first applied in industrial scale, it was conducted in a single fixed-bed catalytic reactor packed with a Fe-based catalyst at temperatures between 450 °C and 600 °C. This single bed reactor was able to reduce the CO content in the syngas to 10%. To further reduce the CO content, a second reactor was placed after the first reactor. This new reactor operated with the same catalyst but at a temperature range of 320 °C - 360 °C, thus, intermediate cooling was necessary. With this modification, the CO content could be decreased to up to 3%. The reactor which operates with the Fe-based catalyst is known as the High Temperature Shift Reactor (HTSR). From the thermodynamic point of view, it would be preferable to operate the reactors at approx. 200 °C since the reaction is exothermic and equilibrium controlled. However, the Fe-based catalyst is insufficiently active at this temperature (Bartholomew and Farrauto, 2006; Smirniotis and Reddy, 2015).

After the development of a Cu-based catalyst, which is active between 150 °C and 250 °C, the Fe-based catalyst in the second reactor was replaced. With this replacement, concentrations of CO below 0.3% can be achieved. The reactor, which operates with the Cu-based catalyst, is known as Low Temperature Shift Reactor (LTSR), and operates usually at 200 °C. In fact, it could be operated at a lower temperature since the WGSR is exothermic.

However, the usual operating pressure of these reactors is about 30 bar and, at this pressure, water condensation could occur at temperatures below 200°C which would damage the catalyst. Moreover, the temperature reduction also decreases the reaction rate, increasing catalyst mass and, consequently, the reactor size and its cost (Bartholomew and Farrauto, 2006; Smirniotis and Reddy, 2015).

According to the Le Châtelier principle, the WGSR equilibrium conversion remains unaffected by the pressure. The high operating pressure might be a consequence of the operating pressure of equipment upstream. For example, in ammonia plants the syngas is generated by the steam reforming of natural gas, which occurs at pressures usually above 30 bar (Bartholomew and Farrauto, 2006; Eggeman, 2010). Since the HTSR and LTSR are placed downstream the reformer, their operating pressure are consequently high. For other processes such as biomass gasification in which gasifiers might operate at atmospheric pressure, the shift reactors could be operated at a lower pressure. Another reason for high operating pressure in the shift reactors is that the catalytic activity decreases when the operating pressure decreases (Rase and Holmes, 1977). However, there might be an economic trade-off between operating pressure (power consumption) and required catalyst amount (reactor size).

3.2 Equilibrium Constant

The WGSR is an equilibrium-limited reaction. The equilibrium constant (K) of any reaction can be defined as a function of the absolute temperature (T) as represented in Eq. 3.2.1 (Smith et al., 2007).

$$\frac{\mathrm{d}\,(\ln K)}{\mathrm{d}T} = \frac{\Delta_{\mathrm{r}} h}{R_{\mathrm{g}}\,T^2} \tag{3.2.1}$$

where $\Delta_{\mathrm{r}} h$ (kJ·mol^{-1}) is the standard enthalpy of reaction, which may also be defined as a function of T (K)(Eq. 3.2.2) (Appl, 1999), and R_{g} is the ideal gas constant.

$$\Delta_{\mathrm{r}} h = -47.617 \times 10^{3} + 1.302 \times 10^{-2} T - 0.126 \times 10^{-5} T^2 + 0.791 \times 10^{3} T^{-1} \tag{3.2.2}$$

Different equation forms to determine the WGSR heat of reaction can be found in the literature, where K is represented only as function of T. Smirniotis and Reddy (2015) presents the empirically derived Moe's equation (Moe, 1962), where K is an exponential function of T (Eq. 3.2.3). Appl (1999) and Souza (2013) also presents K as an exponential function of

T in Eq. 3.2.4 and 3.2.5 , respectively. However their expressions are more complex.

$$K = \exp\left(\frac{4{,}577.8}{T} - 4.33\right) \tag{3.2.3}$$

$$\begin{aligned}\ln\left(\frac{1}{K}\right) &= 13.148 - \frac{5{,}693.5}{T} - 1.077\,\ln T \\ &\quad - 5.44\times10^{-4}T - 1.125\times10^{-7}T^2 + \frac{49{,}170}{T^2}\end{aligned} \tag{3.2.4}$$

$$K = \exp\left(\frac{5{,}872.461}{T} + 1.86\ln(T) - 2.69\times10^{-4}T - \frac{58{,}200}{T^2} - 18.014\right) \tag{3.2.5}$$

To increase the CO conversion in adiabatic shift reactors, the inlet gas is usually diluted into H_2O so that the equilibrium can be shifted towards the H_2 formation (Eq. 3.1.1). In Fig. 3.1, the CO conversion at equilibrium is shown as a function of T and H_2O/CO molar ratio (Smirniotis and Reddy, 2015).

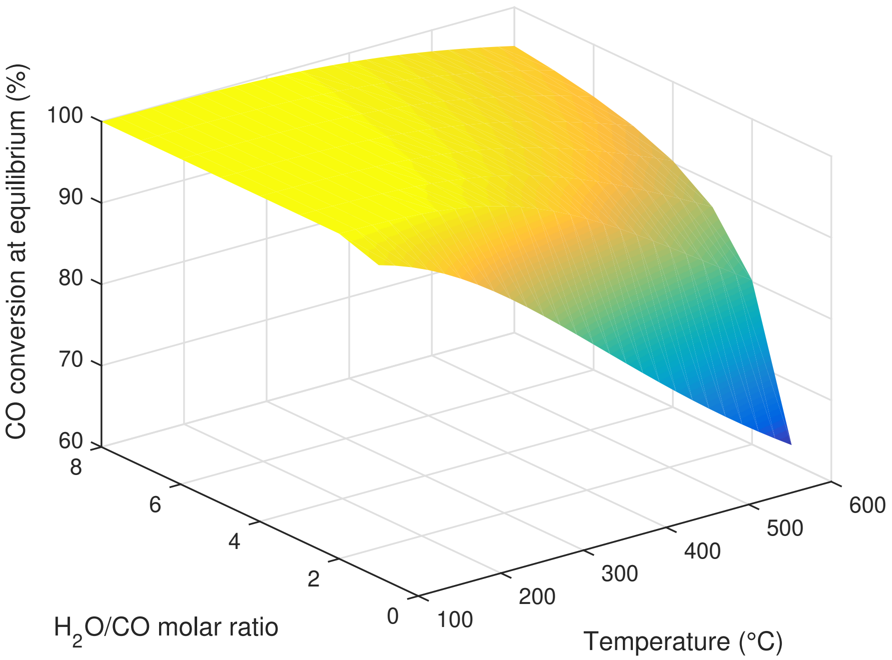

Figure 3.1: CO conversion (%) at equilibrium as a function of T for various H_2O/CO molar ratios (Adapted from Smirniotis and Reddy (2015)).

Obviously, increasing the H_2O/CO molar ratio, higher CO conversions can be obtained at lower temperatures. However, when the H_2O/CO molar ratio increases, the costs to generate the required H_2O vapor and the reactor size also increase. Therefore, the best H_2O/CO can only be obtained after optimization of the design and cost equations (Rase and Holmes, 1977).

3.3 Catalysts and Reaction Rate

To design catalytic reactors it is necessary to know the reaction rate over the selected catalyst. Throughout the last decades several authors have proposed different reaction rates based on different catalysts. Although the composition of these catalysts varies according to the manufacture, most of them are either Fe- or Cu-based. In addition, recently noble metals such as Pt, Ru and Au have raised the interest of scientists due to their higher activity (Smith et al., 2010).

The Fe-based catalyst is used in the HTSR and its main constituents are Fe (80%-90%) and Cr_2O_3 (8%-10%). In this catalyst, Cr_2O_3 acts as stabilizer avoiding thermal sintering. It can operate under industrial condition from 2 to 5 years, and it is resistant to sulfur poisoning (Smirniotis and Reddy, 2015).

The Cu-based catalyst is used for lower temperature applications due to its higher activity. This catalyst is very sensitive to sulfur and do not tolerate concentrations higher than 1 ppm. In the usual HTSR-LTSR configuration, the HTSR serves as a guard bed absorbing sulfur. If only Cu-based catalysts are used to enhance the WGSR, a guard bed, usually containing ZnO, must be placed upstream to avoid sulfur poisoning (Smirniotis and Reddy, 2015; Smith et al., 2010). This catalyst can also be damaged by other halogen compounds and unsaturated hydrocarbons but, with proper gas cleaning, it can be used from 2 to 6 years before replacement (Rase, 1990; Rase and Holmes, 1977).

An alternative to sulfur poisoning is the use of Co-Mo catalysts. These catalysts are able to operate in a lower temperature range than the usual Fe-based catalyst (523 K - 623 K) (250 °C - 350 °C). In addition, the requested H_2O/CO ratio is lower than that required by the Fe-based catalyst. The Co-Mo catalyst is not only tolerant to sulfur compounds but also presents its more active form in the presence of sulfur. In fact, for an acceptable performance, the feed gas must contain at least 0.3% of sulfur. The disadvantages of these catalysts are that the reactor needs to be operated at a lower space velocity and 20% more catalyst is required to achieve a similar performance when compared to the Fe-based catalyst (Smirniotis and Reddy, 2015).

Smith et al. (2010) and Saeidi et al. (2017) have carried out a comprehensive literature review about the intrinsic reaction rate (r_{int}) models reported in the literature for several WGSR catalysts. Although a vast variety of them are proposed, most are based either on the

Langmuir-Hinshelwood model (Eq. 3.3.1) or on the power law model (Eq. 3.3.2) (Smith et al., 2010). In Langmuir-Hinshelwood model, it is considered that the reactants are adsorbed on similar active sites of the catalyst where the products are formed and later desorbed (Mendes et al., 2010). Furthermore, some authors might use the components' partial pressure instead of the concentration to report their data.

$$r_{\text{int}} = \frac{kK_{\text{CO}}K_{\text{H}_2\text{O}}\left([\text{CO}]\,[\text{H}_2\text{O}] - \frac{[\text{CO}_2][\text{H}_2]}{K}\right)}{\left(1 + K_{\text{CO}}\,[\text{CO}] + K_{\text{H}_2\text{O}}\,[\text{H}_2\text{O}] + K_{\text{CO}_2}\,[\text{CO}_2] + K_{\text{H}_2}\,[\text{H}_2]\right)^2} \tag{3.3.1}$$

$$r_{\text{int}} = kP^{l}_{\text{CO}}P^{m}_{\text{H}_2\text{O}}P^{n}_{\text{CO}_2}P^{o}_{\text{H}_2}\left(1 - \frac{P_{\text{CO}_2}P_{\text{H}_2}}{KP_{\text{CO}}P_{\text{H}_2\text{O}}}\right) \tag{3.3.2}$$

where l, m, n and o are exponential factors, k is the rate constant, which is determined by the Arrhenius's equation (Eq. 3.3.3) and K_i, P_i and K are the adsorption equilibrium constant and the partial pressure of the i component and the equilibrium constant, respectively.

$$k = k_0 \exp\left(\frac{-E_{\text{a}}}{R_{\text{g}}T}\right) \tag{3.3.3}$$

where k_0 is the frequency factor and E_{a} is the activation energy.

Keiski et al. (1992) studied the kinetics of the WGSR over a Fe-based catalyst in a temperature range of 575 K - 657 K. The authors estimated the parameters of Eq. 3.3.2 using experimental data obtained for a wide range of H_2O/CO ratios (2.7 - 12). After the fitting procedure, the authors concluded that the parameter o in Eq. 3.3.2 could assume a positive or a negative value depending on the used set of experiments. Therefore, due to this ambiguous result, it was removed from the final model, i. e., $i = 0$. Despite the removal of o, Eq. 3.3.2 could represent the experimental data very well. The final value of the parameters l, m and n obtained were 0.74, 0.47 and -0.18 , respectively. E_{a}/R and k_0 were equal to 9,598 $\text{kJ}\cdot\text{mol}^{-1}$ and 2.623×10^6 $((\text{dm}^3)^{l+m+n}\cdot\text{mol}^{1\text{-}l\text{-}m\text{-}n}\cdot\text{kg}^{-1}\cdot\text{s}^{-1})$.

Amadeo and Laborde (1995) carried out an experimental study to determine the reaction rate of the WGSR over a Cu-based catalyst for low temperature applications (453 K - 503 K). The authors have proposed 5 different models to represent r_{int}. Two of them represent the redox mechanism and the other three are Langmuir-Hinshelwood-type models. The best experimental data fitting was found for one of the Langmuir-Hinshelwood-type model (Eq. 3.3.4). The authors have also formulated a 1D[1] plug-flow model so that the accuracy of Eq. 3.3.4 could be tested against industrial data. Since the experiments used to estimate the parameters present in Eq. 3.3.4 were carried out at atmospheric pressure, they used a

---

[1] Only the axial coordinate is considered

correlation reported by Rase and Holmes (1977) to account for operation at higher pressures for the Cu-based catalyst (Eq. 3.3.5). In addition, Eq. 3.3.5 also takes into account diffusional effects in the catalyst (Smith et al., 2010).

$$r_{\text{int}} = \frac{0.92 \exp\left(\frac{-454.3}{T}\right) P_{CO} P_{H_2O} \left(1 - \frac{P_{CO_2} P_{H_2}}{K P_{CO} P_{H_2O}}\right)}{\left(1 + K_{CO} P_{CO} + K_{H_2O} P_{H_2O} + K_{CO_2} P_{CO_2} + K_{H_2} P_{H_2}\right)^2} \tag{3.3.4}$$

where $K_{CO} = 2.2 \exp\left(\frac{101.5}{T}\right)$, $K_{H_2O} = 0.4 \exp\left(\frac{158.3}{T}\right)$, $K_{CO_2} = 0.0047 \exp\left(\frac{2737.9}{T}\right)$, $K_{H_2} = 0.05 \exp\left(\frac{1596.1}{T}\right)$, r_{int} is given in mol·g^{-1}$_{\text{cat}}$·min^{-1}, T is in K and P_i is in Pa.

$$\begin{aligned} \psi &= 0.86 + 0.14P && \text{for } P \leq 24.8 \text{ atm} \\ \psi &= 4.33 && \text{for } P > 24.8 \text{ atm} \end{aligned} \tag{3.3.5}$$

The factor (ψ) must multiply r_{int} so that the aforementioned effects can be taken into account. Amadeo and Laborde (1995) also compared the prediction capability of the reaction rate given by Moe (1962) (Eq. 3.3.6) with the industrial data of an adiabatic LTSR. Although the results of the model proposed by them were in good agreement with the industrial data, the results predicted by their model with Moe's reaction rate was slightly better. This might be the reason of why Moe's equation were the most popular equation used for reactor designing despite its empirical nature (Amadeo and Laborde, 1995). In Eq. 3.3.6, T is in K, P_i is in atm and r_{int} is given in mol·g^{-1}$_{\text{cat}}$·min^{-1}.

$$r_{\text{int}} = 1.85 \times 10^{-5} \exp\left(12.88 - \frac{1855.5}{T}\right) P_{CO} P_{H_2O} \left(1 - \frac{P_{CO_2} P_{H_2}}{K P_{CO} P_{H_2O}}\right) \tag{3.3.6}$$

Choi and Stenger (2003) conducted experiments over a commercial CuO/ZnO/Al_2O_3 catalyst to determine the kinetics of the WGSR in the temperature range of 120 °C - 250 °C. For the temperature range studied, the equilibrium conversion is difficult to be achieved, i.e., the reaction is kinetically limited. However, for the highest temperature, i.e., 250 °C, a CO conversions near to 100% can be obtained operating the reactor with a H_2O/CO molar ratio higher than 2. The authors fitted their experimental data on 5 different kinetic models, and concluded that all five models represent the kinetics of the WGSR with accuracy and can be used to either simulate or design the reactor despite the slightly better fitting achieved for the model represented by Eq. 3.3.1. In addition, the authors also showed that with the increase of the Gas Hourly Space Velocity (GHSV), the CO conversion decreases.

Indeed the GHSV plays a important role in the CO conversion. Pasel et al. (2005) showed by means of experimental results that the higher the GHSV, the lower the CO final conversion for both isothermal and adiabatic operation. The effect of the GHSV on the CO final conversion has also been reported by Chen et al. (2008). In their study, it was observed (by means of computer simulations of a 2-D[1] model) that higher CO conversions were obtained near the reactor wall when compared to the reactor center. The explanation, according to the authors, was that the flow velocity decreases from the reactor center towards its wall which, in turn, increase the residence time of the reagents improving the CO conversion.

Ding and Chan (2008) determined the parameters of Eq. 3.3.1 for a Pt-based catalyst operating between 500 °C - 700 °C. The comparison between the values predicted by Eq. 3.3.1 and obtained in the experiments were in excellent agreement. The maximum deviation obtained was of 0.56% and 0.47% for the H_2 and the CO molar fractions, respectively. For the Pt-based catalyst the authors also reported the influence of the GHSV on the CO conversion. However, according to the authors, the temperature effect is greater.

Chen et al. (2008) proposed a new kinetic model combining Moe's reaction rate (Eq. 3.3.6) with an polynomial function to account for H_2O/CO molar ratio variation. The constants were estimated using experimental data for both commercial high and low temperature catalysts. After the data fitting procedure, both Eq. 3.3.7 (high temperature catalyst (300 °C - 500 °C)) and Eq. 3.3.8 (low temperature catalyst (200 °C - 400 °C)) showed good agreement with the experimental data.

$$r_{\text{int}} = 1.78 \times 10^{22} \left(1 + 0.0097\delta - 1.1364\delta^2\right) T^{-8} e^{\left(\frac{-70}{R_g T}\right)} P_{\text{CO}} P_{\text{H}_2\text{O}} \left(1 - \frac{P_{\text{CO}_2} P_{\text{H}_2}}{K P_{\text{CO}} P_{\text{H}_2\text{O}}}\right) \tag{3.3.7}$$

$$r_{\text{int}} = 1.74 \times 10^{17} \left(1 - 0.154\delta + 0.008\delta^2\right) T^{-8.5} e^{\left(\frac{-35}{R_g T}\right)} P_{\text{CO}} P_{\text{H}_2\text{O}} \left(1 - \frac{P_{\text{CO}_2} P_{\text{H}_2}}{K P_{\text{CO}} P_{\text{H}_2\text{O}}}\right) \tag{3.3.8}$$

where δ is the H_2O/CO molar ratio.

Mendes et al. (2010) studied the kinetics of the WGSR in the temperature range of 180°C - 300 °C over a commercial Cu-based catalyst ($CuO/ZnO/Al_2O_3$). The experiments were conducted under isothermal condition (a negligible temperature gradient of ±1°C between inlet and outlet was observed). They tried to fit the experimental data on 5 different models - 2 Langmuir-Hinshelwood type, 1 oxidation-reduction type, and 2 empirical (Eqs. 3.3.2 and 3.3.6). Over the entire temperature range, one of the Langmuir-Hinshelwood type model (Eq. 3.3.1) showed the best fitting. However, the authors also considered the possibility of changing the mechanism controlling the reaction rate over the temperature range. After

---

[1] Both axial and radial coordinates are considered

tests, this was confirmed. In the temperature range of 180 °C - 200 °C, Eq. 3.3.1 still provided the best fitting for the experimental data. Nevertheless, from 230 °C to 300 °C the oxidation-reduction type model provided the best fitting.

As mentioned before, for a syngas with high content of sulfur compounds the use of a Co-Mo-based catalyst might be an alternative. Hla et al. (2011) carried out an experimental study to compare the performance of a commercial Co-Mo-based catalyst with an usual Fe-based catalyst at 450 °C in the presence of H_2S. Although the Fe-based catalyst activity decreases in the presence of H_2S, it was still superior than the Co-Mo-based catalyst activity when the H_2S composition was lower than 1%. Therefore, the usage of the tested catalyst is only advisable when the syngas possesses high concentration of H_2S. In addition, it might be preferable to reduce the H_2S content in the syngas prior the reactor in oder to minimize corrosion. In this case, the Fe-based catalyst is still the best option for high temperature operation. Apart from the comparison between catalysts, the authors fitted the experimental data for the Co-Mo-based catalyst on Eq. 3.3.2. The model obtained was considered good. Similar results were also obtained by Plaza et al. (2016) for different operation conditions. However, they were not able to determine the minimum amount of H_2S required for superior performance of the Co-Mo-based catalyst.

The catalysts composition changes according to the manufacture and, consequently, its performance also changes. In addition, there is no consensus on which reaction rate model is the most appropriate for predicting the CO conversion. As could be seen in this section, different models have been proposed throughout the decades and each of them represents the reaction kinetics over a specific catalyst and operating condition.

3.4 Alternative Reactors for WGSR Application

Other catalytic reactor types have been investigated to replace the usual adiabatic HTSR-LTSR configuration mentioned in Section 3.2. The first alternative is to carry out the reaction in a membrane reactor. This reactor still has a bed packed with catalyst but its wall is involved by a membrane which selectively separates the chosen component, e.g., the hydrogen being formed. Since the WGSR is equilibrium limited, the H_2 removal would shift the equilibrium towards the product formation. Therefore, high CO conversion can be achieved with this type of reactor. However, its capital cost might limit its application (Adams II and Barton, 2009; Smirniotis and Reddy, 2015).

The second alternative is to conduct the WGSR in a multitubular packed bed reactor with integrated heat exchange. In this configuration, the heat released by the WGSR is removed by a cooling fluid, keeping the temperature inside reactor almost constant. This reactor is know as isothermal packed-bed reactor and it is used not only for the WGSR but also for any other heat intensive reaction such as the methanol synthesis (Smirniotis and Reddy, 2015). For WGSR application, the copper-based catalyst can be used, allowing the reaction to take place at a low temperature (Appl, 1999). In the most common arrangement, the catalyst is packed inside the tubes and the cooling media flows in the shell-side although other configurations are possible. Typical multitubular reactors are up to 15 m high, 8 m wide and there are thousands tubes inside with inner diameter ranging from 15 mm to 50 mm (Eigenberger and Ruppel, 2012).

Pasel et al. (2005) has carried out a laboratory experiment comparing the performance of a catalyst (unfortunately the composition was not mentioned by the authors) operating in a reactor either isothermally or adiabatically. The isothermal operation mode showed clear advantage over the adiabatic one. Operating at almost identical Gas Hourly Space Velocity (GHSV) the conversion achieved during isothermal operation was always superior than that achieved during adiabatic operation at the same outlet temperature.

3.5 Catalytic Fixed-Bed Reactors Models

Modeling of chemical reactors is a result of the necessity of better understanding the equipment for improvements in design, scale-up, start-up, controlling, optimization and comprehension of the effect of some variables on the equipment's behavior. To develop a model, a sequence of steps might be followed. The simplest model should firstly be considered since it might be easily solved, reducing computational time. Some background knowledge is helpful in this stage. After setting up the model, the parameters involved should be estimated with accuracy. The development of a model is as important as the correct prediction of the parameters in the model. At last, the model must be validated against experimental results. In case of great divergence between the predicted values and the experimental ones, the modeling procedure must begin again, but considering other effects that were neglected in the previous model. This certainly increases the model's complexity (Martinez et al., 1985).

Although models based on thermodynamic equilibrium are found in literature to describe the conversion of a specific reaction, models based on transport phenomena are used to describe the reaction throughout the reactor in detail. Models based on transport phenomena are composed by the continuity equation for global (Eq. 3.5.1) and component (Eq. 3.5.2) mass balance, the energy balance (Eq. 3.5.3) (for only one reaction tanking place) and the momentum balance (Eq. 3.5.4) (Bird et al., 2002; Froment et al., 2011).

$$\frac{\partial \rho}{\partial t} + \left(\nabla \cdot \rho \vec{v}\right) = 0 \tag{3.5.1}$$

$$\frac{\partial C_i}{\partial t} = -\left(\nabla \cdot C_i \vec{v}\right) - \left(\nabla \cdot \vec{J_i}\right) + \nu_i r \tag{3.5.2}$$

$$\rho c_p \frac{DT}{Dt} = -\left(\nabla \cdot \vec{q}\right) - \left(\frac{\partial \ln\rho}{\partial \ln T}\right)_P \frac{DP}{Dt} - \left(\vec{\vec{\tau}} : \nabla \vec{v}\right) + \left(-\mathit{\Delta}_{\mathrm{r}h}\right) r \tag{3.5.3}$$

$$\rho \frac{D\vec{v}}{Dt} = -\nabla P - \left(\nabla \cdot \vec{\vec{\tau}}\right) + \rho \vec{g} \tag{3.5.4}$$

where $\vec{v}$ is the velocity vector, ρ is the density, t is time, C_i is the concentration of the ith component, $\vec{J_i}$ is the molar flux vector of the ith component, c_p is the specific heat at constant pressure, $\vec{q}$ is the heat flux vector, $\vec{\vec{\tau}}$ is the viscous stress tensor, and $\vec{g}$ is the gravitational acceleration vector. ∇ is the differential operator and $\frac{D}{Dt}$ is the substantial derivative operator.

The general momentum balance shown in Eq. 3.5.4 is valid for all kind of fluids since no simplification was made during its development. However, simplifications are acceptable under certain circumstances. For example, Francesconi et al. (2007) established for their reactor design problem that plug flow wa valid if the ratio between the reactor tube length and the catalyst particle diameter ($L_{\mathrm{t}}/d_{\mathrm{p}}$) was higher than 30 and the ratio between the reactor tube diameter and the catalyst particle diameter ($d_{\mathrm{t}}/d_{\mathrm{p}}$) was higher than 10. These restrictions are easily attained in adiabatic packed beds, but are unrealistic for most multitubular packed beds with heat exchange due to $d_{\mathrm{t}}/d_{\mathrm{p}} < 10$ and to the bed void fraction (ε) dependence on the radial position (Hunt and Tien, 1988; Papageorgiou and Froment, 1995; Tsotsas, 2010; Vortmeyer et al., 1992).

In the next paragraphs, the results found by other authors using models derived from Eq. 3.5.1 - 3.5.4 are reviewed. For all of them good agreement with experimental data was obtained. In addition, two different approaches are found in literature for representing fixed-bed catalytic reactors: the heterogeneous model in which the solid phase (catalyst) and the fluid phase are considered separately, and the pseudo-homogeneous model, in which the solid phase is not explicitly considered.

Giunta et al. (2006) developed a 1D heterogeneous model to study the WGSR at low temperatures. After the model validation, it was shown that the catalyst pellets can be considered isothermal. In addition, the increase in the desired CO final conversion increases the required catalyst mass and the reactor volume. A comparison between the isothermal and adiabatic operations modes was also made. Despite the advantage of the isothermal operation mode, the authors advise the use of an adiabatic reactor due to its simplicity. Also, for pellets diameters larger than 5 cm the pressure drop was equal to approx. 0.2 atm and, for pellets lager than 7.5 cm, the reactor can be considered isobaric.

Francesconi et al. (2007), by means of a 1D heterogeneous model, developed a methodology from which it is possible to minimize the LTSR volume. Three different scenarios were analyzed: one single adiabatic reactor, two adiabatic reactors with intermediate cooling and one single reactor considering heat loss to the environment. The optimization methodology used for sizing the reactors was also able to find the most appropriate catalyst particle size considering a trade-off between pressure drop and intraparticle diffusion limitation. For the base capacity selected, the optimum particle diameter was found at the lower bound, i.e., the smallest diameter possible. Since the reactor was small (volume $<$1,500 cm^3), the pressure drop was insignificant and, to minimize intraparticle diffusion limitation, the catalyst particle diameter was reduced to its lower bound. However, increasing the capacity, the reactor size also increases. This cause the particle diameter to increase so that the pressure drop constraint could be respected. From the three studied cases, non-adiabatic operation (heat loss to the environment) was the best option. The authors also compared their model performance with a 2D pseudo-homogeneous model at the same conditions. The results showed a negligible temperature difference between the models' predictions capabilities along the axial coordinate.

Ding and Chan (2008), using a 2D heterogeneous model, performed several simulations varying the temperature (500°C-700°C), the H_2O/CO ratio (1-8) and the GHSV (100 h^{-1} - 1,700 h^{-1}) for an adiabatic reactor containing a Pt-based catalyst. The authors concluded that a higher temperatures combined with a high H_2O/CO ratio (to shift the equilibrium) favor the reaction and the optimum is between 600°C and 700°C for the catalyst used. The best GHSV is between 106.09 h^{-1} and 212.18 h^{-1}.

Chen et al. (2008) studied the behavior of the CO conversion inside the HTSR and the LTSR using a 2D heterogeneous model. From the model simulation results, the flow velocity greatly affects the reaction conversion throughout the catalytic bed. By integrating the HTSR with the LTSR, the system becomes more robust, suffering minor changes in the final CO conversion, even for great temperature variations in the HTSR inlet temperature. For the LTSR, the best inlet temperature found was 200°C.

Adams II and Barton (2009) developed a dynamic 2D heterogeneous model for both the LTSR and the HTSR. After validation against experimental results, the model was used to predict the dynamic behavior of the independent variables, e.g, temperature and molar fraction, in the reactors during startup and changes in the inlet conditions. It was found that temperature picks might occur during startup, which might cause damage to the catalyst. In addition, the authors tested the effect of some parameters on the model prediction capability by means of a sensitivity analysis. The activation energy was found to affect the model's result the most while the catalyst heat capacity and the diffusivity parameter for CO have minor impact during dynamic operation and their effect tend to zero in steady-state operation.

Marín et al. (2012) compared the performance of a HTSR with a membrane reactor (MR) by means of a 2D heterogeneous model. Firstly, the authors studied the possibility of replacing the solid phase model by simpler alternatives in order to ease the reactor's model resolution. For this part, just the HTSR was considered, i.e., there was no membrane. The most complete model was considered to provide the correct result and it was used to check the accuracy of the other simplified models. The replacement of the catalyst phase model by an effectiveness factor estimated by the generalized Thiele modulus (called model C) provided identical results when compared to the most complete model. Moreover, the other simplified models provided good results with exception of the model in which the solid phase model is completely neglected. Therefore, intraparticle diffusion should be considered due to its great effect on the temperature and concentration profile along the reactor. The possibility of simplifying model C was considered by either reducing the model to 1D or neglecting the momentum balance. Reducing model C to just one dimension resulted in great temperature difference along the reactor bed and it was disregarded. Removing the momentum balance from the model was also not recommended. Finally, using model C, the MR has a great advantage over the HTSR achieving almost 100% CO conversion while the former achieved only 60% for the considered operating condition.

From the literature review presented in this section, heterogeneous models are dominant because they consider both the gas and the solid phase separately, taking into account intraparticle diffusion, which seems to limit the reaction kinetics. The pseudo-homogeneous model does not consider this phenomenon, except when an effectiveness factor is introduced in the reaction rate term, which could lead to small deviations from a rigorous heterogeneous model, but make the resulting model simpler to be solved. Studies considering operation with integrated heat exchange for the WGSR are scarce in the literature despite the better performance over the adiabatic mode as shown by Pasel et al. (2005) and by Francesconi et al. (2007), which considered heat loss to the environment in their study. Finally, all studies encountered consider ideal gas behavior, which might not be valid for industrial applications due to the elevated operational pressure.

3.6 Cooling fluids

Besides water and air, there is a vast variety of thermal oils commercially available that can be used as cooling media for reactors. The ideal fluid must be nontoxic, nonflammable, stable at the operating temperature, it must have a high heat capacity (for non-vaporizing operation) or high heat of vaporization (for vaporizing operation) and a low viscosity to minimize pressure drop and pumping work.

Vaporizing fluids are used to ensure a more uniform temperature throughout the bed length. In addition, since the heat of vaporization is higher than the sensible heat, the required mass flow of a boiling fluid tends to be smaller than the non-vaporizing one. The drawbacks of using vaporizing fluids are the possibility of cavitation and pitting corrosion (Eigenberger and Ruppel, 2012).

For operating temperatures up to 300 °C, oil and water are indicated (vaporizing or non-vaporizing). The most common vaporizing fluid is water due to its non-flammability. Nevertheless, the operating pressure might pose a limit for boiling fluid application. For example, at 250 °C water boils at approx. 4,000 kPa, thus the reactor vessel must withstand this pressure which requires its wall to be thick, increasing its cost. For temperatures above 300 °C molten salts are commonly used. Molten salts are also non-flammable but they might solidify if the temperature drops and some of them might cause corrosion issues (Eigenberger and Ruppel, 2012).

In addition, not only a suitable cooling fluid must be selected, but also the opportunity of using the heat removed from the reactor for other purposes must be considered in order to mitigate energy consumption inside any chemical plant.

3.7 Economic Analysis

The cost estimation is as important as the design, construction, and operation of any plant. When its poorly performed, it might cause the ruin of the entire project. The NPV is a suitable method for determining whether the project is economically feasible or not. It is calculated according to Eq. 3.7.1, where t_p is the project life time, i is the interest rate and CF is the cash-flow of the jth year (Towler and Sinnott, 2012).

$$\mathrm{NPV} = \sum_{j=0}^{t\mathrm{p}} \frac{\mathrm{CF}_j}{(1+i)^j} \tag{3.7.1}$$

The CF is calculated according to Eq. 3.7.2, where IT is the income tax, S is the value received due to product sales, TCP is the Total Cost of Production, D is the plant depreciation and TCI is the Total Capital Investment, which enters in the cash flow usually in the first 2 years during the plant construction (Seider et al., 2003).

$$\mathrm{CF} = (1 - IT)\,(S - \mathrm{TCP} - D) + D - \mathrm{TCI} \tag{3.7.2}$$

3.7.1 Total Capital Investment (TCI)

For the construction of new plants, the total capital investment estimation begins with the calculation of the equipment purchase costs. This part is probably the most important because all the subsequent costs are estimated based on it. The most reliable manner of obtaining the equipment costs is contacting manufactures. However, this is time-consuming and, for research purposes, manufacturers rarely supply the requested information. The alternative is to appeal to the literature, where a vast source of publications provide a good database for the cost estimation. According to Towler and Sinnott (2012), this type of evaluation has an accuracy of ±30%.

To estimate the equipment costs, there are some parametric equation available in the literature, e.g., Eq. 3.7.3 (Turton et al., 2012). Other similar equations can be found in Seider et al. (2003) and Towler and Sinnott (2012).

$$\log_{10} C_\mathrm{p} = K_1 + K_2 \log_{10} A + K_3 \left(\log_{10} A\right)^2 \tag{3.7.3}$$

where C_p is the purchase cost (US\$), K_i are parameters and A is a size factor.

The cost estimated by Eq. 3.7.3 is for a base case, i.e., carbon steel is usually the material of construction and the equipment is supposed to operate at atmospheric pressure. If the pressure is different from atmospheric and the material of construction is not carbon steel, the resulting cost difference is taken into account by using material (F_M) and pressure (F_P) factors. In addition, the cost related to equipment transportation and installation is also assessed using factors (B_1 and B_2) as shown in Eq. 3.7.4 (Turton et al., 2012).

$$C_\mathrm{BM} = C_\mathrm{p} \left(B_1 + B_2 F_M F_P\right) \tag{3.7.4}$$

where C_BM is the bare module cost (US\$).

The cost estimated by Eq. 3.7.4 is for a specific base year. For the present year, the inflation effect on the equipment cost must be taken into account. This is done by using inflationary indexes (I) such those released every month by the Chemical Engineering Plant Cost Index (CEPCI). Therefore, the real equipment cost C_R is calculated according to Eq. 3.7.5 (Towler and Sinnott, 2012).

$$C_\mathrm{R} = \frac{I_\text{present year}}{I_\text{base year}} C_\mathrm{BM} \tag{3.7.5}$$

The summation of real cost of each equipment yields the installed cost, which is also known as Inside Battery Limits (ISBL). The costs of auxiliary equipment such as cooling towers, boilers and power lines are known as Outside Battery Limits (OSBL) and its value varies from 20% to 50% of the ISBL. Other costs are Engineering Costs (EC) (from 10% to 30% of ISBL + OSBL), Contingency Costs (CC) (from 10% to 50% of ISBL + OSBL) and start-up costs (from 2% to 30% of ISBL + OSBL + EC + CC). The summation of all theses costs yields the total capital investment (Seider et al., 2003; Towler and Sinnott, 2012).

3.7.2 Total Cost of Production (TCP)

The TCP is the summation of the variable cost of production, which accounts for the raw material cost and utilities cost, and the fixed cost of production. Ulrich and Vasudevan (2006) presents a good methodology to estimate the utilities cost. Base values for utilities are also presented by Seider et al. (2003), Towler and Sinnott (2012), and Turton et al. (2012). The fixed cost of production is the summation of the labor cost (C_{L}), maintenance cost (C_{M}) and benefits and training (C_{BT}). The C_{L} per annum can be estimated according to Eq. 3.7.6, where (C_{SA}) is the annual salary (US$) payed to each employee, U_{S} is the number of process units handling solids and U_{F} is number of process units handling fluids. The C_{M} varies from 3% to 5% of the ISBL and C_{BT} varies from 40% to 60% of C_{L} (Seider et al., 2003; Turton et al., 2012).

$$C_{\mathrm{L}} = 4.5\sqrt{6.29 + 31.7U_{\mathrm{S}}^2 + 0.23U_{\mathrm{F}}}\, C_{\mathrm{SA}} \tag{3.7.6}$$

Chapter 4

Model Development, Simulation and Optimization

This chapter begins with a description of the reactor arrangement used to conduct the WGSR and its cooling system. The next section shows the catalyst particle model, how it is solved and how the effectiveness factor is used to replace it in the reactor's model. In addition, a discussion about mass and heat transfer limitation inside the catalyst and from the catalyst particle to the bulk fluid and vice-versa is made. In Sec. 4.4, the reactor model composed by the material, energy and momentum balances is developed. The model is validated against both experimental and industrial data and it is afterwards simulated. In the last section (Sec. 4.7) the reactor design procedure is presented. The design is accomplished by means of and optimization procedure, which aims at minimizing both the reactor's capital and operational costs.

All models developed in this chapter were implemented in MATLAB®. MATLAB®'s programming language is relatively easy to be understood and can be both procedural and object-oriented. In addition, the software has excellent tools for solving differential equations, algebraic equations system and optimization problems. Despite being a commercial software, it can be considered accessible to students and it is world-wide used.

4.1 Reactor Arrangement

The proposed reactor arrangement is shown in Fig. 4.1. The reacting gases enter the multitubular reactor at the top and flow downwards through the tubes filled with the catalyst, which are immersed in the cooling fluid. Water is chosen to be the reactor cooling fluid due to its temperature operating level (150°C - 250°C), because it is inexpensive compared to thermal oils, non-corrosive, non-toxic, non-flammable and promptly available. Water forms a pool boiling around the tubes. The vapor bubbles flow upwards due to the difference of density until the vapor-liquid separator. The saturated steam is condensed in the heat exchanger, where the coolant to be used is the power cycle's working fluid as discussed in Part II.

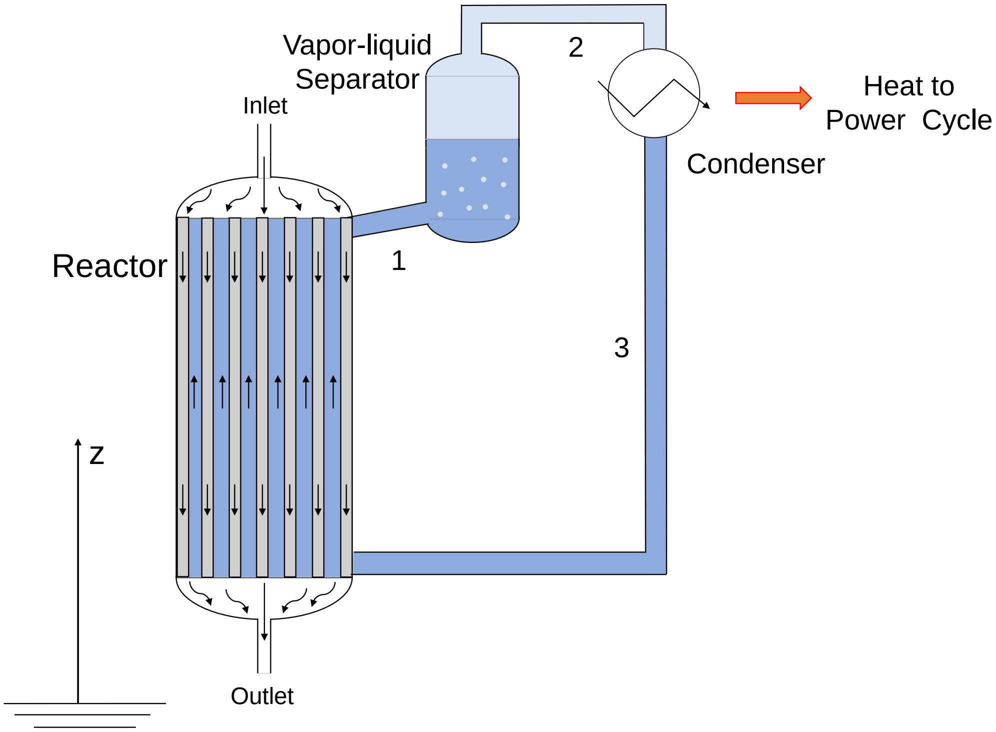

Figure 4.1: Multitubular reactor with integrated heat exchange.

4.2 Catalyst Particle Model

Considering the literature review in the previous chapter, the most accurate model for a catalytic reactor should be a 2D heterogeneous model, in which the mass and the energy balances inside the catalytic particle are considered along with the reactor model. This occurs because the reaction rates in the literature are intrinsic, i.e., the experimental procedures to determine the reaction rates were conducted in such a manner that the influence of mass and heat transfer from the bulk fluid to the catalyst surface (using an elevated GHSV) and to its pores (crushing the catalyst particle to very small diameters, usually μm) could be neglected (Nauman, 2008). However, as reported by Marín et al. (2012), the solution of the 2D heterogeneous model requires a considerable amount of computing time since a set of nested differential equations must be solved simultaneously. One alternative to avoid solving the catalyst particle model along with the reactor model is to find the actual reaction rate

(r). The actual reaction rate is related to the intrinsic reaction rate (r_{int}) by a dimensionless effectiveness factor (η) (Nauman, 2008). Using this alternative, the catalyst particle model still needs to be solved, but it can be solved for several different conditions in the bulk gas phase and η can afterwards be estimated.

The development of the catalyst particle model departs from Eqs. 3.5.2 and 3.5.3. To obtain the final model, the following assumptions were made:

1. Peng-Robinson-Stryjek-Vera Equation of State (PRSV-EoS) (Stryjek and Vera, 1986) is used to describe the gas mixture;
2. The system is considered to be at steady-state. Therefore, the terms $\frac{DT}{Dt}$ and $\frac{DP}{Dt}$ become $\left(\vec{v} \cdot \nabla T\right)$ and $\left(\vec{v} \cdot \nabla P\right)$, respectively;
3. The fluid inside the catalyst pore is stagnant. Therefore, $\vec{v} \approx 0$. This also implies that the ith component is only transported inside or outside the catalyst particle by mass diffusion. Fick's first law of diffusion is used to calculate the molar flux;
4. Heat is transported inside or outside the catalyst particle by thermal conduction. Fourier's law of heat conduction is used to calculate the heat flux;

In addition to the aforementioned assumption, the catalyst particle is also assumed to have spherical shape (Fig. 4.2). Assuming that the dependent variables vary only in the radial coordinate as represented in Fig. 4.2, the final particle model is obtained.

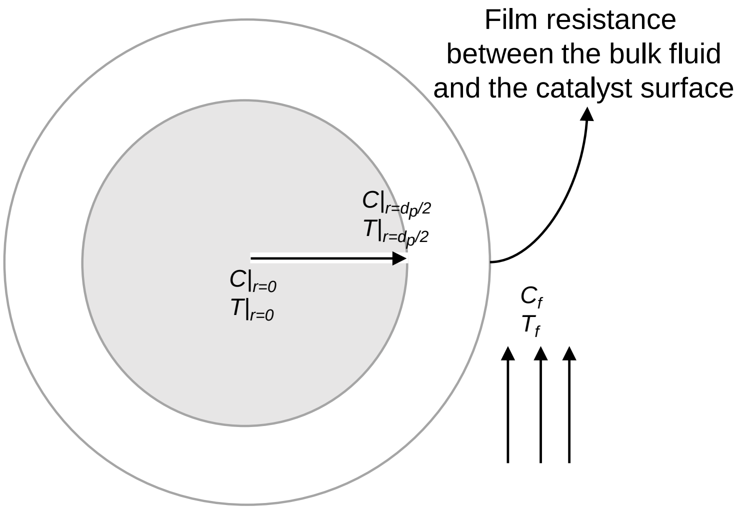

Figure 4.2: Catalyst particle (Adapted from Nauman, 2008).

$$\frac{1}{r^2}\frac{\mathrm{d}}{\mathrm{d}r}\left(r^2 \mathscr{D}_{\text{eff}_i}\frac{\mathrm{d}C_i}{\mathrm{d}r}\right) + \nu_i r_{\text{int}} = 0 \tag{4.2.1}$$

$$\frac{\mathrm{d}C_i}{\mathrm{d}r}\Big|_{r=0} = 0 \qquad -\mathscr{D}_{\mathrm{eff},i}\Big|_{r=d_p/2}\frac{\mathrm{d}C_i}{\mathrm{d}r}\Big|_{r=d_p/2} = \kappa_i\left(C_i\Big|_{r=d_p/2} - C_{\mathrm{f},i}\right)$$

$$\frac{1}{r^2}\frac{\mathrm{d}}{\mathrm{d}r}\left(r^2\lambda_{\mathrm{eff}}\frac{\mathrm{d}T}{\mathrm{d}r}\right) + \left(-\Delta_{\mathrm{r}}h\right)r_{int} = 0 \tag{4.2.2}$$

$$\frac{\mathrm{d}T}{\mathrm{d}r}\Big|_{r=0} = 0 \qquad -\lambda_{\mathrm{eff}}\frac{\mathrm{d}T}{\mathrm{d}r}\Big|_{r=d_p/2} = h\left(T\Big|_{r=d_p/2} - T_{\mathrm{f}}\right)$$

where C_i is the concentration of the ith component (kmol·m^{-3}). N_2 and CH_4 are inerts encountered in the syngas mixture. Therefore, they are also taken into account. The subscript "f" refers to the bulk fluid phase. The effective diffusion of the ith component ($\mathscr{D}_{\mathrm{eff}}$)(m^2·s^{-1}) is calculated according to Eq. B.1.1 in Appendix B.1.1.

As presented the literature review and examining Fig. 3.1, the CO conversion is favored at low temperatures. For low temperature operation, the most suitable catalyst is Cu-based. Therefore, Moe's intrinsic reaction rate (r_{int}) (Eq. 4.2.3), whose parameters were estimated by Choi and Stenger (2003) is used in this work. The parameters were estimated based on results obtained from experiments with a commercial Cu-based catalyst in the temperature range of 120 °C - 250 °C.

$$r_{\mathrm{int}} = F_p\rho_s(1-\varepsilon_{\mathrm{p}})2.96\times10^5\exp\left(\frac{-47400}{R_{\mathrm{g}}T}\right)\left(y_{\mathrm{CO}}y_{\mathrm{H_2O}} - \frac{y_{\mathrm{CO_2}}y_{\mathrm{H_2}}}{K}\right) \tag{4.2.3}$$

where T is in K, P_i is the partial pressure of the ith component (atm), r_{int} is in kmol·m^{-3}·h^{-1} and ρ_s is the solid catalyst particle density (5,904 kg·m^{-3}) (Adams II and Barton, 2009; Choi and Stenger, 2003). Eq. 4.2.3 was developed at atmospheric pressure. According to Adams II and Barton (2009), Eq. 4.2.3 under predicts the reaction rate at higher pressures. Therefore, a pressure correction factor needs to be used F_p (Eq. 4.2.4). This factor multiplies the reaction rate and it is valid up to 55 atm (55.73 bar) (Adams II and Barton, 2009).

$$F_p = P^{\left(0.5-\frac{P}{500}\right)} \tag{4.2.4}$$

In this work a stagnant film resistance involving the catalyst particle is considered (Fig. 4.2). The mass flux of the jth component from the bulk fluid to the catalyst particle surface and vice-versa is proportional to the concentration difference at the end points of the film and to the mass transfer coefficient (κ_j) (m·s^{-1}). κ_j can be found through the Sherwood number (*Sh*) as shown in Appendix B.2.

The analogy used to calculate κ can be extended to calculate the convective heat transfer coefficient (h) (W·m^{-1}·K^{-1}). h is calculated through the Nusselt number $\left(Nu = \frac{d_{\mathrm{f}}h}{\lambda_{\mathrm{f}}}\right)$. *Nu* replaces *Sh* in Eq. B.2.1 so as the Prandtl number $\left(Pr = \frac{c_{p\mathrm{f}}\mu_{\mathrm{f}}}{\lambda_{\mathrm{f}}}\right)$ replaces *Sc* in the same equation (Iordanidis, 2002). The fluid viscosity (μ_{f}) and fluid thermal conductivity (λ_{f}) are calculated as shown in Appendix B.3 and B.4, respectively.

The effective thermal conductivity of the catalyst particle (λ_{eff} (W·m^{-1}· K^{-1})) is assumed to be 0.43 W·m^{-1}·K^{-1}. The correlations for predicting λ_{eff} are not as developed as those used to estimate $\mathscr{D}_{\text{eff}}$. However, selecting a value for λ_{eff}, which may be very close to the real one, is possible because it ranges from approx. 0.1 Btu·h^{-1}·°F^{-1}·ft^{-1} (0.17 W·m^{-1}·K^{-1}) to 0.4 Btu·h^{-1}·°F^{-1}·ft^{-1} (0.69 W·m^{-1}·K^{-1}) (Smith, 1970). Therefore, an average value is chosen in this work.

The catalyst particle model cannot be solved analytically due to the form of r_{int}. The numerical procedure used to solve them is discretization by Orthogonal Collocation (OC) (See Appendix C) followed by any method able to find the roots of the resulting algebraic equations. In this work, the model is implemented in MATLAB® 2019b and the function *fsolve* is used to solve it. The discrete catalyst particle model implemented in MATLAB® is available in Appendix A.1.

4.2.1 Catalyst Particle Model Simulation

The catalyst particle model was solved and the result is depicted in Fig. 4.3. 10 internal collocation points were found to be enough to achieve a stable solution, i.e., increasing the number of points did not cause any change in the concentration and temperature profiles.

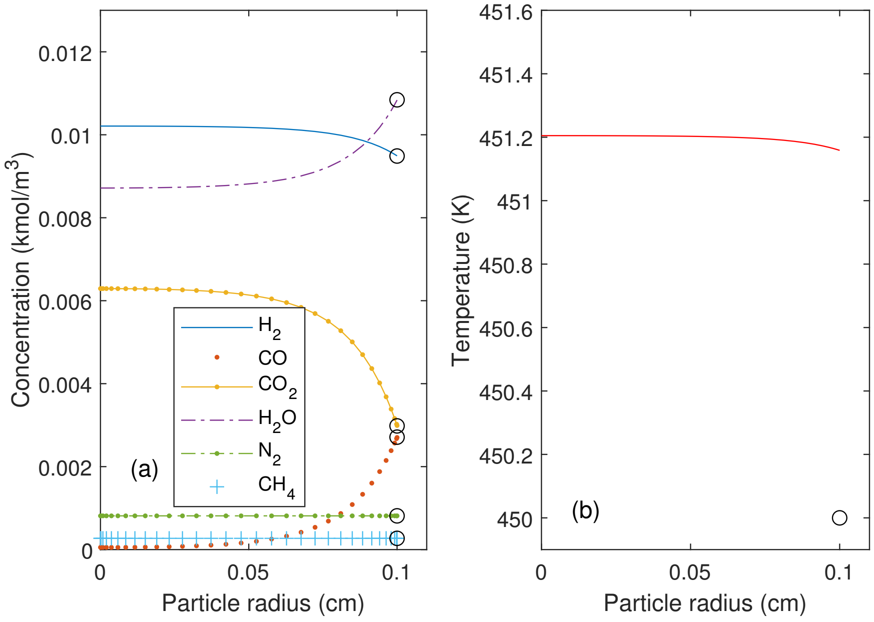

Figure 4.3: Catalyst particle model solution. Bulk fluid condition: $T = 450$ K, $P = 1$ atm, $y_{H_2} = 0.35$, $y_{CO} = 0.1$, $y_{CO_2} = 0.11$, $y_{H_2O} = 0.4$, $y_{N_2} = 0.03$, $y_{CH_4} = 0.01$, $d_p = 2 \times 10^{-3}$ m and $v = 0.6$ m/s. The marker 'o' represents the bulk fluid value.

The effect of the film resistance, although not very pronounced in the concentration profile (Fig. 4.3-a), may be perfectly noticed on the temperature profile (Fig. 4.3-b) where the temperature of the bulk fluid is 1.2 K below the temperature of the catalyst particle surface. However, the mass diffusion effect inside the particle is more evident than that of the thermal conductivity. This leads to the conclusion that heat transfer resistance inside the particle is considerably lower than the mass transfer resistance but, in the film formed around the particle, the resistances change roles, i.e., the mass transfer resistance is lower than the heat transfer resistance. The combined effect of both mass and heat transfer resistances yields an effectiveness factor (η) of 0.35 for this case. In addition, it is possible to notice that H_2 diffuses considerably faster than the other components. CH_4 and N_2 concentrations are constant because they are inert.

4.3 Effectiveness Factor

To minimize the computation time, the catalyst particle model is not coupled with the reactor model in this work. Rather, it is solved for several bulk fluid conditions and the effectiveness factor (η) is estimated to account for mass and heat transfer limitations between the solid and the fluid phases. The conditions for which η was estimated are presented in Table 4.1.

Table 4.1: Set of variables range used to estimate η.

Molar fraction	Temperature (K)	Particle diameter (mm)	Bulk fluid velocity (m/s)
End points are 0.001 and 0.997 with internal points from 0.1 to 0.9 increasing by 0.1	From 423.15 to 523.15 increasing by 10	From 2 to 10 increasing by 2	From 0.1 to 1.9 increasing by 0.3

The components considered in the mole fraction calculation are those involved with the reaction, i.e., H_2, CO, CO_2 and H_2O. Firstly, the mole fractions for each component (except H_2O) were expanded from 0.001 to 0.997. The H_2O mole fraction was then calculated based on the constraint that the summation of all fractions must be equal to unity. Secondly, the resulting combinations in which the water mole fraction was negative were removed. In addition, combinations resulting in H_2O/CO molar ratios smaller than 1 or grater than 8 were also removed. H_2O/CO molar ratios lying out of the aforementioned range are not desirable for performing the WGSR as can be seen in Fig. 3.1. Finally, after this procedure a total of 88 combinations were found.

The temperature range was selected based on the usual operating temperature of reactors with Cu-based catalysts (See Section 3.2). The catalyst particle diameter range represents the usual size in which commercial catalyst are supplied (Nauman, 2008). The velocity range was chosen based on the operating velocities found on literature (Chen et al., 2008; Choi and Stenger, 2003; Ding and Chan, 2008). The combination of all variables results in a total of 33,880 different conditions, i.e., the catalyst particle model must be solved 33,880 times.

Since the reaction is considered to occur only in the presence of the catalyst, the real reaction rate (r) must be equal to the rate of consumption/generation of the ith component at the solid surface (Nauman, 2008).Therefore:

$$r = a_v \kappa_i \left(C_i|_{r=d_p/2} - C_{\mathrm{f},i} \right) \tag{4.3.1}$$

where a_v is the catalyst particle surface area per unit volume (m^{-1}), which is equal to $d_\mathrm{p}/6$ for a sphere.

After solving the catalyst particle model, the concentration of the ith component at the solid surface ($C_i|_{r=d_p/2}$) is determined. Therefore, the real reaction rate (Eq. 4.3.1) and η can be calculated (Eq. 4.3.2).

$$\eta = \frac{r}{r_{\mathrm{int}}|_{\text{at bulk fluid condition}}} \tag{4.3.2}$$

At this point, a reference model is proposed (Eq. 4.3.3). This model contains a_is parameters which are estimated in MATLAB® 2019b by the function *nlinfit*, which minimizes the square difference between the ‘real’ value of η obtained by Eq. 4.3.2 and the value predicted by Eq. 4.3.3 by changing the a_i values. The parameters whose effects on the final value of the objective function can be neglected will be removed from the model.

$$\begin{aligned} \eta = & a_0 + a_1 y_{\mathrm{H_2}} + a_2 y_{\mathrm{CO}} + a_3 y_{\mathrm{CO_2}} + a_4 y_{\mathrm{H_2O}} + a_5 T + a_6 T^2 + a_7 v + a_8 v^2 \\ & + a_9 y_{\mathrm{H_2}} T + a_{10} y_{\mathrm{CO}} T + a_{11} y_{\mathrm{CO_2}} T + a_{12} y_{\mathrm{H_2O}} T + a_{13} d_\mathrm{p} + a_{14} d_\mathrm{p}^2 \end{aligned} \tag{4.3.3}$$

Using Eq. 4.3.3 along with Eq. 4.2.3, the real reaction rate can be estimated and the catalyst participle model is not necessary anymore.

4.3.1 Effectiveness Factor Surrogate Model

The catalyst particle model was solved for each condition presented in Table 4.1 and the value of η was calculated according to Eq. 4.3.2. With the values of η, the parameters of Eq. 4.3.3 were estimated. It was not possible to obtain a good data fitting using only one model. Therefore, for each particle diameter one model was obtained. Although the models have the same form (Eq. 4.3.4), the parameters values are different (Table 4.2). The correlation coefficient (R) obtained for each model was greater than 0.98 as shown in Fig. 4.4.

$$\eta = a_0 + a_1 y_{\mathrm{CO}} + a_2 y_{\mathrm{H_2O}} + a_3 T + a_4 T^2 + a_5 v + a_6 T y_{\mathrm{CO}} + a_7 T y_{\mathrm{H_2O}} \tag{4.3.4}$$

Table 4.2: Surrogate model parameters.

d_p (cm)	a_0	a_1	a_2	$a_3 \times 10^2$	$a_4 \times 10^5$	$a_5 \times 10^3$	$a_6 \times 10^4$	$a_7 \times 10^3$
0.2	7.0664	-0.52659	-1.3578	-2.3780	2.0483	-5.7154	9.8536	2.3091
0.4	4.7457	-0.23600	-1.0287	-1.6267	1.4190	-6.2692	4.6615	1.8292
0.6	3.4221	-0.00722	-0.7348	-1.1782	1.0316	-5.6479	0.0434	1.3021
0.8	2.7647	0.08149	-0.5713	-0.9599	0.8475	-4.6977	-1.8208	1.0068
1.0	2.4002	0.08746	-0.4833	-0.8417	0.7496	-3.7653	-1.9866	0.8525

From the parameter estimation, the effect of the H_2 and CO_2 mole fractions were negligible. Therefore, the terms containing these variables were removed. The bulk fluid velocity has also a small linear effect on η. The combined effect between T and CO and H_2O molar fractions were observed. Other combined effects between T, mole fractions and velocity were tested but they can be considered irrelevant due to the negligible increase of the correlation coefficient. Finally, increasing the size of the catalyst particle decreases the effectiveness factor.

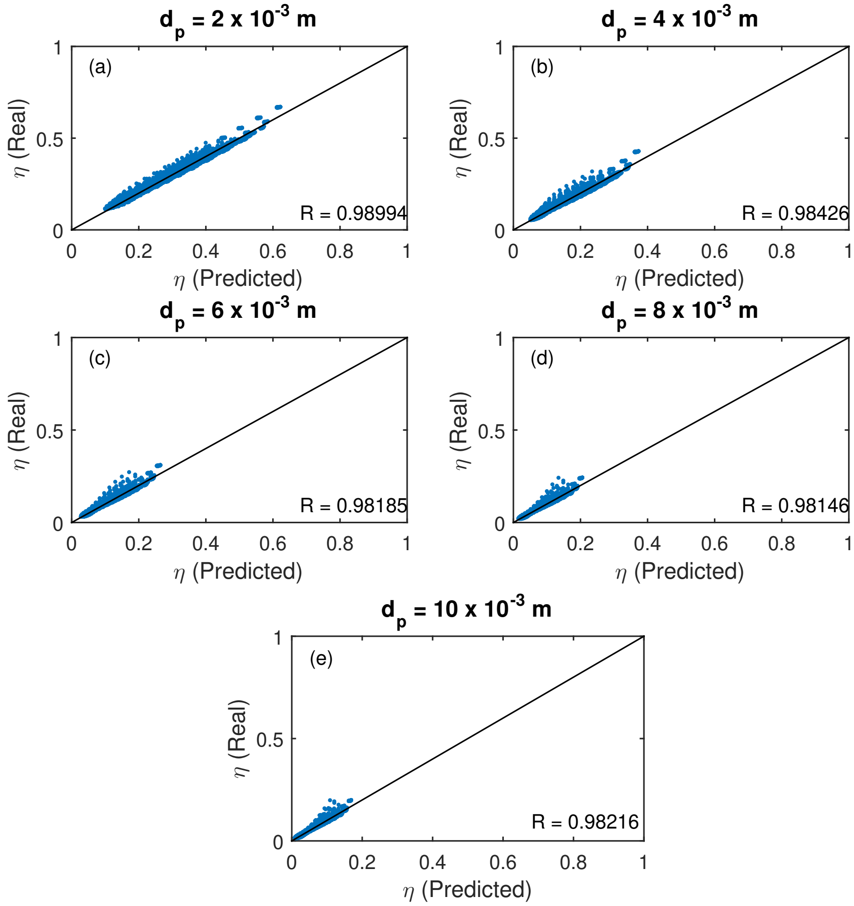

Figure 4.4: Comparison between η from Eq. 4.3.4 (Predicted) with η from Eq. 4.3.2(Real)

.

4.4 Reactor Model

4.4.1 Momentum Balance

The following assumptions were made to simplify the general momentum balance (Eq. 3.5.4):

1. Newtonian fluid behavior. The stress components are given by Stokes' correlations;
2. Fluid viscosity variation along with the reactor position is neglected. According to Hunt and Tien (1988), for a narrow temperature range, the viscosity can be assumed constant since the fluid are gases.
3. Fluid compressibility effect on the velocity field is negligible. The Mach Number for catalytic reactors is lower than 0.3 (Chanson, 1996).

With the assumptions made so far, Eq. 3.5.4 reduces to:

$$\rho_{\mathrm{f}}\frac{D\vec{v}}{Dt} = -\nabla P + \mu\nabla^{2}\vec{v} + \rho\vec{g} \tag{4.4.1}$$

4. Quasi steady state. The velocity response to any disturbance is considerably faster than the temperature and the concentration responses. Therefore $\frac{\partial v}{\partial t} \approx 0$;
5. Symmetry in the angular coordinate;
6. From the simulation of a 2D momentum balance, Papageorgiou and Froment (1995) reported radial velocity only from the reactor's entrance up to 4% of its total length. Therefore, radial velocity is neglected in this work;

After these simplifications, Eq. 4.4.1 can be rewritten as:

$$\rho_{\mathrm{f}} v_z \frac{\partial v_z}{\partial z} = \rho_{\mathrm{f}} g_z - \frac{\partial P}{\partial z} + \mu_{\mathrm{f}}\left[\frac{1}{r}\frac{\partial}{\partial r}\left(r\frac{\partial v_z}{\partial r}\right) + \frac{\partial^2 v_z}{\partial z^2}\right] \tag{4.4.2}$$

With the aid of the continuity equation (Eq. 3.5.1) and assumption #3, #5 and #6, $\frac{\partial v_z}{\partial z} = 0$. In addition, the superficial velocity ($v = \varepsilon v_z$) is introduced along with the friction factor given by Ergun to account for head loss due to flow through the solid catalyst bed (Froment et al., 2011). Therefore, the momentum balance can be written as:

$$\frac{\partial P}{\partial z} = \rho_{\mathrm{f}} g_z + \frac{\mu_{\mathrm{f}}}{\varepsilon}\left[\frac{1}{r}\frac{\partial}{\partial r}\left(r\frac{\partial v}{\partial r}\right)\right] - \frac{150\,(1-\varepsilon)^2\,\mu_{\mathrm{f}} v}{\varepsilon^3 d_{\mathrm{p}}^2} - \frac{1.75\,(1-\varepsilon)\,v^2\rho_{\mathrm{f}}}{\varepsilon^3 d_{\mathrm{p}}} \tag{4.4.3}$$

$$\frac{\partial v}{\partial r}\Big|_{r=0} = 0 \qquad v\big|_{r=R} = 0$$

Eq. 4.4.3 is a simplified version of the extended Brinkman's equation (Dong, 2018; Marín et al., 2012; Tsotsas, 2010). The bed void fraction (ε) varies along with the radial position. This variation is taken into account by Giese's correlation (Eq. 4.4.4) (Tsotsas, 2010).

$$\varepsilon = 0.4\left[1 + 1.36\exp\left(-5\frac{R-r}{d_{\mathrm{p}}}\right)\right] \tag{4.4.4}$$

Since the velocity varies only in the radial coordinate, the term $\frac{\partial P}{\partial z}$ is constant. Therefore, to solve the model the procedure depicted in Fig. 4.5 is used. The discrete momentum balance obtained after applying OC to the radial coordinate (Appendix A.2.1) was implemented in MATLAB® 2019b and the function *fsolve* was used to solve it.

4.4.2 Energy Balance

The following assumptions were made to simplify the general energy balance (Eq. 3.5.3):

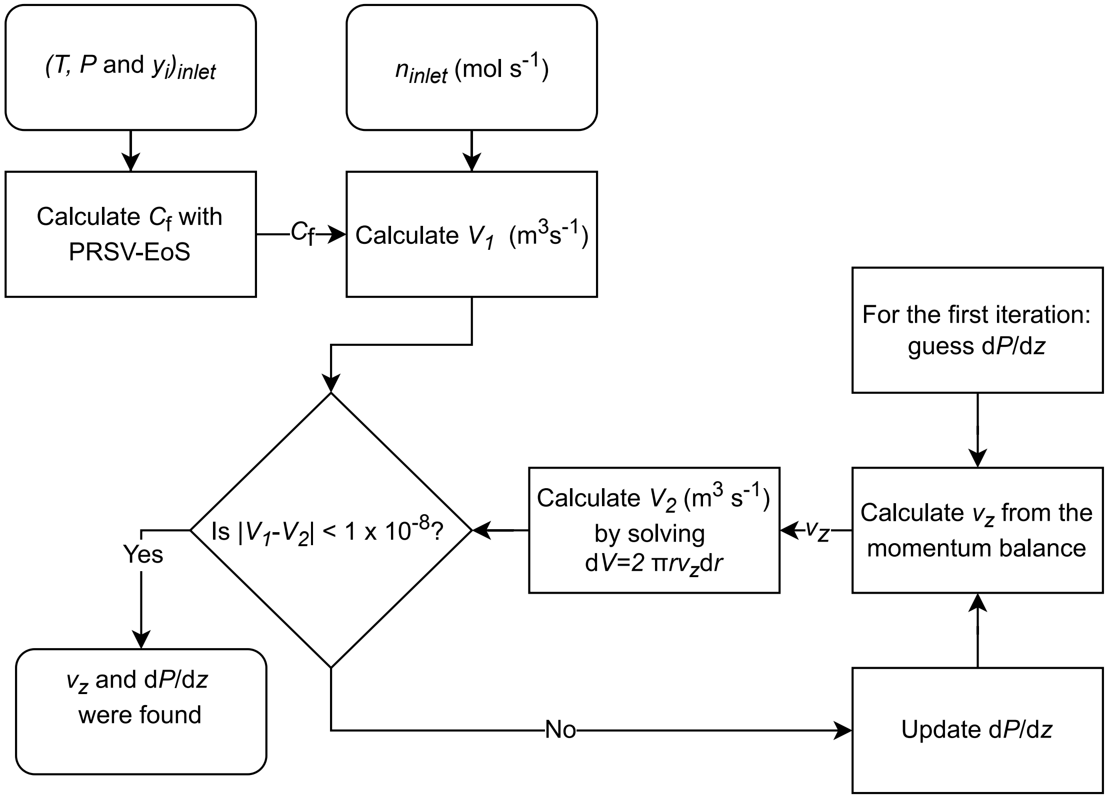

Figure 4.5: Procedure to find the the fluid flow velocity profile and pressure drop.

7. The viscous dissipation effect on the temperature is negligible, i.e., $\vec{\vec{\tau}} : \nabla \vec{v} \approx 0$ (Bird et al., 2002);

8. Fourier's law of heat conduction is used to calculate the heat flux;

In addition, considering assumptions #5 and #6, the final energy balance may be written as:

$$\begin{aligned}\left(\varepsilon C_{\mathrm{f}} c_{p_{\mathrm{f}}} + (1-\varepsilon)\,\rho_{\mathrm{s}} c_{p_{\mathrm{s}}}\right)\frac{\partial T}{\partial t} = & - C_{\mathrm{f}} c_{p_{\mathrm{f}}} v \frac{\partial T}{\partial z} + \frac{1}{r}\frac{\partial}{\partial r}\left(\lambda_r r \frac{\partial T}{\partial r}\right) + \frac{\partial}{\partial z}\left(\lambda_z \frac{\partial T}{\partial z}\right) \\ & - v\frac{T}{C_{\mathrm{f}}}\left(\frac{\partial C_{\mathrm{f}}}{\partial T}\right)_P \frac{\partial P}{\partial z} + (-\Delta h_{\mathrm{r}})(1-\varepsilon)\,\eta r_{\mathrm{int}}\end{aligned} \tag{4.4.5}$$

$$\left[c_{p_{\mathrm{f}}} T \frac{\dot{n}}{A_{\mathrm{t}}} + \frac{\dot{n}T}{A_{\mathrm{t}} C_{\mathrm{f}}^2}\left(\frac{\partial C_{\mathrm{f}}}{\partial T}\right) P\right]_{inlet} = \left[C_{\mathrm{f}} c_{p_{\mathrm{f}}} T v + v\frac{T}{C_{\mathrm{f}}}\left(\frac{\partial C_{\mathrm{f}}}{\partial T}\right)_P P - \lambda_z \frac{\partial T}{\partial z}\right]_{z=0} \qquad -\lambda_z \frac{\partial T}{\partial z}\Big|_{z=L} = 0$$

$$-\lambda_r \frac{\partial T}{\partial r}\Big|_{r=0} = 0 \qquad -\lambda_r \frac{\partial T}{\partial r}\Big|_{r=d_{\mathrm{r}/2}} = \ddot{q}$$

where $\dot{n}$ is the feed molar flow (kmol·s^{-1}), C_f is the total fluid concentration (kmol·m^{-3}), A_t is the reactor tube cross sectional area (m^2) and the subscript "f" stands for the fluid phase. The term $\left(\frac{\partial C_\mathrm{f}}{\partial T}\right)_P$ is derived in Appendix B.5.The real gas (c_{p_f}) and the enthalpy of reaction ($\Delta_\mathrm{r} h$) are calculated according to what is stated in Appendix B.6 and B.7.

The effective radial (λ_r) and axial (λ_z) heat conduction coefficients (W·m^{-1}·K^{-1}) are determined according to Eqs. 4.4.6 and 4.4.7 (Markatos et al., 2005). Both equations are represented by the sum of the static contribution (λ^0 (Eq. 4.4.8)), i.e., thermal conductivity of the bed without fluid flow, and the dynamic contribution (λ_r^D (Eq. 4.4.9) and λ_z^D (Eq. 4.4.10)), i.e., thermal conductivity of the bed due to fluid flow (Markatos et al., 2005).

$$\lambda_r = \lambda^0 + \lambda_r^D \tag{4.4.6}$$

$$\lambda_z = \lambda^0 + \lambda_z^D \tag{4.4.7}$$

$$\lambda^0 = \lambda_\mathrm{f} \left(\frac{\lambda_\mathrm{eff}}{\lambda_\mathrm{f}}\right)^{\left[0.28 - 0.757 \log_{10}(\varepsilon) - 0.057 \log_{10}\left(\frac{\lambda_\mathrm{eff}}{\lambda_\mathrm{f}}\right)\right]} \tag{4.4.8}$$

$$\lambda_r^D = \frac{\lambda_\mathrm{f} Re Pr}{8.65 \left[1 + 19.4 \left(\frac{d_\mathrm{p}}{d_\mathrm{t}}\right)^2\right]} \tag{4.4.9}$$

$$\lambda_z^D = \frac{\lambda_\mathrm{f} Re Pr}{1.4} \tag{4.4.10}$$

where $Re = \rho_\mathrm{f} d_p v / \mu_\mathrm{f}$, $Pr = c_{p_\mathrm{f}} \mu_\mathrm{f} / \lambda_\mathrm{f}$ and λ_f is calculated as stated in Appendix B.4.

At $r = d_\mathrm{t}/2$, the heat flux ($\ddot{q}$) transfered from the reacting gases to the cooling fluid must be the same. $\ddot{q}$ is estimated according to Eq. 4.4.11, where T_cf is the cooling fluid temperature and U is the overall heat transfer coefficient (W·m^{-2}·K $^{-1}$). Since the cooling fluid is pure and it is assumed to be changing phase, its temperature is constant. U is assumed to be equal to 30 (W·m^{-2}·K $^{-1}$). According to Roetzel and Spang (2010), U typically ranges from 15 to 50 W·m^{-2}·K $^{-1}$ when heat exchange takes place between hot gases and a boiling fluid.

$$\ddot{q} = U \left(T|_{r=d_{\mathrm{t}/2}} - T_\mathrm{cf} \right) \tag{4.4.11}$$

To solve the energy balance, forward first order finite differences are applied to approximate the first order derivatives in the axial coordinate and the thermal conductivity coefficients derivatives; central second order finite differences are applied to approximate the second order derivative in the axial coordinate and OC is applied in the radial coordinate. The discrete energy balance can be seen in Appendix A.2.2.

4.4.3 Material Balance

With the aid of the assumptions #3, #5 and #6 and the continuity equation, the component material balance (Eq. 3.5.2) reduces to:

$$\frac{\partial C_i}{\partial t} = -v\frac{\partial C_i}{\partial z} + \frac{1}{r}\frac{\partial}{\partial r}\left(j_{r,i}r\right) + \frac{\partial}{\partial z}\left(j_{z,i}\right) + \nu_i\left(1-\varepsilon\right)\eta r_{\mathrm{int}} \tag{4.4.12}$$

10. Fick's first law of diffusion is used to calculate the molar flux.

$$\frac{\partial C_i}{\partial t} = -v\frac{\partial C_i}{\partial z} + \frac{1}{r}\frac{\partial}{\partial r}\left(r\,D_r\frac{\partial C_i}{\partial r}\right) + \frac{\partial}{\partial z}\left(D_z\frac{\partial C_i}{\partial z}\right) + \nu_i\left(1-\varepsilon\right)\eta r_{\mathrm{int}} = 0 \tag{4.4.13}$$

$$\left[\frac{\dot{n}_i}{A_{\mathrm{t}}}\right]_{inlet} = \left[C_i v - D_z\frac{\partial C_i}{\partial z}\right]_{z=0} \qquad - D_z\frac{\partial C_i}{\partial z}|_{z=L} = 0$$

$$-D_r\frac{\partial C_i}{\partial r}|_{r=0} = 0 \qquad - D_r\frac{\partial C_i}{\partial r}|_{r=d_r/2} = 0$$

The effective axial $D_{z,i}$ and radial $D_{r,i}$ diffusion coefficients ($\mathrm{m^2{\cdot}s^{-1}}$) of the ith component are estimated according to Eqs. 4.4.14 and 4.4.15 (Tiemersma et al., 2006). $D_{\mathrm{m},i}$ is estimated according to Wilke's correlation (Eq. B.1.4 in Appendix. B.1.1).

$$D_{z,i} = \left(1-\sqrt{1-\varepsilon}\right)D_{\mathrm{m},i} + \frac{v\,d_{\mathrm{p}}}{2} \tag{4.4.14}$$

$$D_{r,i} = \left(1-\sqrt{1-\varepsilon}\right)D_{\mathrm{m},i} + \frac{v\,d_{\mathrm{p}}}{8} \tag{4.4.15}$$

The same procedure adopted to make the discretization of the energy balance was applied to the material balance. The discrete material balance is available in Appendix A.2.3

The discrete energy and material balances are solved in MATLAB® 2019b by performing the ingratiation in time using the function *ode15s*. As initial condition, the concentration and temperature inside the reactor are assumed to be equal to the inlet temperature and concentration. The set of partial differential equations was solved with relative and absolute tolerances of 10^{-6} and 10^{-8}, respectively. All calculations were performed in a computer with a processor Intel Core i7- 3520M of 2.9 GHz and installed memory of 8 GB.

4.5 Reactor Model Validation

The model validation is accomplished in two steps in this work. The first validation takes into account the intraparticle diffusion and the mass and heat transfer between the solid catalyst and the bulk fluid by applying an effectiveness factor in the component material balances. The second validation takes into account the complete reactor model, including the energy balance. However, the effectiveness factor is not considered on this validation because the reaction rate and the factor (ψ) used already include the effects represented by η. The validation is executed in this manner because it was not found in the literature experimental data regarding a low temperature WGS reactor with integrated heat exchange. However, by achieving good results in comparison with the experimental data in both validations, it is considered that the catalyst particle model, the effectiveness factor surrogate model, the momentum balance, the component molar balances, and the energy balance developed in this work are able to represent the reality.

4.5.1 Isothermal Operation

The prediction capability of the model developed in this work was tested against the experimental data provided by Choi and Stenger (2003). The experiments were conducted in a laboratory scale reactor at constant temperature and atmospheric pressure. Since the temperature was constant, the energy balance was neglected. In addition, since the experimental conditions (laboratory scale) differ from those used to estimate the effectiveness factor, a new estimation had to be done. The procedure was the same as described in Subsection 4.3 and the resulting equation for η with the fitting results are available in Appendix E.1. The results are presented in Fig. 4.6. The H_2O/CO molar ratio was divided by a reference value. To see the real value, one should refer to Choi and Stenger (2003).

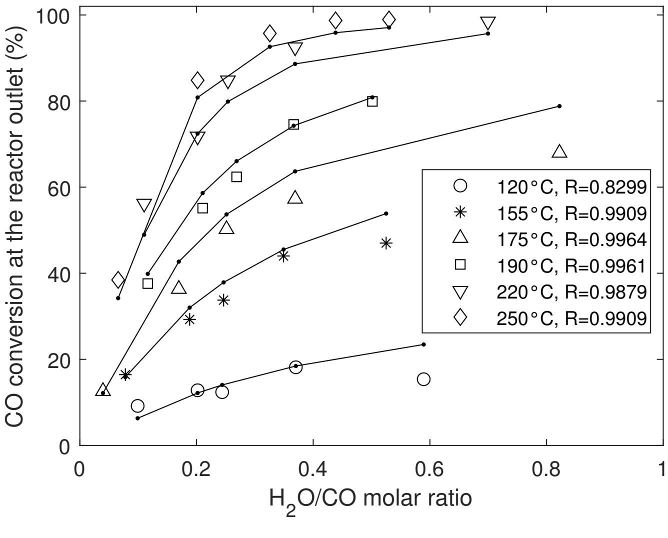

Figure 4.6: Comparison between the experimental CO conversion from Choi and Stenger (2003)(markers) and the values predicted by the model (lines).

Although some deviations are more pronounced at lower temperatures and elevated H_2O/CO molar ratios, the model can represent the reality well. The correlation coefficients (R) represent the good agreement between experimental and predicted values. The grid was considered stable for 28 points in the radial coordinate and 37 points in the axial coordinate.

4.5.2 Adiabatic Operation

The reactor model, this time including the energy balance, was tested against the industrial data provided by Elnashaie and Elshishini (1994) for 2 adiabatic high temperature WGS reactors. The reactors operate with a Fe-based catalyst due to the high temperature. Therefore, the reaction rate was that reported by Rase and Holmes (1977), which has the same form as Eq. 3.3.6, but with different constants. In addition, a factor (ψ), which considers the pressure effect on the reaction rate, is used. The reaction rate and ψ reported by Rase and Holmes (1977) were developed for a catalyst operating at industrial condition, thus, thermal and mass transfer limitation between the bulk fluid and the catalyst particle were already taken into account when estimating the rate constants and ψ (Elnashaie and Elshishini, 1994; Rase and Holmes, 1977). Table 4.3 presents the deviation for the outlet CO conversion and outlet temperature of the reactors. Information regarding the reactor size, catalyst size and gas composition, pressure and temperature at the reactor inlet is detailed in Elnashaie and Elshishini, 1994. From Table 4.3 it is possible to see the very good agreement between the results obtained by the model simulation and the industrial reactor data.

Table 4.3: Model prediction error for adiabatic operation.

Reactor	T_{outlet} error	CO conversion error
I	0.032 %	-2.97 %
II	-0.63 %	-3.51 %

From the simulation of the adiabatic reactors, the thermal and the mass Péclet numbers in the axial coordinate ($Pe_m = Re\,Sc$ and $Pe_t = Re\,Pr$, respectively) have an average value of approx. 10^5, which means that the terms in the material and energy balances involving D_z and λ_z may be safely neglected because they are 10^5 smaller than the convective terms. This is an indicator that, for reactors operating in industrial scale, the aforementioned variables are irrelevant. Therefore, this terms are not considered in this work anymore. By doing so, the approach used for solving the reactor model also changes. Instead of applying discretization in the spatial coordinates and performing integration in time, the integration can be directly applied in the axial coordinate since, in this coordinate, after removing the terms involving D_z and λ_z, the equations changed from a boundary value problem to an initial condition problem. Steady-state is also assumed because the dynamic behavior does not need to be known for sizing the reactor. After those assumptions, both mass and energy balances were reduced to Eq. 4.5.1 and Eq. 4.5.2, respectively.

$$v\frac{\partial C_i}{\partial z} = \frac{1}{r}\frac{\partial}{\partial r}\left(r\, D_{r,i}\frac{\partial C_i}{\partial r}\right) + \nu_i\left(1-\varepsilon\right)\eta r_{\text{int}} = 0 \tag{4.5.1}$$

$$C_{i,\text{inlet}} = C_i\left(z=0\right), \quad \forall\, r$$

$$-\left. D_{r,i}\frac{\partial C_i}{\partial r}\right|_{r=0} = 0, \quad \forall\, z$$

$$-\left. D_{r,i}\frac{\partial C_i}{\partial r}\right|_{r=d_\text{t}/2} = 0, \quad \forall\, z$$

$$C_\text{f} c_{p_\text{f}} v\frac{\partial T}{\partial z} = \frac{1}{r}\frac{\partial}{\partial r}\left(\lambda_r r\frac{\partial T}{\partial r}\right) - v\frac{T}{C_\text{f}}\left(\frac{\partial C_\text{f}}{\partial T}\right)_p\frac{\partial P}{\partial z} + \left(-\Delta_\text{r} h\right)\left(1-\varepsilon\right)\eta r_{\text{int}} \tag{4.5.2}$$

$$T_{\text{inlet}} = T\left(z=0\right), \quad \forall\, r$$

$$-\left. \lambda_r\frac{\partial T}{\partial r}\right|_{r=0} = 0, \quad \forall\, z$$

$$-\left. \lambda_r\frac{\partial T}{\partial r}\right|_{r=d_{\text{t}/2}} = \ddot{q}, \quad \forall\, z$$

4.6 Reactor Model Simulation

To prevent the occurrence of hot spots inside the reactor, the rate of reaction inside the model was set to zero if the temperature exceeded 523 K during the model simulation. In reality that means to place an inert layer right after the catalyst layer to prevent catalyst sintering and reactor runaways when the amount of heat being removed by the cooling fluid is not enough to counterbalance the heat released by the reaction. To test this implementation, the reactor model was simulated. Only the inlet temperature and d_t were changed. Other variables were set as follows: $d_\text{p} = 0.002$ m, and $v_{\text{inlet}} = 0.1$ m/s. The gas inlet pressure and composition, and the reactor length is that of Reactor I reported by Elnashaie and Elshishini (1994). The results are presented in Fig. 4.7, Fig. 4.8 and Fig. 4.9. By comparing Fig. 4.7 with Fig. 4.8, it is promptly noticed that for $T_{\text{inlet}} = 490$ K, there is the necessity of 3 inert layers (plateaus in the CO conversion profile) whilst for $T_{\text{inlet}} = 470$ K, no inert layer is requested and both achieve very similar conversions.

The inert layers correspond to 30.51 % of the total reactor volume in Fig. 4.8. This is advantageous from the economic point of view because less catalyst, which is more expensive, is required for achieving the same conversion. However, by decreasing d_t by half (Fig. 4.9), the heat exchange was enhanced and, as a result, the temperature did not raise as much as in Fig. 4.8 and the conversion obtained was approx. 5 % higher. This, at first, indicates that reducing the tube diameter seems to be the most feasible option. However, one should bear in mind that, reducing d_t by half while v_inlet is kept constant, meas that 2 tubes like Fig. 4.9 must be used to handle the total inlet molar flow rate. This implicates that, despite the better conversion, for the tubes represented by Fig. 4.9, the same amount of catalyst used in the tube represented by Fig. 4.7 is requested, which is 43.9 % more catalyst than that used for a tube represented by Fig. 4.8 due to the nonexistence of inert. Therefore, the sizing the reactor must be an optimization procedure so that the best option can be found.

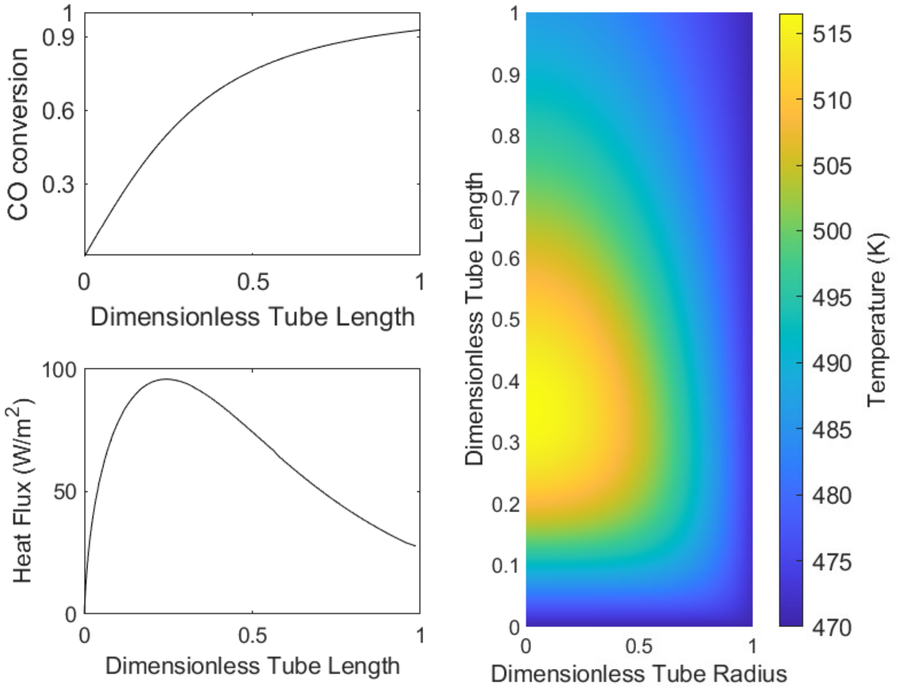

Figure 4.7: Reactor tube model simulation. $T_\mathrm{inlet} = 470$ K and $d_\mathrm{t} = 0.1$ m.

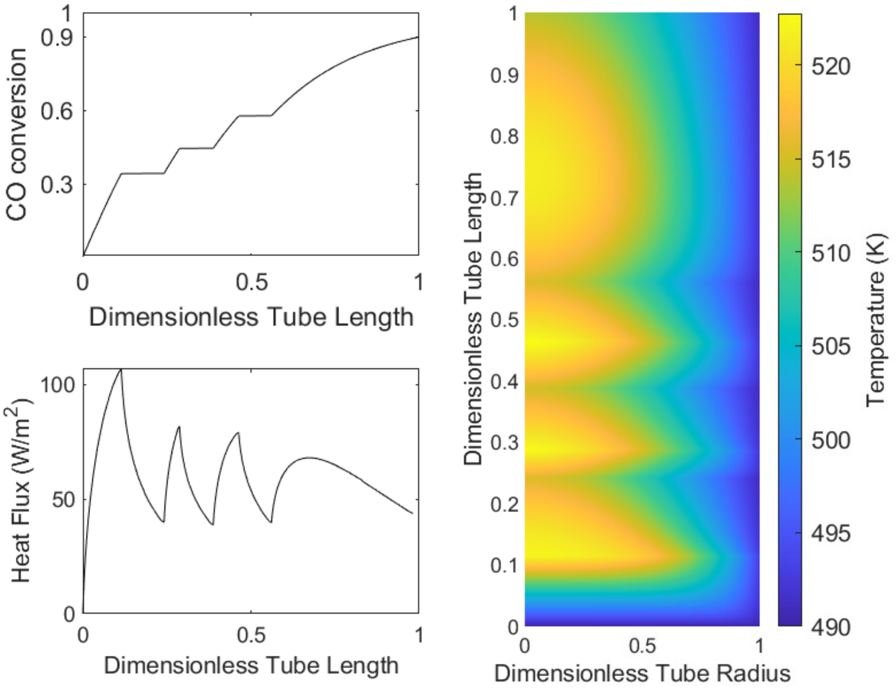

Figure 4.8: Reactor tube model simulation. $T_{\text{inlet}} = 490$ K and $d_{\text{t}} = 0.1$ m.

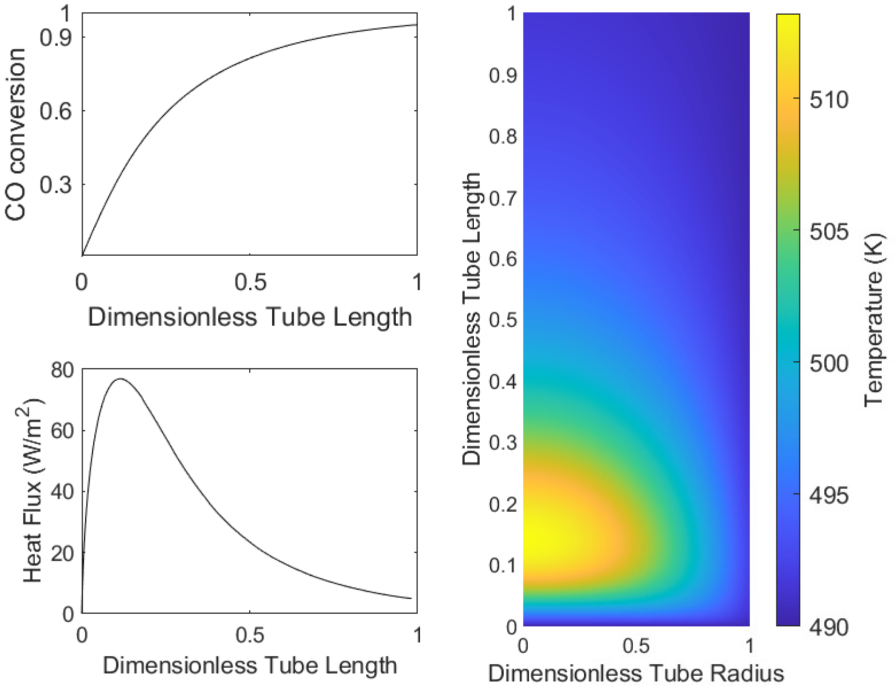

Figure 4.9: Reactor tube model simulation. $T_{\text{inlet}} = 490$ K and $d_{\text{t}} = 0.05$ m.

Finally, in all figures the hot spot occurs in the tube center. This is a common trend in fixed-bed reactors where exothermic reactions are conducted and it is reported in the literature (Froment et al., 2011; Vortmeyer et al., 1992).

4.7 Reactor Model Optimization

The reactor model is optimized according to a cost function, i.e., minimizing the summation of the real equipment cost (Eq. 3.7.4) and the operating cost.

4.7.1 Real Equipment Cost

To the best author's knowledge, there aren't literature available correlations for estimating the multitubular reactor's cost. Therefore, since the reactor is a heat exchanger, its bare module cost (C_{BM}) is approximated by using a correlation for a shell and tubes heat exchanger provided by Turton et al. (2012). The shell, where the cooling fluid (water) is evaporated, is constructed with carbon steel. The tubes, where the reaction takes place, are constructed with stainless steel. The reactor bare module cost is defined in Eq. 4.7.1.

$$C_{\mathrm{BM}_{\mathrm{reactor}}} = 10^{(4.8306-0.85009\,\log_{10}(A))+0.3187[\log_{10}(A)]^2)}\,(1.63+2.988F_P) \tag{4.7.1}$$

where F_P is the pressure factor, which is equal to 1 if $P < 5$ barg or calculated according to Eq. 4.7.2 if $5 \leq P < 140$ barg; and A is the heat exchanger area (m^2) (Eq. 4.7.3).

$$\log_{10}F_P = 0.03881 - 0.11272\,\log_{10}P + 0.08183\,(\log_{10}P)^2 \tag{4.7.2}$$

where P is the pressure in bar gauge.

$$A = \pi d_{\mathrm{t}}\,L\,N_{\mathrm{t}} \tag{4.7.3}$$

where L is the tube length (m), and N_{t} is the total number of tubes, which is defined according to Eq. 4.7.4.

$$N_{\mathrm{t}} = \frac{\dot{n}_{\mathrm{inlet}}}{v_{\mathrm{inlet}}C_{\mathrm{inlet}}A_{\mathrm{t}}} \tag{4.7.4}$$

The inlet pressure is assumed to be 1 barg. If it is increased, a cost associated with the compressors and compression power must be taken into account. The compressor bare module cost is calculated according to Eq. 4.7.5 (Turton et al., 2012).

$$C_{\mathrm{BM}_{\mathrm{compressor}}} = 2.8 \times 10^{(2.2897+1.3604\,\log_{10}(\dot{W}_{\mathrm{f}}))-0.1027[\log_{10}(\dot{W}_{\mathrm{f}})]^2)} \tag{4.7.5}$$

The fluid power ($\dot{W}_\mathrm{f}$ in kW) is calculated according to Eq. 4.7.6. The inlet temperature (T_1) is assumed to be 305 K and the outlet temperature (T_2) is calculated by assuming adiabatic reversible compression, i.e., $\Delta S = \Delta S^\mathrm{IG} + \Delta S^\mathrm{R} = 0$. The residual entropy variation (ΔS^R) is estimated by PRSV-EoS. In addition, if the compression ratio is greater than 3, another compression stage is added and an intermediate heat exchanger is placed between the stages. This is done to minimize compression power. The outlet temperature of the intermediate heat exchanger is set to be equal to the inlet temperature of the first compression stage. Cooling water is used as coolant. It is assumed to be available at 298 K and returning to the cooling tower at 313 K.

$$\dot{W}_\mathrm{f} = \dot{n}_\mathrm{inlet} \left(\int_{T_1}^{T_2} c_p^\mathrm{IG} \mathrm{d}T + h_{T_2,P_2}^\mathrm{R} - h_{T_1,P_1}^\mathrm{R} \right) \tag{4.7.6}$$

The compressor driver is assumed to be an electric motor, whose bare module cost is estimated by Eq. 4.7.7 (Turton et al., 2012).

$$C_{\mathrm{BM}_\mathrm{driver}} = 1.5 \times 10^{(1.956+1.7142\,\log_{10}(\dot{W}_\mathrm{s}))-0.2282[\log_{10}(\dot{W}_\mathrm{s})]^2)} \tag{4.7.7}$$

The shaft power ($\dot{W}_\mathrm{s}$) is based on the fluid power assuming an isentropic compressor efficiency of 78 % ($\dot{W}_\mathrm{s} = \dot{W}_\mathrm{f}/0.78$).

The bare module cost presented above are for the year of 2001. Therefore, an inflation correction factor must be used (Eq. 3.7.5). The CEPCI in September of 2001 was equal to 397 (Turton et al., 2012) and the 2018 average value was equal to 601.3 (Jenkins, 2019). Therefore, the total real equipment cost is:

$$C_\mathrm{R} = 1.51461(C_{\mathrm{BM}_\mathrm{reactor}} + C_{\mathrm{BM}_\mathrm{compressor}} + C_{\mathrm{BM}_\mathrm{driver}}) \tag{4.7.8}$$

4.7.2 Operating Cost ($\mathrm{C_O}$)

The operating cost is the sum of the electricity cost for the compressor driver, steam for adjusting the H_2O/CO molar ratio, cooling water for the heat exchangers between the compression stages, and the catalyst cost. The total electricity cost is found by multiplying the electricity cost US\$ 0.0671 $\mathrm{kW^{-1} \cdot h^{-1}}$ (EIA, 2019) by the electric power ($\dot{W}_\mathrm{e}$) consumed in 20 years, working 330 days a year and 24 hours a day (158,400 h in total). $\dot{W}_\mathrm{e}$ is calculated assuming an electric motor efficiency of 98 % ($\dot{W}_\mathrm{e} = \dot{W}_\mathrm{s}/0.98$).

Usually, the designer sets a maximum pressure drop allowable for the reactor. However, in this work, instead of setting a limit for the pressure drop, a penalty is introduced in the reactor cost function. The penalty is the cost of the total $\dot{W}_\mathrm{e}$ necessary to increase the pressure of the gas stream at the reactor outlet to its original value, i.e, the reactor inlet pressure.

The steam generation and the cooling water costs are calculated as stated in Appendix D.1. The boiler and cooling tower capital costs are not taken into account in this work. The shift reactor is not a standalone equipment. It is usually placed inside a complex chemical plant, in which these equipment are assumed to be installed.

The catalyst cost is 17.65 US$·kg^{-1} and it must be changed every 3 years (Banerjee et al., 2013). Therefore, it must be bought 7 times within 20 years, which result in a total cost of 123.55 US$·kg^{-1}. The inert cost is 12.5 % of the catalyst cost (Rase and Holmes, 1977).

The total operating cost (US$) is defined as:

$$C_{\mathrm{O}} = 10{,}628.64(\dot{W}_{\mathrm{e}} + \dot{W}_{\mathrm{e,penalty}}) + 123.55 m_{\mathrm{catalyst}} + 15.48 m_{\mathrm{inert}} + C_{\mathrm{steam}} \tag{4.7.9}$$

4.7.3 Objective Function

The optimization procedure is required to find the best reactor operational condition and size for a specified gas mass flow rate. The goal is to find the least expensive option. Therefore, the optimization is carried out by minimizing the summation of operational cost, C_{O}, and the real cost of the reactor and auxiliary equipment, C_{R}. The optimization problem is set as:

$$\begin{array}{ll}
\min & F = (C_{\mathrm{O}} + C_{\mathrm{R}}) + \left(1 \times 10^{11} y_{\mathrm{CO,\ dry\ gas,\ outlet}}\right) \\
\text{subjected to:} & \text{Material, energy and momentum balances} \\
 & 430\ \mathrm{K} \leq T_{\mathrm{inlet}} \leq 510\ \mathrm{K} \\
 & 2\ \mathrm{atm} \leq P_{\mathrm{inlet}} \leq 55\ \mathrm{atm} \\
 & 0.1\ \mathrm{m/s} \leq v_{\mathrm{inlet}} \leq 1.9\ \mathrm{m/s} \\
 & 2\ \mathrm{mm} \leq d_{\mathrm{p}} \leq 10\ \mathrm{mm} \\
 & 15\ \mathrm{mm} \leq d_{\mathrm{t}} \leq 100\ \mathrm{mm} \\
 & 435\ \mathrm{K} \leq T_{\mathrm{inert}} \leq 515\ \mathrm{K} \\
 & L \leq 10\ \mathrm{m} \\
 & 1 \leq \mathrm{H_2O/CO} \leq 8
\end{array}$$

The inlet temperature, velocity, H_2O/CO molar ratio and catalyst particle diameter ranges were defined for calculating the effectiveness factor in Subsection 4.3. The pressure range was defined according to the maximum pressure accepted for calculating the pressure correction factor (Eq. 4.2.4). The tube diameter and length intervals are defined according to the usual value encountered for multitubular reactors (Eigenberger and Ruppel, 2012).

Shift reactors are used to reduce the CO content in a gas stream. However, the CO molar fraction is a dependent variable. To find the outlet CO mole fraction ($y_{\text{CO, dry gas, outlet}}$), the reactor model must be solved, i.e., material, energy and momentum balances. Therefore, it is introduced in the objective function with at least one order of magnitude greater than the cost function. In this work, the desired $y_{\text{CO, dry gas, outlet}}$ is set to be 0.01 unless otherwise mentioned. The reactor model resolution is set to be performed from $L = 0$ m to $L = 10$ m. At each point in the axial coordinate, i.e, the length, $y_{\text{CO, dry gas}}$ is checked. If, for a certain length, $y_{\text{CO, dry gas}}$ has achieved 0.01, this length is set as the final and the objective function is evaluated. Otherwise, the integration proceeds until $L = 10$ m.

The reactor temperature may not exceed 523 K because the reaction rate parameters were estimate from data collected up to this temperature (Choi and Stenger, 2003). Therefore, if the temperature exceeds 523 K during the reactor model integration, an inert layer is placed. By simplicity, the inert is assumed to have the same thermal and physical properties than those of the catalyst. The inert layer ends when the gas temperature flowing through it (T_{inert}) achieves the value set by the optimizer within the range presented above. The reactor cooling fluid is always set to be 5 K below T_{inert} so that the heat exchange can occur.

Water cannot condense inside the reactor because it can damage the catalyst (Rase and Holmes, 1977). Therefore, the water saturation pressure ($P_{\text{H}_2\text{O}}$) must be taken into account in the optimization procedure. That is accomplished by inserting a penalty in optimization problem. If the water partial pressure is greater than its saturation pressure, that condition is deemed as unfeasible and the objective function promptly returns 10^{12} as value. Otherwise, the other required calculations to evaluate the objective function are carried out. The sequence of steps to evaluate the objective function is depicted in Fig. 4.10.

$P_{\text{H}_2\text{O}}$ is defined by the Antoine equation (Eq. 4.7.10), whose constants were estimated from the steam table (Smith et al., 2007), and 1 bar was subtracted as a safety measure, and are valid only in the range of 423 K - 523 K.

$$P_{\text{H}_2\text{O}} \leq \left[\exp\left(12.315 - \frac{4386.4}{T - 14.9}\right) - 1\right] \text{ bar} \tag{4.7.10}$$

To solve the optimization problem, the DIRECT (dividing rectangles) algorithm is used. It is a deterministic derivative-free algorithm, which does not suffer from the existence of local minima and it is able to converge to a global optimum (Jones et al., 1993). However, this algorithm performs more function evaluations when compared to those using the objective function gradient. The DIRECT was implemented in MATLAB® language by Finkel (2003).

The DIRECT algorithm was set to stop after 20,000 function evaluations, or if all sides of the best rectangle are smaller than 10^{-6}. The tuning parameter, which balances DIRECT between local and global search was set equal to 10^{-4}. According to Jones et al. (1993), this value was found to be adequate for finding the global optimum of different tested functions with an error smaller than 0.01%.

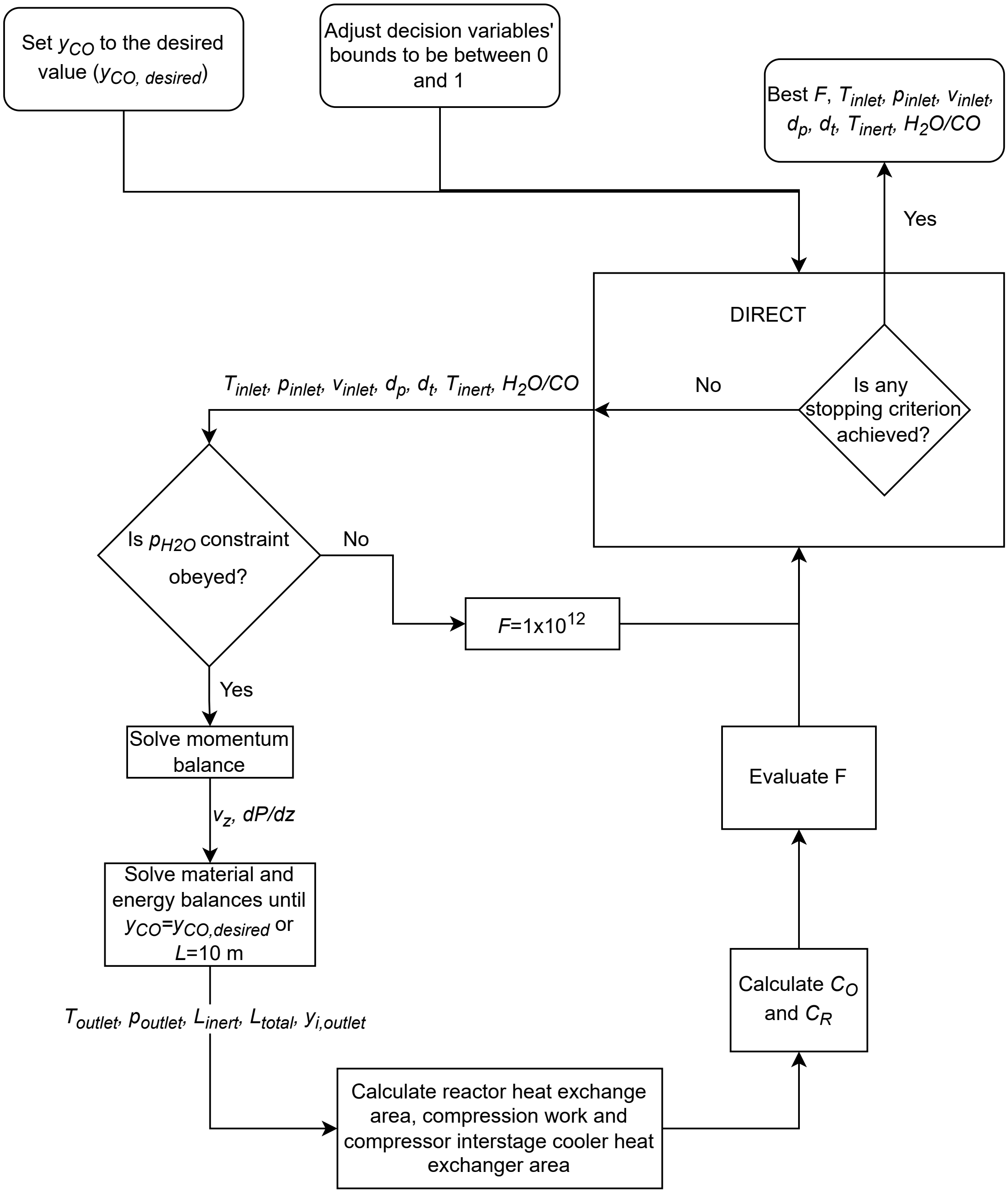

Figure 4.10: Flowchart of the procedure to evaluate the objective function.

4.7.4 Optimization Scenarios

Three different optimization scenarios are studied. The first one (OPT1) is performed for an average dry syngas composition (mol %) generated by a gasification process (Smirniotis and Reddy, 2015) (Table 4.4). The other two are carried out for a syngas produced in a natural gas steam reforming process.

The CO dry mole fraction at the reactor outlet of OPT2 is set to be 3%, which is equal to the original mole fraction reported by Elnashaie and Elshishini (1994) for the industrial HTSR. For OPT3, the CO dry mole fraction at the reactor outlet is set equal to 0.3%, which is equal to the original value obtained by Rase and Holmes (1977) when designing the HTSR followed by the LTSR. In addition, for OPT2 and OPT3, the H_2O/CO molar ratio and the reactor inlet pressure are kept constant and equal to the values reported by Elnashaie and Elshishini (1994) and Rase and Holmes (1977).

Table 4.4: Dry syngas at the reactor inlet.

	OPT1 (Smirniotis and Reddy, 2015)	OPT2 (Elnashaie and Elshishini, 1994)	OPT3 (Rase and Holmes, 1977)
$\dot{n}_{\text{inlet}}$ (kmol/s)	1	1.76	1.56
p_{inlet} (bar)	to be optimized	31.51	26.88
H_2O/CO	to be optimized	4.6	5
H_2	34 %	58.83 %	56.8 %
CO	47 %	11.67 %	13 %
CO_2	13 %	7.68 %	7.9 %
N_2	0 %	14.54 % *	21.8 %
CH_4	6 %	7.28 %	0.5 %

*Argon content included in nitrogen.

Each optimization scenario took roughly a month to be completed, and they all finished when DIRECT exceeded the limit of 20,000 objective function evaluations. The decisions' variable optimal values are shown in Table 4.5. As can be seen in Fig. 4.11, the objective function greatly decreased during the first 30 iterations, but hardly changed afterwards, which indicates that the predefined value of 10^{-6} for all sides of the best rectangle could be greater.

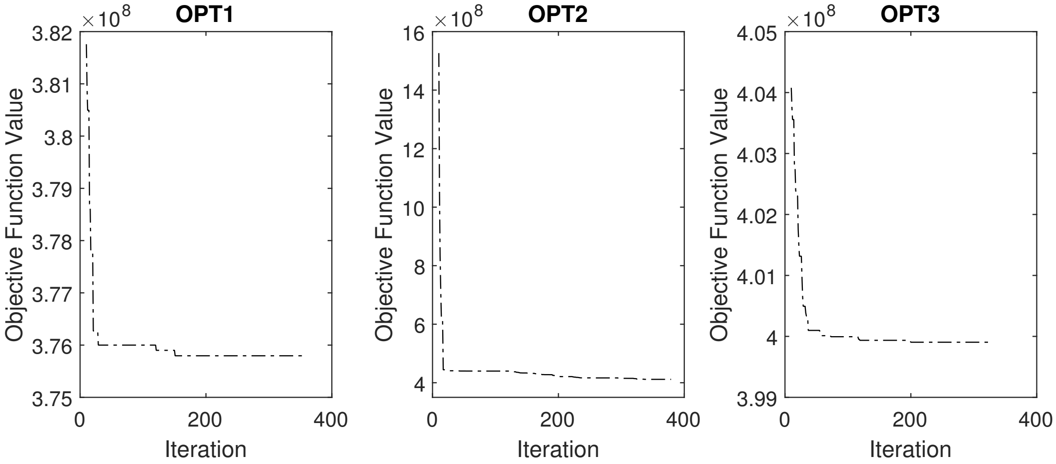

Figure 4.11: Objective function decrease according to DIRECT iterations.

Table 4.5: Optimization results.

Variables	OPT1	OPT2	OPT3
T_{inlet} (K)	459.38	465.72	459.68
p_{inlet} (bar)	21.23	31.51*	26.88*
v_{inlet} (m·s^{-1})	0.13	0.43	0.13
d_p (m)	0.002	0.002	0.002
d_t (m)	0.05	0.0998	0.0998
T_{inert} (K)	483.33	510.56	491.57
L (m)	9.92	9.17	9.03
H_2O/CO	2.05	4.6*	5*
F $\times 10^{-8}$ (US$)	3.758	4.115	3.999
Optimization time (days)	31	33	33
F evaluation	20,072	20,069	20,065

*Specified value.

For all three scenarios, the inlet gas temperature was lower than the cooling fluid temperature so that at the beginning of the bed, the gas mixture is heated up by both the cooling fluid and the reaction itself. At some point within the bed, the gas mixture becomes hotter than the cooling fluid and the heat exchange changes the direction (Figs. 4.12, 4.13, and 4.14). Since the reaction is exothermic, it is preferred to start it at a lower temperature so that the desired CO conversion can be achieved within the maximum tube length (10 m).

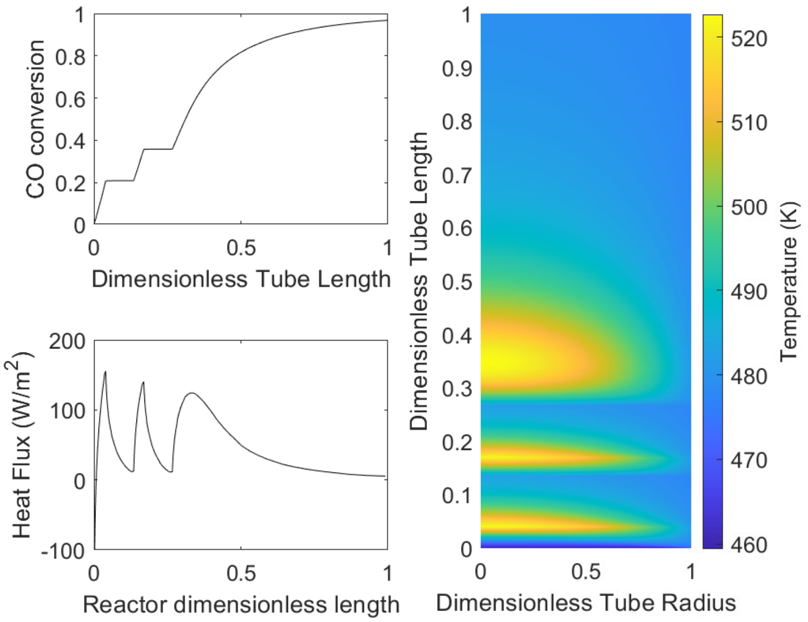

Figure 4.12: OPT1 temperature, CO conversion and heat flux reactor tube profiles.

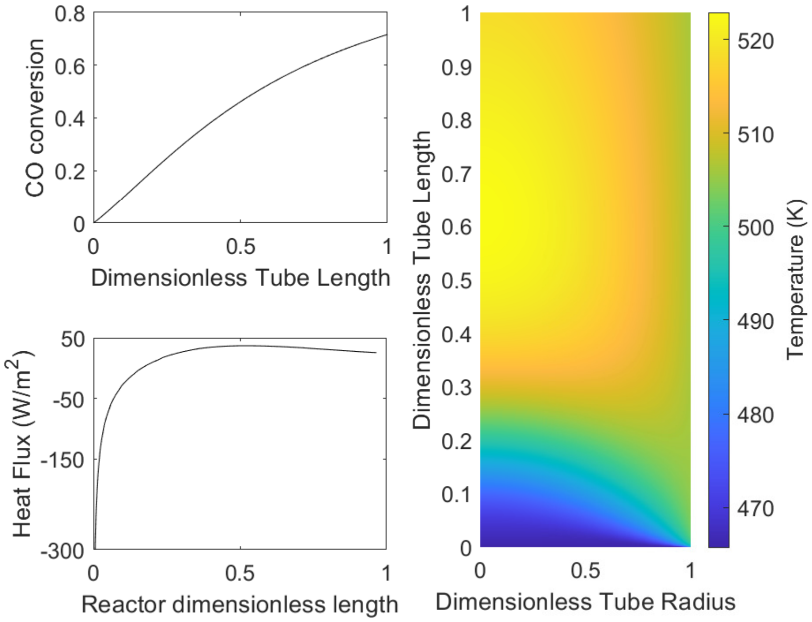

Figure 4.13: OPT2 temperature, CO conversion and heat flux reactor tube profiles.

In addition, no inert layer exists for the optimal scenarios of OPT2 (Fig. 4.13) and OPT3

(Fig. 4.14). In those cases, the benefit of the gas cooling inside the inert layer does not pay off the reactor length increase. Nevertheless, for OPT1, this changes (Fig. 4.12). The CO content for this scenario is considerably higher, and so is the heat that is released during its conversion. Therefore, 2 inert layers (1.748 m of the total tube length) are required. The importance of the gas cooling for OPT1 is also apparent when comparing the tube diameter found to be the optimum for this scenario with the tube diameter of OPT2 and OPT3.

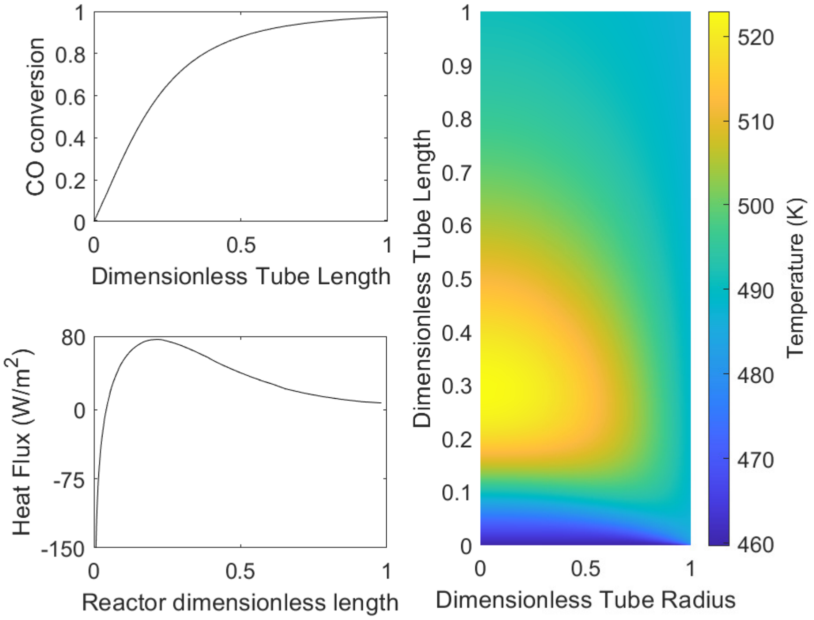

Figure 4.14: OPT3 temperature, CO conversion and heat flux reactor tube profiles.

The inlet pressure for OPT1 is lower than that found in natural gas steam reforming plants (OPT2 and OPT3). This happens as a consequence of the pressure factor (Eq. 4.2.4) greatly increasing up to 20 atm, and then remaining practically constant (Adams II and Barton, 2009). Therefore, there was no need to increase the reactor pressure. In natural gas steam reforming plants, the pressure is higher due to the operational pressure of equipment upstream. The gas velocity was found to be the same for OPT1 and OPT3, but for OPT2 is was considerably higher. There is a very close relation between residence time and overall conversion. For OPT3, the final CO content was 10 times smaller than that of OPT2. Therefore, a slower flow velocity was necessary. For OPT1, the final CO concentration was only 3 times smaller, but the initial content was much higher. In fact, for OPT1, the initial CO content was so high that the best H_2O/CO was only 2, which is half of the usual value. Regarding this matter, water is added in excess to force the CO conversion by shifting the reaction equilibrium (Rase and Holmes, 1977).

The particle diameter for all scenarios was found to be at its lower bound. The bigger the particle diameter, the lower the effectiveness factor, but the pressure drop also decreases. Since for all scenarios the costs related to the pressure drop caused by the catalytic bed (approximately 4% of the total electricity cost for all cases) can be considered irrelevant when compared to other costs (See Table 4.6), the optimal d_p was found at its lower bound. The same result was reported by Francesconi et al. (2007), who found a negligible pressure drop by optimizing an adiabatic LTSR.

By comparing the catalyst mass obtained for OPT2 and OPT3 with the respective adiabatic reactors reported by Elnashaie and Elshishini (1994) and Rase and Holmes (1977), the reactor with integrated heat exchange always requires more catalyst than the adiabatic ones. The lower the final CO concentration, the greater this difference. For example, comparing the catalyst mass of OPT2 with the catalyst mass reported by Elnashaie and Elshishini (1994) (for 3% CO at the outlet), the difference is of 27.5%. For OPT3 (0.3% CO at the outlet) with the catalyst mass reported by Rase and Holmes (1977), the difference is of 258%. The larger amount of catalyst obtained in this work is due to the lower temperature of operation.

Pasel et al. (2005) obtained better results operating the reactor in isothermal mode. The catalyst, however, was composed of a noble metal that is likely more active than the Cu-based catalyst considered in this work. To prove this point, taken the same conditions obtained in OPT2, but increasing the catalytic activity by 10%, the required catalyst mass would drop from +27.5% to -12% compared to the value reported by Elnashaie and Elshishini (1994). Moreover, the methanol synthesis is industrially conducted in a multi-tubular reactor with integrated heat exchange also with a Cu-based catalyst at a similar temperature (Leonzio, 2020). The difference is that the methanol formation reaction is twice more exothermic than WGSR. Therefore, the use of multi-tubular reactors with integrated heat exchange for exothermic reactions depends both on the catalytic activity and on the amount of heat being released by the reaction.

Giunta et al. (2006) reported a better conversion for the isothermal operation when compared to the adiabatic operation of a LTSR. Its H_2O/CO molar ratio was approximately 6.7, which is considerably high, and would increase the operational cost, since steam generation cost is high considering the 20 years horizon (Table 4.6).

Marín et al. (2012) has shown the advantage of using a membrane in an adiabatic reactor at a high temperature, *i.e.*, 670 K. Therefore, it is suggested to also use a membrane to continuously remove H_2 from the multi-tubular reactor. By removing H_2 from the system, the reaction rate over the Cu-based catalyst would remain elevated, and with a lower operational temperature, the steam generation cost can be diminished.

Table 4.6: Reactor and costs summary for a 20-year lifespan.

Variables	OPT1	OPT2	OPT3
Compression			
Stages	3	3	3
Compressor cost $\times 10^{-6}$ (US$)	6.28	10.06	8.99
Driver cost $\times 10^{-5}$ (US$)	9.6	10.06	10.05
Heat exchanger cost $\times 10^{-6}$ (US$)	2.52	5.17	4.28
Reactor			
Pressure drop (bar)	0.15	1.75	0.17
Number of tubes	13,286	970	3,444
Catalyst mass (ton)	303.8	100.4	350.8
Inert mass (ton)	61.3	0	0
Heat exchange area (m^2)	20,584	2,790	9,752
Reactor cost $\times 10^{-6}$ (US$)	88	3.54	23.46
Operational costs			
Electricity $\times 10^{-7}$ (US$)	9.73	20.2	16.87
Catalyst $\times 10^{-7}$ (US$)	3.75	1.24	4.33
Steam $\times 10^{-7}$ (US$)	13.16	12.93	13.79
Cooling water $\times 10^{-6}$ (US$)	10.70	12.99	12.25

4.7.5 PRSV-EoS *versus* Ideal Gas Model

As mentioned earlier in the literature review, most authors simplify their models by assuming ideal gas behavior regardless the considerably above atmospheric operational pressure. To evaluate if there is a significant difference in the model's prediction capability by making such simplification, the three optimized scenarios were simulated considering either non-ideal gas behavior by the PRSV-EoS (standard in this work) or ideal gas behavior. The results are shown in Table 4.7.

Table 4.7: Optimal scenarios simulations. Comparison between PRSV-EoS and ideal gas model.

Variables	PRSV-EoS	Ideal Gas	Difference
	OPT1		
CO conversion (%)	95.9	96.5	-0.6 %
Highest bed temperature (K)	522.29	523.39	-0.02 %
Computation time (s)	118	27	440 %
	OPT2		
CO conversion (%)	71.8	71	1.2 %
Highest bed temperature (K)	522.7	514.4	1.6 %
Computation time (s)	48.7	12.5	390 %
	OPT3		
CO conversion (%)	97	97	0 %
Highest bed temperature (K)	522.22	523.47	-0.02 %
Computation time (s)	50	21.8	228 %

It is clear that considering ideal gas behavior does not affect the model's capability of predicting neither the CO conversion nor the temperature inside the reactor. Indeed, for OPT2 it is observed that considering ideal gas behavior affects both the temperature and the CO conversion than for the other scenarios. However, the difference is completely acceptable taking into account that the time spent to solve the model when ideal gas behavior is considered is much less e. i., almost 4 times less. Therefore, up to approx. 30 bar at least the ideal gas model can be safely considered for simulations of the water-gas shift reactor. Nevertheless, if higher operational pressures are required, not only for the WGSR, but for any other gaseous reactions, the model with PRSV-EoS developed in this work has also proven to be useful and shall serve as a basis.

4.7.6 Critical Heat Flux and Heat Transfer Limitation

So far, all simulations were carried out considering an overall heat transfer coefficient (U) of 30 W·m^{-2}·K^{-1}. When the fluid is being heated up and starts boiling, bubbles start to be formed at the tube surface and to break loose. This causes an additional agitation, which improves the heat transfer mechanism. Nevertheless, if the temperature difference between the boiling fluid and the hot gases keep increasing, the rate of vaporization at the tube surface may achieve a critical level, creating dry patches, which drastically decreases the heat exchange rate and may cause a reactor runway if the temperature is not self-controlling, e.g., by thermodynamic equilibrium. In the critical level, the heat flux is referred to as critical heat flux and design condition should be far from this value (Smith, 2005).

Since the cooling fluid is assumed to be changing phase, it is mandatory to evaluate if the heat flux achieved in the design by assuming U is far from the critical heat flux. The critical heat flux for the three optimized scenarios were calculated by Mostinski's equation (Eq. 4.7.11) (Smith, 2005) and they are compared with the maximum heat flux achieved inside the reactor for each optimized scenario in Table 4.8. As can be seen, for all three optimized scenarios, the maximum heat flux is at least 38% below the critical heat flux, which indicates that the assumed U value is acceptable for a valid design and even with an elevated bed temperature increase, the critical heat flux would not be achieved.

$$\ddot{q}_c = 3.67 \times 10^4 P_c \left(\frac{P}{P_c}\right)^{0.35} \left[1 - \left(\frac{P}{P_c}\right)\right]^{0.9} \tag{4.7.11}$$

where P_c is the water critical pressure in bar and P is water boiling pressure in bar for each optimized scenario.

Table 4.8: Optimal scenarios simulations. Heat flux comparison.

	Maximum heat flux (W·m^{-2})	Critical heat flux (W·m^{-2})
OPT1	2.00×10^6	3.25×10^6
OPT2	3.58×10^4	3.56×10^6
OPT3	2.63×10^5	3.45×10^6

Finally, U value was changed from 30 W·m^{-2}·K^{-1} to 5 W·m^{-2}·K^{-1} and the simulations for the three optimized scenarios were carried out to evaluate what would be the maximum temperature inside the bed in case of very poor heat exchange. The results are shown in Table 4.9. Despite the fact that the bed temperature increases, the changes cannot be considered enough to harm the reactor's structure. The catalyst may suffer sintering in case OPT1 due to 30 K temperature increase. However, one should bear in mind that 5 W·m^{-2}·K^{-1} is a very small value that would be unlikely encountered. As a matter of fact, the usual lowest value reported by Roetzel and Spang (2010) for such system is 15 W·m^{-2}·K^{-1}.

Table 4.9: Optimal scenarios simulations. Result comparison for different overall heat transfer coefficients.

U	30 W·m^{-2}·K^{-1}	5 W·m^{-2}·K^{-1}	Difference
OPT1			
Highest bed temperature (K)	522.29	551.58	-5.3 %
OPT2			
Highest bed temperature (K)	522.7	525.92	-0.6 %
OPT3			
Highest bed temperature (K)	522.22	527.97	-1.00 %

Chapter 5

Conclusions

The possibility of replacing the usual HTSR-LTSR by one single reactor with integrated heat exchange was evaluated in this part of the work. Firstly, it was identified that the best approach to perform such evaluation was to model the reactor, considering the three transport phenomena fundamental equations, i.e., mass, energy and momentum balances, instead of only relaying on a thermodynamic analysis.

To account for mass and heat transport resistances from the bulk gas phase to the catalyst particle (surface and its interior) and vice-versa, an effectiveness factor (η) was estimated. The estimation was carried out using data from more than 30,000 catalyst particle simulations for different operational conditions. From those simulations, it was possible to identify that inside the catalyst particle mass diffusion limitations is very pronounced and the heat transport resistance has a minor effect whereas from the catalyst surface to the bulk gas the resistances change roles. Although it was not possible to find one single surrogate model able to predict the effectiveness factor over the entire catalyst particle diameter range under consideration, the five proposed models can be considered appropriate to perform such task based on the respective obtained correlation coefficients. For particle diameters lying in between the ones used to perform the estimation, linear interpolation seems appropriate to find η. However, data extrapolation is not recommended.

A 2D pseudo-homogeneous model was developed, considering an engineering equation of state for the gas thermodynamic behavior. The developed model was validated against laboratory and industrial data. Based on the results of the simulations performed to validate the model, both mass and thermal Peclét numbers in the axial coordinate were very high ($>10^5$), indicating that heat and mass convection are dominating, thus, mass diffusion and thermal conductivity could be safely neglected for the axial coordinate.

After optimizing the reactor for three different scenarios, namely, OPT1, OPT2, and OPT3, it was noticed that operating the reactor at a lower temperature with integrated heat exchange requires more catalyst than the usual HTSR-LTSR configuration. It is well-known that, according to the Arrhenius' equation, the temperature affects the reaction kinetics greatly. Therefore, a more active catalyst with a competitive price is necessary so that the requested mass can be reduced, and the benefit of generating steam at a lower temperature can be visible. Another alternative is to keep the current catalyst, but use a membrane reactor. With a continuous H_2 removal from the bed, the reaction rate would remain high even at a low temperature and the costs with steam generation would be minimized.

It could also be noticed that there is a trade-off between the use of either a adiabatic reactor with intermediate cooling or a multi-tubular reactor with integrated heat exchange. The reactor choice depends both on the catalytic activity and on the amount of heat being released by the main reaction. For the WGSR ($\Delta_{\mathrm{r}} h^0_{(\text{at } 298.15\,\mathrm{K} \text{ and } 1\,\mathrm{bar})} = -41.16$ kJ $\cdot\mathrm{mol}^{-1}$) the best option is the HSTR-LTSR configuration, but for the methanol synthesis ($\Delta_{\mathrm{r}} h^0_{(\text{at } 298.15\,\mathrm{K} \text{ and } 1\,\mathrm{bar})} = -90.7$ kJ $\cdot\mathrm{mol}^{-1}$), for example, the multi-tubular reactor with integrated heat exchange is desirable. Both reactions are enhanced by a very similar catalyst in the same temperature range.

After optimizing the reactors it was also observed that the lower the outlet CO mole fraction, the greater the catalyst mass difference between the reactor studied in this work and the HTSR-LTSR, and the higher the initial CO load, the higher the reactor size, which, in turn, makes the process of using only one single reactor operating at a lower temperature with a Cu-based catalyst unrealistic.

A comparison with the results obtained from the simulations of the optimized cases using PRSV-EoS and ideal gas was made. For all three cases, the assumption of ideal gas behavior has shown to be completely acceptable due to very similar results obtained. The maximum deviation was of only 1.6% for the highest bed temperature in case OPT2. In addition, model simulation time considerably decreases when using the ideal gas model. OPT3 simulation is solved twice faster and OPT1 4 times faster when ideal gas is assumed. Despite the similar results obtained with ideal gas model, the model developed in this work with PRSV-EoS has also shown to be useful and may be used as basis for future works in which ideal gas behavior is not valid assumption.

Finally, for all three optimized designs the critical heat flux was calculated and compared to the maximum heat flux achieved inside the reactor's bed. The results have shown that the assumed overall heat transfer coefficient is acceptable and the design scenarios are valid because maximum heat flux achieved is well below the critical one. Even assuming a very poor heat transfer between the hot gases and the boiling water by decreasing the overall heat transfer coefficient 6 times the original one, additional simulations shown only a 30 K increase in the highest bed temperature.

References

Adams II, T. A. and P. I. Barton (2009). “A dynamic two-dimensional heterogeneous model for water gas shift reactors”. In: *International Journal of Hydrogen Energy* 34.21. DOI: 10.1016/j.ijhydene.2009.08.045, pp. 8877–8891.

Amadeo, N. E. and M. A. Laborde (1995). “Hydrogen production from the low-temperature water-gas shift reaction: kinetics and simulation of the industrial reactor”. In: *International journal of hydrogen energy* 20.12. DOI: 10.1016/0360-3199(94)00130-R, pp. 949–956.

Appl, M. (1999). *Ammonia: principles and industrial practice.* Weinheim, Germany: Wiley-VCH.

Banerjee, S. et al. (2013). “Technoeconomic analysis of biofuel production and biorefinery operation utilizing geothermal energy”. In: *Energy & Fuels* 27.3. DOI: 10.1021/ef301898n, pp. 1381–1390.

Bartholomew, Calvin H. and Robert J. Farrauto (2006). *Fundamentals of Industrial Catalytic Processes.* second ed. John Wiley & Sons, New York.

Bird, R. B., W. E. Stewart, and E. N. Lightfoot (2002). *Transport Phenomena.* Second Edition. John Wiley & Sons, Inc.

Çengel, Yunus A.. and Michael A. Boles (2007). *Thermodynamics: An Engineering Approach.* McGraw-Hill Higher Education.

Chanson, Hubert (1996). *Air Bubble Entrainment in Free-Surface Turbulent Shear Flows.* Chapter 12 - Air Entrainment in Partially-Filled Conduits. Academic Press.

Chen, Wei-Hsin et al. (2008). “Modeling and simulation of hydrogen generation from high-temperature and low-temperature water gas shift reactions”. In: *International Journal of Hydrogen Energy* 33.22. DOI: 10.1016/j.ijhydene.2008.08.039, pp. 6644–6656.

Choi, Yongtaek and Harvey G Stenger (2003). “Water gas shift reaction kinetics and reactor modeling for fuel cell grade hydrogen”. In: *Journal of Power Sources* 124.2. DOI: 10.1016/S0378-7753(03)00614-1, pp. 432–439.

Ding, OL and SH Chan (2008). “Water–gas shift reaction–A 2-D modeling approach”. In: *international journal of hydrogen energy* 33.16. DOI: 10.1016/j.ijhydene.2008.05.087, pp. 4325–4336.

Dong, Ying (2018). "Modeling Chemistry and Flow in Catalytic Fixed-Bed Reactors with Detailed Geometry". PhD thesis. Technischen Universitat Hamburg. Hamburg, Germany.

Eggeman, T (2010). *Ammonia. Kirk-Othmer Encyclopedia of Chemical Technology.* 1–33.

EIA (2019). *Average Price of Electricity to Ultimate Customers by End-Use Sector.* `https://www.eia.gov/electricity/monthly/epm_table_grapher.php?t=epmt_5_6_a`. (accessed 26 August 2019).

Eigenberger, Gerhart and Wilhelm Ruppel (2012). "Catalytic Fixed-Bed Reactors". In: *Ullmann's Encyclopedia of Industrial Chemistry.*

Elnashaie, S. S. E. H. and Elshishini (1994). *Modelling, simulation and optimization of industrial fixed bed catalytic reactors.* Ed. by R. Hughes. Vol. 7. Topics in Chemical Engineering. Gordon and Breach Science.

Finkel, Daniel E. (2003). "DIRECT optimization algorithm user guide". In: *Center for Research in Scientific Computation, North Carolina State University*, pp. 1–14.

Francesconi, Javier A, Miguel C Mussati, and Pio A Aguirre (2007). "Analysis of design variables for water-gas-shift reactors by model-based optimization". In: *Journal of Power Sources* 173.1. DOI: 10.1021/ie101137b, pp. 467–477.

Froment, Gilbert F., Kenneth B. Bischoff, and Juray De Wilde (2011). *Chemical Reactor Analysis and Design.* third ed. John Wiley & Sons Inc.

Giunta, P., N. Amadeo, and M. Laborde (2006). "Simulation of a low temperature water gas shift reaction using the heterogeneous model/application to a PEM fuel cell". In: *Journal of Power Sources* 156. DOI: 10.1016/j.jpowsour.2005.04.036, pp. 489–496.

Hla, S. S. et al. (2011). "Investigation into the performance of a Co–Mo based sour shift catalyst using simulated coal-derived syngases". In: *International Journal of Hydrogen Energy* 36.11. DOI: 10.1016/j.ijhydene.2011.02.075, pp. 6638–6645.

Hunt, M. L. and C. L. Tien (1988). "Non-Darcian convection in cylindrical packed beds". In: *Journal of Heat Transfer* 110.2. DOI: 10.1115/1.3250495, pp. 378–384.

Iordanidis, A. A. (2002). "Mathematical Modeling of Catalytic Fixed Bed Reactors". PhD thesis. University of Twente. URL: `https://ris.utwente.nl/ws/portalfiles/portal/6073612/t0000040.pdf`.

IPPC (2007). *Reference Document on Best Available Techniques for the Manufacture of Large Volume Inorganic Chemicals – Ammonia, Acids and Fertilisers.* Technical Report. `http://eippcb.jrc.ec.europa.eu/reference/BREF/lvic_aaf.pdf`. (accessed 24 September 2018). Integrated Pollution Prevention and Control. European Commission.

Jenkins, Scott (2019). *Chemical Engineering Plant Cost Index: 2018 Annual value.* `https://www.chemengonline.com/2019-cepci-updates-january-prelim-and-december-2018-final/`. (accessed 26 August 2019).

Jones, Donald R, Cary D Perttunen, and Bruce E Stuckman (1993). "Lipschitzian optimization without the Lipschitz constant". In: *Journal of Optimization Theory and Applications* 79.1. DOI: 10.1007/BF00941892, pp. 157–181.

Keiski, Riitta L, Tapio Salmi, and Veikko J Pohjola (1992). "Development and verification of a simulation model for a non-isothermal water-gas shift reactor". In: *The Chemical Engineering Journal* 48.1. DOI: 10.1016/0300-9467(92)85003-R, pp. 17–29.

Leonzio, Grazia (2020). "Mathematical modeling of a methanol reactor by using different kinetic models". In: *J. Ind. Eng. Chem.* 85. DOI: 10.1016/j.jiec.2020.01.033, pp. 120–140.

Marín, Pablo, Fernando V Díez, and Salvador Ordóñez (2012). "Fixed bed membrane reactors for WGSR-based hydrogen production: Optimisation of modelling approaches and reactor performance". In: *International journal of hydrogen energy* 37.6. DOI: 10.1016/j.ijhydene.2011.12.027, pp. 4997–5010.

Markatos, N. C. et al. (2005). "Membrane reactor modelling: A comparative study to evaluate the role of combined mass and heat dispersion in large-scale adiabatic membrane modules". In: *Chemical Engineering Research and Design* 83.10. DOI: 10.1205/cherd.04299, pp. 1171–1178.

Martinez, O. M., S. I. Pereira Duarte, and N. O. Lemcoff (1985). "Modeling of fixed bed catalytic reactors". In: *Computers & chemical engineering* 9.5. DOI: 10.1016/0098-1354(85)80028-4, pp. 535–545.

Mendes, Diogo et al. (2010). "Determination of the low-temperature water- gas shift reaction kinetics using a Cu-based catalyst". In: *Industrial & Engineering Chemistry Research* 49.22. DOI: 10.1021/ie101137b, pp. 11269–11279.

Moe, J. M. (1962). "Design of water gas shift reactors". In: *Chemical Engineering Progress* 58, pp. 33–36.

Nauman, E Bruce (2008). *Chemical reactor design, optimization, and scaleup.* John Wiley & Sons.

Papageorgiou, JN and GF Froment (1995). "Simulation models accounting for radial voidage profiles in fixed-bed reactors". In: *Chemical Engineering Science* 50.19. DOI: 10.1016/0009-2509(95)00 pp. 3043–3056.

Pasel, J et al. (2005). "Test of a water–gas-shift reactor on a 3 kWe-scale—design points for high-and low-temperature shift reaction". In: *Journal of power sources* 152. DOI: 10.1016/j.jpowsour.2004.12.051, pp. 189–195.

Plaza, A et al. (2016). "Apparent kinetics of the catalyzed water–gas shift reaction in synthetic wood gas". In: *Chemical Engineering Journal* 301. DOI: 10.1016/j.cej.2016.04.152, pp. 222–228.

Rase, Howard F (1990). *Fixed-bed reactor design and diagnostics: gas-phase reactions.* Butterworth-Heinemann.

Rase, Howard F. and James R. Holmes (1977). *Chemical reactor design for process plants.* Vol. 2. John Wiley & Sons, New York.

Roetzel, Wilfried and Bernhard Spang (2010). *VDI Heat Atlas.* Ed. by Peter Stephan. 2nd Edition. Part C3. Springer-Verlag Berlin Heidelberg. ISBN: 978-3-540-77877-6.

Saeidi, Samrand et al. (2017). "Hydrogen production: Perspectives, separation with special emphasis on kinetics of WGS reaction: A state-of-the-art review". In: *Journal of Industrial and Engineering Chemistry* 49. DOI: 10.1016/j.jiec.2016.12.003, pp. 1–25.

Seider, Warren D., J.D. Seader, and Daniel R. Lewin (2003). *Product and Process Design Principles.* second ed. John Wiley & Sons, New York.

Smirniotis, Panagiotis G. and Gunugunur K. Reddy (2015). *Water Gas Shift Reaction: Research Developments and Applications.* Elsevier.

Smith, Byron, Muruganandam Loganathan, and Murthy Shekhar Shantha (2010). "A review of the water gas shift reaction kinetics". In: *International Journal of Chemical Reactor Engineering* 8.1.

Smith, Joseph M., Hendrick C. Van Ness, and Michael M. Abbott (2007). *Introdução à termodinâmica da engenharia química.* 7th edition. Rio de Janeiro, Brasil: LTC.

Smith, Joseph Mauk (1970). *Chemical engineering kinetics.* 2nd Edition. McGraw-Hill.

Smith, Robin (2005). *Chemical process: design and integration.* John Wiley & Sons.

Souza, Renata N C de (2013). *Estudo e Simulação do Processo de Gaseificação.* Trabalaho de conclusão de curso. Escola de Química, Universidade Federal do Rio de Janeiro (EQ/UFRJ).

Stryjek, R and JH Vera (1986). "PRSV: An improved Peng—Robinson equation of state for pure compounds and mixtures". In: *The canadian journal of chemical engineering* 64.2, pp. 323–333.

Tiemersma, T. P. et al. (2006). "Modelling of packed bed membrane reactors for autothermal production of ultrapure hydrogen". In: *Chemical Engineering Science* 61.5. DOI: 10.1016/j.ces.2005.10.004, pp. 1602–1616.

Towler, Gavin and Raymond K Sinnott (2012). *Chemical engineering design: principles, practice and economics of plant and process design.* second ed. Elsevier, New York.

Tsotsas, Evangelos (2010). *VDI Heat Atlas.* Ed. by Peter Stephan. 2nd Edition. Part M7. Springer-Verlag Berlin Heidelberg. ISBN: 978-3-540-77877-6.

Turton, Richard et al. (2012). *Analysis, synthesis and design of chemical processes.* fourth ed. Pearson Education, New York.

Ulrich, G. D. and P. T. Vasudevan (2006). “How to estimate utility costs”. In: *Chemical Engineering* 113.4, p. 66.

Vortmeyer, D., P. Wagner, and E. Haidegger (1992). “The interaction between temperature and flow in wall-cooled catalytic fixed-bed reactors”. In: *Chemical Engineering Science* 47.5. DOI: 10.1016/0009-2509(92)80256-C, pp. 1325–1328.

Part II

The Power Cycle

In Part II the heat released by the exothermic WRSR is used as heat source for both the conventional (ORC) and recuperative (RORC) organic Rankine cycles. The heat that must be removed from each optimized reactor design from Part I, namely, OPT1, OPT2 and OPT3, is the power cycle boiler heat load. The idea is to study the possibility of using the saturated steam generated in the reactor's shell to generate additional electricity to the chemical plant. To carry out the study, the power cycles are modeled and simulated for different working fluids and the best scenario is chosen after a thermoeconomic assessment.

Chapter 6

Main Objective

Select the most appropriate working fluid and power cycle arrangement based on a thermal-economic assessment for recovering the heat released by the Water-Gas Shift Reaction (WGSR).

6.1 Specific Objectives

- Define a set of suitable working fluids for the Organic Rankine Cycle (ORC) to transform the heat wasted by the multitubular catalytic reactor into power;
- Assess the power cycle's performance by calculating both First and Second Law of Thermodynamics efficiencies;
- Estimate heat exchange area for each heat exchanger present in the power cycle based on literature-available correlations, which take into account the fluids' thermophysical properties;
- Estimate the power cycle's Net Present Value (NPV) for the fluids with the best thermodynamic performance and select the most appropriate one.

Chapter 7

Literature Review and Fundamentals

The development of power cycles has its roots on the constant necessity for life's quality improvement. Some are used to produce electricity to illuminate our homes and power our household appliances. Others are used to transport people and goods. Independently of the type, all of them are used to convert a form of energy into a more useful one. How efficient this conversion is performed can be assessed by carrying out either a thermodynamic or economic analysis or a combination of both. This chapter begins with a description of the thermoeconomic assessment of power cycles. Subsequently, the power cycles of interest are discussed along with preceding studies about them found in the literature.

7.1 Power Cycles Performance Indicators

The First Law efficiency, also known as thermal efficiency, is related with the energy conservation. It is a measure of how efficiently the power cycle converts the energy received into the desirable energy form. Since the power cycle is not allowed to produce more energy that it has received, the First Law efficiency may never be greater than one. This can be mathematically expressed as follows (Moran et al., 2011):

$$\eta_{\mathrm{I}} = \frac{\dot{W}_{\mathrm{net}}}{\dot{Q}} < 1 \tag{7.1.1}$$

where η_{I} is the First Law efficiency, $\dot{Q}$ (kW) is the total amount of energy received from the primary source, usually as heat rate, and $\dot{W}_{\mathrm{net}}$ (kW) is the cycle's net power produced in the desirable form, i.e., power.

η_{I} alone, although a good measure of the cycle's performance, is neither able to show how much of the maximum energy available is transformed into power nor how much of the energetic potential is being destructed throughout the process. That can be indicated by the

Second Law efficiency. As an aside, by considering one of the Second Law of thermodynamics statement, it can be affirmed that η_{I} may also never be equal 1 (Moran et al., 2011).

To determine how much of power generation potential is being destructed or lost, the initial maximum potential must be firstly known. To accomplish such task, the exergy ($\dot{E}x$) of the primary source must be known. The exergy is the maximum available potential for generating power from a source in comparison to a reference state called the environment. When the source is in complete equilibrium (thermomechanical and chemical) with the environment, it is said to be in the dead state from which no form of power can be extracted anymore (Moran et al., 2011).

The exergy of a stream can be calculated according to Eq. 7.1.2. In Eq. 7.1.2, chemical exergy and potential and kinetic energies contributions are neglected (Moran et al., 2011).

$$\dot{E} = \dot{m}[h - h_0 - T_0(s - s_0)] \tag{7.1.2}$$

where $\dot{m}$ is the mass flow rate (kg·s^{-1}), h is the specific enthalpy (kJ·kg^{-1}), evaluated at the actual stream temperature (T) and pressure (P), h_0 is the specific enthalpy (kJ·kg^{-1}) evaluated at the environment temperature (T_0) and pressure (P_0), s is the specific entropy (kJ·kg^{-1}·K^{-1}) at T and P, and s_0 is the specific entropy (kJ·kg^{-1}·K^{-1}) at T_0 and P_0.

For a control volume, the steady-state exergy balance can be written as follows:

$$0 = \sum_{i=1} \left(1 - \frac{T_0}{T_i}\right) \dot{Q}_i + \dot{W} + \sum_{j=1}^{\text{inlets}} \dot{E}x_j - \sum_{k=1}^{\text{outlets}} \dot{E}x_k - \dot{E}x_{\mathrm{d}} \tag{7.1.3}$$

where the first term is the exergy associated to the heat transfer $\dot{Q}_i$ (kW) occurring at a temperature T_i (K), $\dot{W}$ (kW) is the amount of exergy associated to power, and $\dot{E}x_{\mathrm{d}}$ is the amount of exergy destructed due to irreversibilities. At the limiting case $\dot{E}x_{\mathrm{d}}$ may be equal to 0 if no irreversibilities are present within the system, but it may never be negative. Details regarding the derivation of Eqs. 7.1.2 and 7.1.3 can be found in Chapter 7 of Moran et al., 2011.

The Second Law efficiency (η_{II}), also known as exergetic efficiency, can be written for a power cycle as the ratio between the generated net power and the exergy rate of the primary source as follows (Lee and Kim, 2015; Moran et al., 2011):

$$\eta_{\mathrm{II}} = \frac{\dot{W}_{\text{net}}}{\dot{E}_{\text{primary source}}} \tag{7.1.4}$$

η_{II} provides an insight of how efficiently the resources are being used in terms of the maximum available energy that can be extracted from the primary source. Furthermore, by performing an exergy balance for each component of a power cycle, it is possible to identify where the greatest exergy destruction and losses are occurring. Therefore, it possible to point out where changes must be firstly made in order to improve the cycle's performance (Moran et al., 2011).

η_{I} and η_{II} can be used to compare different power cycles with respect to their performance. However, in some cases, the most efficient power cycle may not be the most indicated one because it might require expensive equipment to properly work. In addition, when dealing with waste heat usage, it is necessary to carry out an economic assessment to identify if the additional power generation pays-off the required investment. The NPV (Sec. 3.7) may be use as a good indicator. Alternatively, the Levelized Cost of Electricity (LCOE) (US$·k^{-1}·h^{-1}) can be used (Pili et al., 2017). With the LCOE is possible to directly compare the cost of the electricity being produced with the electricity purchase cost from the local grid. Therefore, it is possible to identify if the proposed project is economically feasible.

$$\mathrm{LCOE} = \frac{\sum\limits_{j=1}^{\mathrm{lifetime}} \frac{C_{\mathrm{M},j}}{(1+i)^j} + C_{\mathrm{R},j}}{\sum\limits_{j=1}^{\mathrm{lifetime}} \frac{e_{\mathrm{y},j}}{(1+i)^j}} \tag{7.1.5}$$

where C_{M} (US$) is the maintenance cost of the jth year, C_{R} (US$) is the total real equipment cost as defined in Subsec. 3.7.1, i is the interest rate, and e_{y} (kW·h) is the electricity production of the jth year.

7.2 Rankine Power Cycle

One of the most important type of power cycle for electricity production, the Rankine power cycle uses water as working fluid and consists of four basic stages (ideal) (Fig. 7.1) (Çengel and Boles, 2007; Moran et al., 2011):

- 1-2: Saturated liquid water is pumped from the condenser pressure to the boiler pressure;
- 2-3: Water receives heat from the hot source and it is vaporized and superheated in the evaporator/boiler;
- 3-4: Superheated steam is expanded in a steam turbine producing power until it becomes a mixture of liquid and vapor;
- 4-1: Saturated vapor is condensed by giving up heat to the cold sink in the condenser until it reaches the saturated liquid state, closing the cycle.

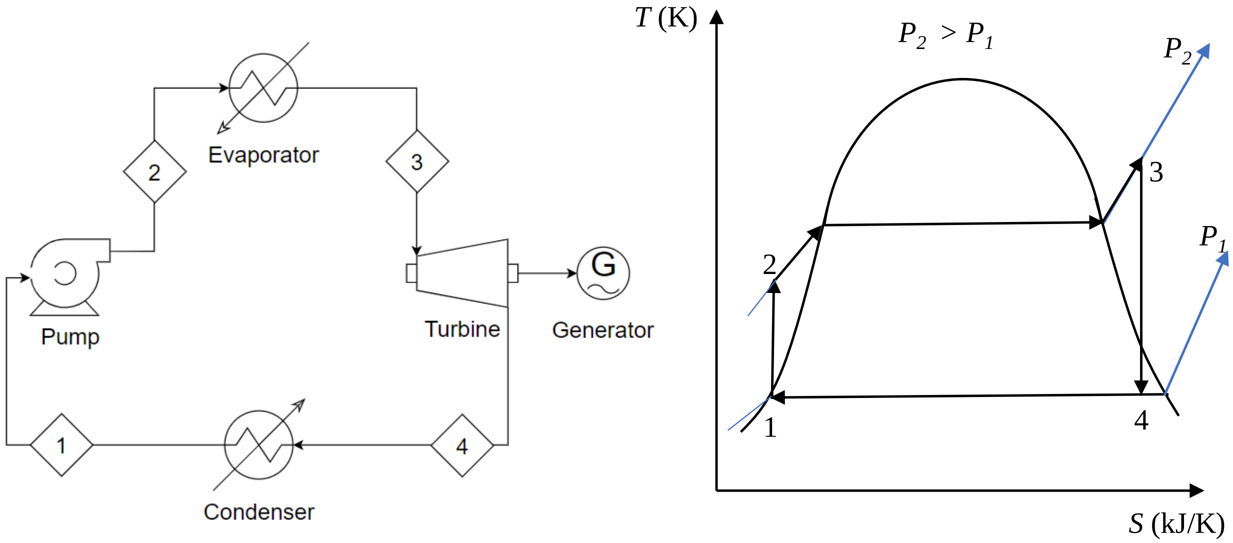

Figure 7.1: Ideal Rankine cycle on the left. Corresponding T x S diagram on the right (Adapted from Çengel and Boles (2007)).

The Rankine cycle efficiency can be increased by increasing the pressure and temperature of the vapor leaving the boiler and/or decreasing the condenser pressure. However, all these variables are subjected to process constraints. Increasing the boiler pressure also requires the material of construction to be more resistant. This, in turn, increases the boiler capital cost. Nowadays, a maximum operating pressure for the boiler of 30 MPa is adopted. Regarding the vapor temperature, it should not exceed 620 °C. At higher temperatures, the mechanical resistance of the boiler's material of construction, e.g., carbon steel, decreases considerably. Ceramics are promising materials for higher temperature operations. Regarding the condenser pressure, a lower pressure is achieved when the vapor is further expanded in the turbine. However, decreasing pressure makes vapor to condense inside the turbine, causing damage to the turbine blades. In addition, decreasing the pressure in the condenser requires the coolant to be at a lower temperature in order to condense steam. Usually, the coolant used is water, which is available at a temperature of 25 °C and should not return to the cooling tower at a temperature higher than 40 °C. Therefore, to keep a minimum temperature approach in the condenser, a pressure below 20 kPa at the turbine outlet is not desired (Çengel and Boles, 2007). Both temperature and pressure values presented in this paragraph are used as an initial guide during the design stage, but their values certainly change from plant to plant.

7.3 Organic Rankine Cycle (ORC)

Regarding waste heat usage in the industry, the Organic Rankine Cycle (ORC) also plays a vital role. The ORC configuration is identical to that of the conventional Rankine cycle (Fig. 7.1). The difference lies on the working fluid, which is usually an organic fluid as the name suggests. Vélez et al. (2012) present a review about the ORC and its potential application. According to the authors, the ORC technology is mature for applications in biomass and geothermal plants and for waste heat recovery. Manufactures are able to construct plants ranging from kW to MW of installed power, which is an indicator that the technology is already economically feasible even for small capacities.

The ORC working fluids can be divided into three classes: refrigerants, hydrocarbons, and siloxanes. The refrigerants are usually used to operate from 100 °C up to 175 °C, the hydrocarbons from 175 °C up to 250 °C and the siloxanes from 250 °C up to 400 °C (Vélez et al., 2012).

According to Badr et al. (1985), water is a good option for power cycles operating with a thermal source at a high temperature, e.g, 600 °C, because it can promote a high efficiency, it is stable, non-toxic and it is less expensive compared to other working fluids. In fact, for a conventional Rankine cycle, the feasible pressure can be attained only when the temperature of the heat source is elevated. However, waste heat sources are available at a considerably lower temperature (below 400 °C). In addition, water is a 'wet' fluid (Figure. 7.2-c), i.e., its liquid-vapor saturation curve has a negative $\mathrm{d}S/\mathrm{d}T$, which makes it condensate prematurely when expanded from a high pressure ($P1$) to a low pressure ($P2$) if a certain degree of superheating is not provided.

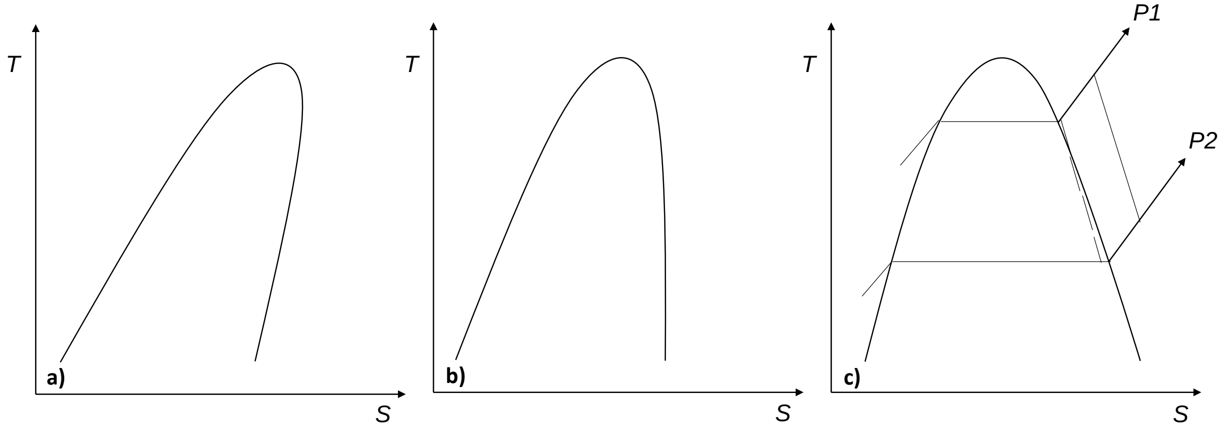

Figure 7.2: Saturation curve for: a) dry fluid, b) isentropic fluid, and c) wet fluid (Adapted from Badr et al. (1985) and Vélez et al. (2012)).

Casci et al. (1981) studied the implementation of an ORC in a ceramic kiln. The system was designed to transform the heat wasted in the kiln exhaust gases (200 °C - 250 °C) into power. The selected working fluid was tetrachlorethylene and the power produced by the cycle was 40 kW. The cycle efficiency was 58% of the Carnot efficiency[1]. The project, after an economic study, can be considered attractive. The payback period was estimated to be between 2.5 and 4 years. Using an average payback period, the internal rate of return was calculated to be 18% for a plant lifetime of 5 years.

Badr et al. (1985) list 13 criteria that the 'perfect' working fluid should possess, such as, to be stable at all conditions within the cycle, to be non-toxic, non-flammable, inexpensive, and promptly available on the market. One should refer to the original paper if more information about this matter is sought. Using the proposed criteria, the authors were able to reduce from a initial list of 68 to 3 fluids, namely the refrigerants R-11, R-113 and R-114. After an analysis of the cycle operating between 120 °C and 40 °C with the aforementioned fluids, the authors concluded that, R-113 was the best option and there is not a perfect fluid suitable for all scenarios. The fluid selection depends on the designer, which should evaluate the maximum number of possibilities, reducing them by a screening process followed by a cycle performance assessment.

Wolpert and Riffat (1996) carried out a theoretical study of an ORC coupled with an electrolyzer and a fuel cell. This energetic arrangement is supposed to provide power for households. The solar thermal energy is transferred to the working fluid of the ORC during the day. If the electricity production of the ORC is higher than the demand, the excess is used to produce hydrogen in an electrolyzer. The hydrogen is then stored to be used in the fuel cell to produce electricity when sunlight is unavailable. Different working fluids were studied, i.e., R134a, R152a, Klea32 and Care30. The ORC achieved the best performance working with R152a but, due to its flammability, Care30 was recommended by the authors. Operation with R152a, the ORC was able to achieve almost 70% of the Carnot efficiency whereas 64% was achieved with Care30. Although the cycle configuration is very interesting, the research lacks economic data, which might prove the feasibility of implanting such power plant.

Maizza and Maizza (2001) studied the performance of the ORC for 25 different working fluids for a evaporator temperature between 80 °C and 110 °C and a condenser temperature between 35 °C and 60 °C. By means of simulations, the authors showed that the fluids R-600a, R-123 and R-124 are the most appropriated. The authors also advise to use fluids, which are able to be condensed and vaporised within the pressure range of 0.1 MPa and 2.5 MPa.

Yamamoto et al. (2001) conducted an study of an Rankine cycle using water and HCFC-123

---

[1] Calculated as $1 - \frac{T_C}{T_H}$, where T_C is the lowest temperature (K) of the power cycle's cooling fluid and T_H is the highest temperature (K) of the primary energy source.

as working fluids. The analysis, which were based on both computer simulations and on experiments, showed the better performance of the cycle when operated with HCFC-123 for the temperature range under consideration (120 °C - 200 °C). The cycle's performance increases when water is superheated before entering the turbine, but for the HCFC-123 it is better when the temperature is as close as possible to saturation. The authors concluded that this behavior is due to the lower latent heat of HCFC-123.

Nguyen et al. (2001) performed an experimental study of a micro-scale ORC (1,5 kW) operating with *n*-pentane. The cycle average efficiency was 4% due to the low turbine inlet temperature (81 °C). This value is approx. 33% of the Carnot efficiency. The turbine isentropic efficiency (estimated to be 50%) was the major contributor to the low efficiency ratio. After an economic analysis, the electricity price was calculated to be 64.36 p/kWh, with a TCI of £21,560 for an interest rate of 10% and a project lifetime of 5 years.

Liu et al. (2004) carried out a thermodynamic analysis of several working fluids for the ORC. The authors found out that fluids with strong hydrogen bond such as water and ethanol have a greater heat of vaporization and are wet, which is an undesired characteristic for the ORC. In addition, both the thermal and the heat recovery efficiency of the cycle are small for working fluids with lower critical temperature.

Drescher and Brüggemann (2007) studied the effect of hundreds of working fluids on the ORC for biomass and power plant applications. After an screening process, over 100 fluids were able to provide an efficiency between 24.3% to 25.4%. The maximum temperature was 300 °C and the minimum was 90 °C. In addition, it was shown that superheating is undesired because it reduces the cycle efficiency. Increasing the maximum temperature also increases the cycle efficiency. Moreover, fluids with higher critical temperatures made the cycle more efficient, which corroborates with the conclusion presented by Liu et al. (2004) and the first criterion used by Badr et al. (1985) in his fluid screening study. The fluids of the alkylbenzenes family provided the best cycle performance for this study.

Wei et al. (2007) simulated an ORC able to produce 100 kW. The simulations were validated using experimental data of an ORC plant that uses the heat coming from the gas turbine exhaust gas. The working fluid was R-245fa. After a parametric study it was found that the subcooling temperature in the condenser should be between 0.5 K and 0.6 K for a given evaporator temperature. This occurs because subcooling the working fluid to lower temperature levels would require more heat to be supplied in the evaporator to achieve the desired superheating level. This makes the plant efficiency to decrease. The ambient temperature plays a significant role in the cycle performance. Since air was used as cooling media, with the increase of the ambient temperature for a given waste heat source temperature, the cycle efficiency decreases. Increasing the ambient air temperature from 280

K to 345 K makes the cycle efficiency decrease from 10% to only 3%.

Saleh et al. (2007) studied 31 dry and wet fluids for both subcritical and supercritical operation. The dry fluids in subcritical condition yielded the highest cycle efficiency (up to 14%) for a maximum temperature of 100 °C. For these fluids, superheating is not recommended. R600, R601a, and R245fa are among the recommended dry fluids. However, for a specified installed power, these fluids require a higher mass flow rate of the heat source due to pinch limitation in the evaporator. When a low mass flow rate of heat source is desired, operating the cycle with supercritical fluid is an alternative. For cases in which the working fluid at the turbine outlet was still at superheated state - common situation for dry fluids -, the use of an intermediate heat exchanger prior to the condenser showed an average increase of 1% in the cycle efficiency. The authors suggest that for temperatures higher than 100 °C, the best working fluid are likely to be dry.

Mago et al. (2008) compared the performance of the ORC with the regenerative ORC (Fig. 7.3 - a) for 5 different dry and isentropic fluids. For all of them, the regenerative arrangement has shown a better performance considering both first and Second Law of thermodynamics. In addition, superheating the working fluid in the evaporator was proven to not be advantageous. Therefore, dry and isentropic fluids should preferably leave the evaporator as close as possible to the saturation condition.

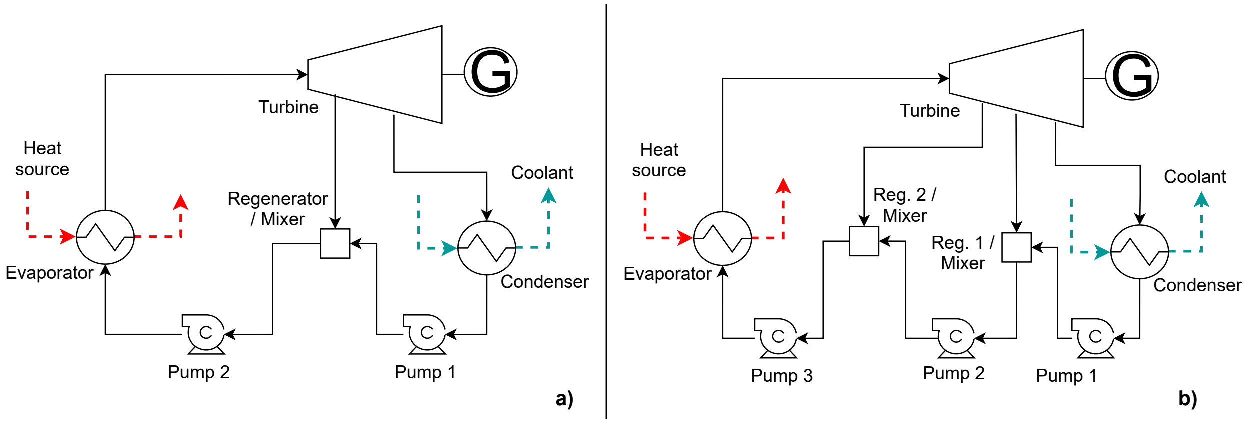

Figure 7.3: Single (a) and double (b) stage regenerative ORC (Imran et al., 2014).

Tchanche et al. (2009) carried out a fluid selection study. The study evaluated 20 fluids for a 2 kW ORC using hot water at 90 °C as heat source. Beside some of the fluid selection criteria considered by Badr et al. (1985), the authors have also taken into account the Ozone Depletion Potential (ODP) and the Global Warming Potential (GWP) of the fluids in their analysis. In fact, if one of the fluids under consideration had either a high ODP or a high GWP, its use was rejected. This was the case for the fluids R12 and R500. For the scenario under consideration, the refrigerant R134a was considered the most suitable, but the fluids

R152a, R290, R600, and R600a were also recommended.

Nguyen et al. (2010) performed a study about the Rankine cycle operating with water, ammonia and hydrocarbons in the temperature range of 100 °C - 250 °C. Despite of water having the greatest capability of generating power per kg of fluid (probably due to its high heat for vaporisation), it was the fluid with the worst net power generation among the set of the selected fluids. In addition, since water is a wet fluid, it needs to be superheated to avoid condensation inside the turbine. The authors recommended the use of hydrocarbons for the temperature range studied because of their dry characteristic, the higher net power generation and greater cycle efficiency.

Sun and Li (2011) optimized a ORC operating with R134 and considering air as cooling fluid in the condenser. Using a derivative-free algorithm, either the thermal efficiency or the net power generation was optimized. The values of the working fluid flow rate, the air flow rate and the expander inlet pressure were chosen as decision variables. By increasing the expander inlet pressure, a higher efficiency and a higher net power generation was obtained. However, increasing the pressure indiscriminately affects the capital and operating cost of the plant and it might affect the working fluid thermal stability. Moreover, the working fluid flow rate has a greater effect on the cycle performance than the cooling air flow rate.

Bao and Zhao (2013) carried out a comprehensive review about the ORC working fluids and expansion machines, discussing the limitation of each type and listing the performance of prototypes and the manufactures on the global market.

Imran et al. (2014) optimized the capital cost and the performance of an usual ORC and two different regenerative ORC: single stage and double stage (Fig. 7.3). The study was conducted for wet, isentropic and dry fluids. The authors found out that the most influential variable on both the capital cost and cycle thermal efficiency is the evaporator pressure. In addition, it was shown that superheating the working fluid inside the evaporator was unnecessary because it did not cause a great increase in the cycle's thermal efficiency, but it considerably increased its capital cost. Moreover, double stage regenerative ORC had the best thermal efficiency, but the highest capital cost whereas the regular ORC had the worst performance, but the lowest capital cost. Unfortunately, the results were indecisive to conclude whether the double stage regenerative ORC higher efficiency was enough to pay off for its higher capital cost.

Peris et al. (2015) studied the performance of a recuperative (Fig. 7.4) ORC in industrial conditions. The hot gases of a ceramic furnace were used to heat a thermal oil, which was then used in the cycle evaporator as heat source. R245fa was the working fluid. The authors compared the performance of the cycle in industrial condition with its early performance in laboratory condition. The results showed no significant difference. The maximum expander electrical isentropic efficiency was 65% and the maximum cycle net efficiency was 10.94%. For a year of operation, a net electricity production of 115 MWh was estimated. An economic analysis has shown that, for a project life of 15 years with an interest rate of 2%, the payback is less than 5 years and the internal rate of return is 22.88%.

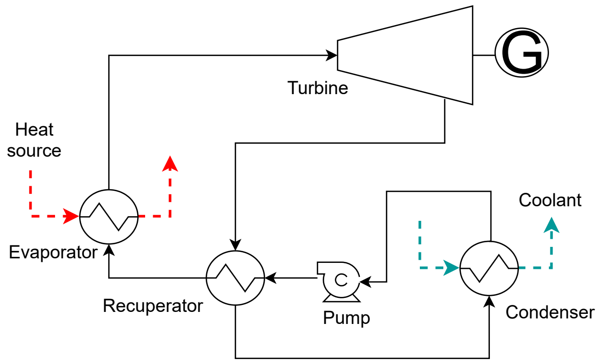

Figure 7.4: Recuperative Rankine/ORC (Peris et al., 2015).

Wang et al. (2015) evaluated the possibility of implementing an ORC to recover waste heat from an air stream in a cement industry. The studied working fluids were hexane, isohexane, R601, R123 and R245fa. After a performance and economic analysis of the cycle, R601 was found to be the most appropriate working fluid. The R601 critical temperature (approx. 197 °C) is close to the heat source temperature (220 °C). According to the authors, when the working fluid has a critical temperature close to the thermal source temperature, the irreversibilities in the evaporator are reduced. Therefore, the cycle efficiency increases. The highest cycle efficiency of 19.1% was achieved with R601. The ORC capital cost was estimated to be 2.5 M€ with a payback period varying from 2.74 to 3.42 years. The net present value (NPV) varied from 6.4 M€ to 8.4 M€ with a project lifetime of 20 years and an interest rate of 5%. The elevated profitability of the project might be due to the lower interest rate. However, considering the current NPVs, it can be assumed that even with a higher interest rate, the project would still be profitable. Nevertheless, the payback period would be elevated.

Muhammad et al. (2015) built a 1 kW ORC, which operates using steam (maximum temperature of approx. 130 °C) as heat source. After a working fluid screening procedure, R245fa was judge to be the best option. The authors found out that the increase of the expander inlet pressure improves the power generation, but decreases the expander isentropic efficiency. This was pointed out as the major reason for achieving a maximum thermal efficiency and a maximum power output at different pressures. The expander isentropic efficiency varied from 58.3% to 77.74%. The degree of superheating at the evaporator outlet was also investigated.

The results showed that superheating should be avoided - R245fa is an isentropic fluid -, but it cannot be completed eliminated because the heat loss to the environment prior the expander inlet. Therefore, a safety superheating degree should be adopted. The authors were unable to reduce the superheating temperature below 10 °C in their experiments. The pump power consumption greatly affects the net power generation whereas in the usual Rankine cylce, the pump work is usually negligible compared to the turbine power generation. Regarding this matter, the Misselhorn power cycle has the advantage of not requiring pumps, which in turn, increase the the net power generation.

Gleinser and Wieland (2016) performed a theoretical study of the Misselhorn cycle for power production from waste heat source. The Misselhorn cycle is similar to the ORC but it has more than one evaporator that operates batchwise. The working fluid is feed into the evaporator forming a pool. The heat source exchanges heat with the working fluid inside the evaporator. With the temperature increase, since the working fluid is kept inside the evaporator with constant volume, the pressure also increases. After the evaporation, the discharge valve is opened, allowing the vapor to expand in the turbine. To produce power continuously, a minimum of three evaporators are necessary. The evaporation with constant volume permits a better temperature match in the evaporator, which increases the cycle efficiency. In addition, the pressure increase occurs during evaporation of the working fluid in a closed vessel, i.e., the evaporator. This avoids pump power consumption. Gleinser and Wieland (2016) showed that for a heat source at 100 °C, the Misselhorn cycle with three evaporators has an efficiency of 29.8% while the ORC presented an efficiency of 26.8% working with R134a. With the increase of the number of evaporators, the Misselhorn cycle efficiency also increases. With ten evaporators, its efficiency was calculated to be 44.4%, which corresponds to an increase of approx. 65% of the ORC efficiency. However, increasing the number of evaporators presents drawbacks. The higher the number of evaporators, the higher the cycle capital cost and the controlling complexity.

Yu et al. (2016) has shown how the characteristic of the waste heat source affects the working fluid selection. The waste heat sources were divided into three groups: only able to supply sensible heat, sensible heat plus latent heat, and only latent heat. According to the authors, for waste heat sources able to supply only latent heat, any working fluid is able to completely extract the heat from the waste source and the analysis of which one to choose is basically based on the net power generation. However, this is not the case for the other two waste heat sources groups because of pinch point inside the evaporator changes according to the fluids characteristics. For sensible heat sources, it was found that the best working fluid is the one with a critical temperature in the range of 25 °C to 35 °C below the waste heat temperature at the inlet of the evaporator, which corroborates with the results found by Wang et al. (2015). In addition, for sensible plus latent waste heat sources, it was shown that the ratio between the sensible and the latent heat has a great effect on the working fluid performance within the cycle.

Landelle et al. (2017) carried out a vast literature review regarding studies about the ORC. The review focuses on the equipment, manly on the different types of expanders and pumps. Regarding the expander, an average adiabatic efficiency 56% was encountered, but this value is dependent on the mechanical power of the equipment following a linear trend. The higher the mechanical power, the higher the efficiency. By means of an statistical analysis, it was shown that the cycle thermal efficiency is strongly dependent on the power scale, expander efficiency and hot source temperature, in this order. The use of an intermediate heat exchange - recuperative ORC - can also improve the cycle performance, but its effect is limited.

Pili et al. (2017) studied alternatives to implement in an ORC for heat sources suffering fluctuations in either its temperature or its mass flow rate. For variations of the heat source temperature, the use of a heat storage tank has proven to be the best option. For mass flow rate fluctuations, a by-pass was suggested for values above 120% of the design value. The choices were based on the economic performance of the cycle by means of the levelized cost of electricity and on the reduction potential of CO_2 emissions.

Braimakis and Karellas (2018) proposed different ORC cycle arrangements, combining the recuperative with the regenerative configuration. By comparing their performance with the standard recuperative ORC configuration, they concluded that recuperative cycles have always a higher efficiency than non-recuperative regenerative cycles. Recuperative regenerative cycles have shown the best performance for all fluids under consideration, however. Finally, both recuperative and regenerative cycles are more efficient when working with dry fluids.

Scaccabarozzi et al. (2018) have carried out a very detailed fluid selection based on the maximization of the exergy efficiency of the ORC for more than 40 fluids (pure and mixtures). The work aimed to make use of the ORC for recovering the heat rejected by 2 different heavy-duty diesel engines (approx. 10 MW of mechanical power each). The authors used 2 approaches: Heat recovery only for power generation and heat recovery for combined heat and power generation. For both cases, the best pure and fluid mixtures were mostly dry and the cycle was supercritical and recuperative. Supercritical operation led to a better temperature match between the working fluids and the heat source in the evaporator, thus, a higher exergy efficiency was achieved. Moreover, the authors concluded that the slightly higher efficiencies obtained for fluid mixtures in comparison with pure fluids might not suffice to justify its use because of the lower heat transfer coefficient in the evaporator, which would require a larger heat exchanger, thus, more expensive. Finally, the literature lacks data regarding thermal stability for most the ORC working fluids, including those found to be optimum in this study. Therefore, the authors advise the execution of further experimental study regarding this matter.

Sun et al. (2020) evaluated the thermo-economic performance of a double pressure recuperative ORC for three working fluids, namely, R21, R114, and R245fa. The cycle under consideration is depicted in Fig. 7.5. The best result was obtained for the R245fa and the turbine inlet pressure has shown a greater effect on the cycle performance than the inlet temperature. In addition, there is a certain optimum value of around 1,800 kPa and 900 - 1,100 kPa for the high and low turbine inlet pressure, respectively. For all fluids, the double pressure recuperative ORC has shown a superior performance in comparison with the standard ORC.

Feng et al. (2020) optimized the performance of a recuperative ORC (Fig. 7.4) by varying the working fluid superheating degree at the evaporator outlet, working fluid mass flow rate and by varying the heat exchange area of each heat exchanger, but keeping the total heat exchange area fixed. After the optimization, the cycle's power output was increased by 25.22% and the thermal efficiency by 12.16%.

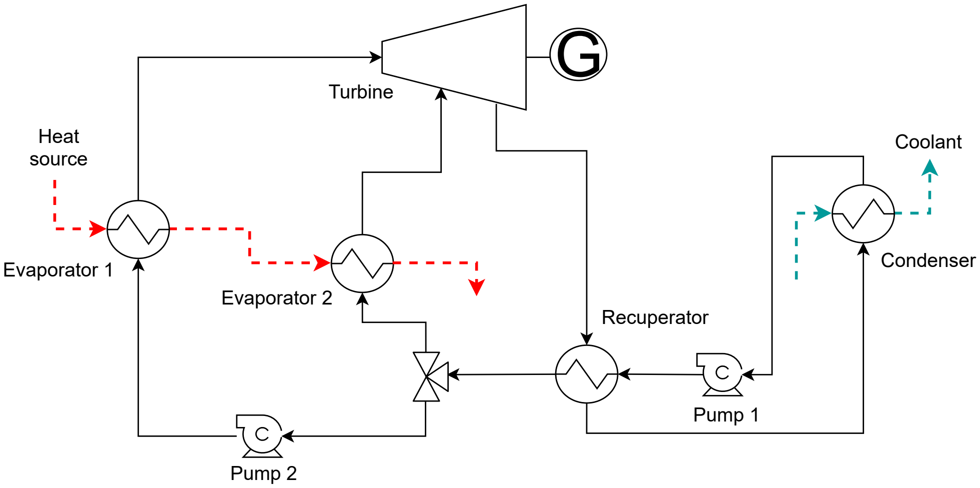

Figure 7.5: Double pressure recuperative ORC (Sun et al., 2020).

Tian et al. (2020) studied the possibility of using the ORC for heat recovery of a ship engine when operating with LNG. The idea was to use the LNG as cooling medium in the condenser and to use the engine exhaust gas and jacket cooling water in parallel as heat sources. The system was comprised of three thermally integrated conventional ORC units and each unit operated with a different working fluid. After optimization, the system shown an average First Law efficiency of 14.5%, power generation of 210 kW, and capital cost of US$ 1.9 million with a payback period of approx. 8.5 years.

Al-Janabi et al. (2021) evaluated the economic feasibility of implanting an ORC running with R-245fa for industrial waste heat recovery in 5 different locations. The waste heat source temperatures varied from 60 °C to 115 °C. Waste heat source temperature played a major role in the cycle's efficiency and consequently in its economic performance. The lower the heat source temperature, the worst the net power generation, which varied from -3.16 kW (higher power consumption than production) to 29.9 kW. Nevertheless, with the heat source temperature of 115 °C and net power generation of 29.9 kW the system has proven to be economically feasible with a pay-back period of 6.3 years for an electricity price of 0.078 $/kW.

Fierro et al. (2021) investigated the possibility of using hot air (240 °C) from the cooling system of a rotary kiln as heat source of RORC operating with cyclopentane. The First and Second law efficiencies were 17.35% and 48.62%, respectively, and the net power generation were approx. 865 kW. For an electricity price of 0.12 US$/kWh and rate of return of 5%, the NPV was MUS$ 0.06 and payback time of 12 years.

From the power cycles literature review, it can be concluded that water is appropriate as working fluid if the primary energy source is at a high temperature, e.g., > 400 °C. That is advised by Badr et al. (1985) and it was shown by Nguyen et al. (2010) and Yamamoto et al. (2001). Also, it has a relatively high latent heat and it needs to be superheated before entering the turbine to avoid premature condensation because it is a wet fluid. For a primary energy source able only to provide sensible heat, e.g., exhaust gas from an engine, those characteristics decrease the evaporator/boiler exergetic efficiency due to a poor temperature match (Gleinser and Wieland, 2016). Considering that hundreds of working fluids are available, the most appropriate working fluid can only be chosen after an extensive analysis composed by different criteria, which vary from author to author as shown by Badr et al. (1985), Maizza and Maizza (2001), Scaccabarozzi et al. (2018), and Tchanche et al. (2009).

In terms of operational conditions, maximum and minimum operating pressures are not fixed. Despite the recommendation made by Imran et al. (2014), Maizza and Maizza (2001), Sun and Li (2011), and Sun et al. (2020), the maximum operating pressure is ultimately constraint by the capital cost. The higher the operating pressure, the higher the capital cost, but the higher the cycle efficiency. regarding temperature, for a primary energy source able to provide only sensible heat, the proper working fluid is that which has a critical temperature in the range of 25 °C to 35 °C lower than the primary energy source, provided that the power cycle is subcritical (Yu et al., 2016). By doing so, irreversibilities are reduced due to a better temperature match in the boiler (Badr et al., 1985; Drescher and Brüggemann, 2007; Liu et al., 2004; Saleh et al., 2007). For transcritical operation, the temperature match is improved, but dry or isentropic fluids tend to leave the turbine with an elevated degree of superheating, which jeopardizes the cycle's performance. An alternative is to use a recuperator (Braimakis and Karellas, 2018; Mago et al., 2008; Saleh et al., 2007), but its effect on the cycle's performance is limited (Landelle et al., 2017). At last, the Misselhorn cycle has proven to provide the best temperature match as shown by Gleinser and Wieland (2016), but it has a relatively more complex arrangement. Furthermore superheating of dry and isentropic fluids inside the boiler must be avoided (Drescher and Brüggemann, 2007; Imran et al., 2014; Mago et al., 2008; Muhammad et al., 2015; Saleh et al., 2007). However, to avoid premature condensation before entering the turbine, at least some degree of superheating must be provided, e.g., 10 °C (Muhammad et al., 2015);

Most studies found on the literature are focused on recovering heat from sources able to provide only sensible heat. In the chemical industry, however, several medium temperature (473-573 K) exothermic reactions take place. The heat released by such reactions are usually used to generate low pressure saturated steam, which might be of low economic value for the plant. In addition, for plants in which high pressure gases are used or produced, the power demand due to compression is elevated. Hence, the conversion of the energy in low pressure steam into electricity is the opportunity to be investigated in this part of the work.

Chapter 8

Power Cycle Simulation and Thermoeconomic Assessment

This chapter begins with the description of how the working fluids are pre-selected for the power cycle simulations. In the subsequent section a description of how the power cycles are modeled, simulated and assessed in terms of their thermodynamic performances is presented along with the required equations. Afterwards a discussion about the simulations results for each pre-selected fluid is presented. In the final section it is explained how the economic evaluation is carried out along with a detailed procedure for estimating the heat exchangers areas. The analysis result is shown and the decision of what working fluid best suits the process under consideration is made.

The power cycles are modeled in Python 3.8.10. Python is a very powerful object-oriented programming language and it is also relatively easy to be learned. In addition, there are hundreds of different packages available, which makes easy to solve algebraic equation system, to display figures and, most important for this work, to calculate thermophysical properties. That is accomplished by the CoolProp 6.4.1 package (Bell et al., 2014). CoolProp was developed based on literature-available high-accuracy equations of state and physical properties formulations. In CoolProp thermodynamic properties are estimated from the total Helmholtz energy. For physical properties, different correlations are adopted since there is not a unique one able to represent all fluids. Finally, Python and the packages used in this work are free of any charge.

8.1 Working Fluids Preliminary Screening

The following criteria are used to perform the first step of selecting the most appropriate working fluid:

1. The working fluid must be able to condense at an approx. temperature of 45 °C near atmospheric pressure. Cooling water is used as coolant in the condenser. Therefore, some precaution regarding the temperature difference between the fluids must be taken;

2. It is reported in the literature that expanding the working fluid to lower sub-atmospheric pressures in the turbine may cause air to leak into the system (Badr et al., 1985; Maizza and Maizza, 2001; Tchanche et al., 2009). However, there is not a consensus on setting up a minimum value for the pressure. Therefore, a constraint regarding the condenser pressure is not imposed in this work;

3. The working fluid must be able to vaporize at a temperature close to those of the primary energy source (Tab. 8.1), which is the saturated steam coming from the reactors designed in Part I. As previously seen from the literature review, the better the temperature match in the boiler, the higher the exergetic efficiency of this equipment. Therefore, a slack of approx. ±30 °C compared to the average primary energy source's temperature is considered to select the desirable fluids;

4. Health and environmental aspects are also taken into account. The CFCs (Chlorofluorocarbons) and the HCFCs (Hydrochloroflurocarbons) shall be disregarded due to their high Global Warming Potential (GWP). A safety classification according to the American National Fire Protection Association (NFPA) is also used. The scale goes from 0 to 4, where 4 means the most elevated risk and zero means no risk for health (H), flammability (F), stability (S) and other hazards (O). All fluids to be selected in this work must be stable and have a low to moderate health hazard classification (From 0 up to 2).

Table 8.1: Saturated steam stream information from the reactors optimization scenarios.

	OPT1	OPT2	OPT3
T (K)	478	506	487
$\dot{Q}_{\text{boiler}}$ (MW)	16.4	1.3	5.1
$\dot{m}$ (kg·s^{-1})	8.50	0.72	2.69

The working fluids for the primary screening are chosen from a broader range of fluids present in the lists of Bao and Zhao (2013), Maizza and Maizza (2001), Nguyen et al. (2010), and Tchanche et al. (2009). By applying the aforementioned guidelines, the number of initially considered working fluids was narrowed down from 78 to 6 as shown in Tab. 8.2 (See $T \times s$ and $T \times h$ diagrams in Fig. 8.1).

Table 8.2: Pre-selected working fluids.

Substance	T_c (°C)	P_c (bar)	Type	HFSO	Reference
Ethanol	241	61.5	wet	1300	Fisher (2014) and Tchanche et al. (2009)
Methanol	240	81	wet	2300	Fisher (2015a) and Tchanche et al. (2009)
R601 (*n*-pentane)	197	33.6	dry	1400	Fisher (2015b) and Tchanche et al. (2009)
Cyclopentane	238	45.1	dry	130n.a.	Chevron-Phillips (2018) and Nguyen et al. (2010)
R610 (Diethyl-ether)	193	36.4	dry	040n.a.	Bao and Zhao (2013) and Sigma-Aldrich (2015)
HMDSO (Hexam-ethyldisiloxane)	245	19.1	dry	241n.a.	Fisher (2009) and Tchanche et al. (2009)

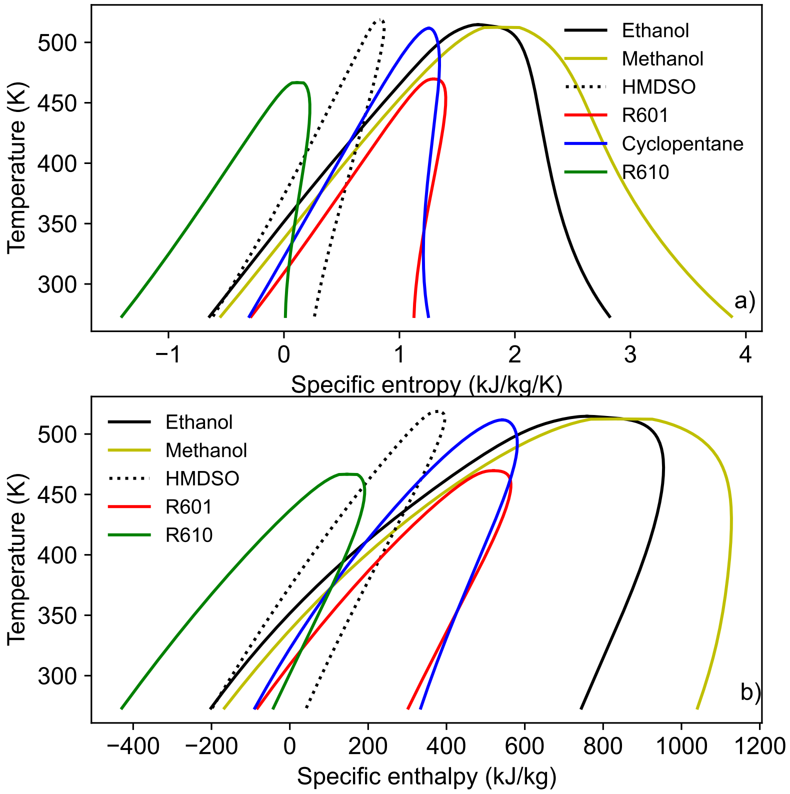

Figure 8.1: Selected working fluids $T \times s$ (a) and $T \times h$ (b) diagrams.

8.2 ORC Configuration

Two power cycle configurations are under consideration: the conventional (Fig. 8.2-a) and the recuperative (Fig. 8.2-b). For wet fluids, only the usual configuration is tested for subcritical operation. For dry and isentropic fluids, both usual and recuperative cycles are tested. As known from the literature review, dry and isentropic fluids tent to leave the turbine with a certain degree of superheating. Therefore, it will be investigated if the improvement in terms of power generation caused by the use of a recuperator pays off the additional capital cost.

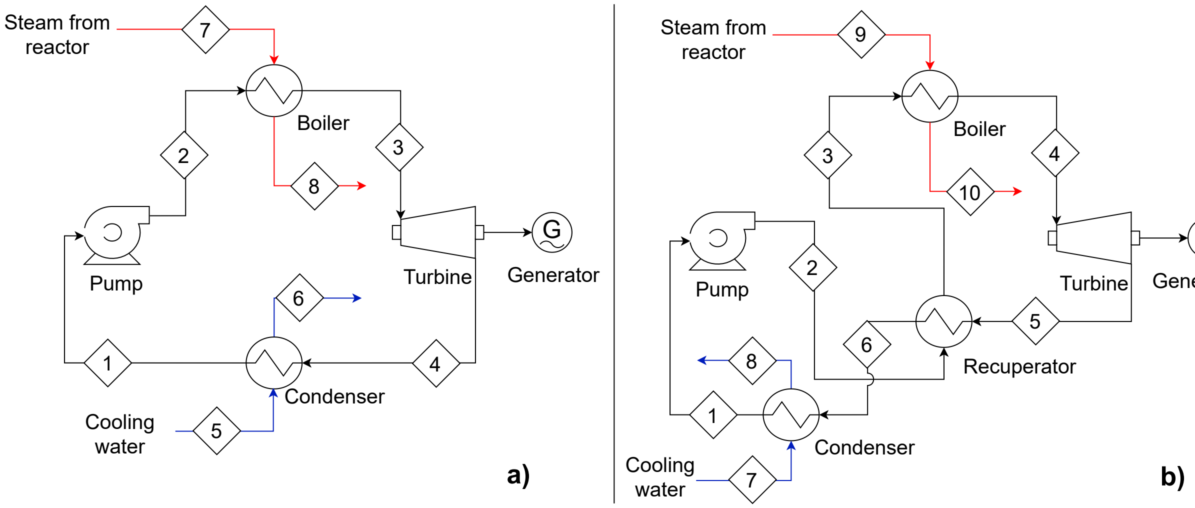

Figure 8.2: Conventional ORC (a) and recuperative (RORC)(b).

8.2.1 Power Cycle Modeling and Simulation

Both usual and recuperative ORCs were modeled in Python 3.8.10. Thermophysical properties were estimated using CoolProp 6.4.1 package (Bell et al., 2014). All equipment are assumed to be adiabatic with respect to the environment. Thus, turbine (η_{turbine}) and pump (η_{pump}) isentropic efficiencies can be expressed according to Eqs. 8.2.1 and 8.2.2, respectively.

$$\eta_{\text{turbine}} = \frac{\dot{W}_{\text{turbine}}}{\dot{W}_{\text{turbine, ise}}} = \frac{h_{\text{in}} - h_{\text{out}}}{h_{\text{in}} - h_{\text{out, ise}}} \tag{8.2.1}$$

$$\eta_{\text{pump}} = \frac{\dot{W}_{\text{pump, ise}}}{\dot{W}_{\text{pump}}} = \frac{h_{\text{out, ise}} - h_{\text{in}}}{h_{\text{out}} - h_{\text{in}}} \tag{8.2.2}$$

where the subscript "ise" means isentropic.

The energy balance for hot and cold streams in the heat exchangers are expressed in Eqs. 8.2.3 and 8.2.4, respectively.

$$\dot{Q} = \dot{m}_{\text{hot}}(h_{\text{hot, in}} - h_{\text{hot, out}}) \tag{8.2.3}$$

$$\dot{Q} = \dot{m}_{\text{cold}}(h_{\text{cold, out}} - h_{\text{cold, in}}) \tag{8.2.4}$$

To simulate the power cycles in steady-state some assumptions are made:

1. Working fluid leaves the condenser as saturated liquid;
2. Both pump and turbine isentropic efficiencies are equal to 85% and 70%, respectively (Landelle et al., 2017; Muhammad et al., 2015; Nguyen et al., 2001; Peris et al., 2015; Quoilin, 2011);
3. Minimum temperature approach (ΔT_{min}) in heat exchangers are set to be equal to 10 K (Seider et al., 2016);
4. Heat exchangers operate in counter-current;
5. Pressure drop (ΔP) in pipes and fittings is neglected. For heat exchangers it is set as follows (Seider et al., 2016; Sinnott, 2005):
   (a) 0.15 bar for streams with pressure below 1 bar;
   (b) 0.6 bar for liquids;
   (c) 1.0 bar for high pressure gases (> 10 bar);
   (d) 0.5 bar for low pressure gases (< 10 bar).
6. Cooling water inlet and outlet temperatures are 298.15 K and 313.15 K, respectively.
7. Kinetic and potential energies variations are considered negligible;

The power cycle simulation starts at stream 1 (Fig. 8.2-a) by taking into account assumption #1 and guessing its temperature (T1). By defining T1, stream 1 properties can be found. By setting the pump discharge pressure and using Eq. 8.2.2 and assumption #2, both the specific required pump power (kW/kg) and stream 2 can be determined. In the boiler, the hot fluid is saturated steam (Tab. 8.1), which must leave as saturated liquid to be used as the reactor cooling fluid. Therefore, the hot fluid stream is always determined in the boiler. The cold fluid outlet temperature (working fluid) is either set to be 5 K above the saturation temperature if the working fluid is dry or to be 10 K below the heat source inlet temperature (assumption #3) if it is wet, provided that it has achieved at least 20 K of superheating so that premature condensation inside the turbine can be mitigated. With the hot fluid information, stream 2, Eq. 8.2.3 and Eq. 8.2.4, the working fluid mass flow rate and stream 3 can be determined. Stream 4 pressure is determined because of stream 1 and assumption #5. Therefore, by using Eq. 8.2.1 and assumption #2, the power generate by the turbine and stream 4 can be determined. With stream 1 and 4 data, assumption #6 and Eq. 8.2.3 and Eq. 8.2.4, the cooling water mass flow rate can be found, thus, all variables are determined. However, the aforementioned procedure can only be executed if T1 is firstly guessed.

By guessing T1, assumption #3 might not be satisfied in the condenser. Differently from the boiler, if the working fluid leaves the turbine as superheated vapor, in the condenser the pinch may occur anywhere between inlets and outlets instead of in one of the end points as exemplified in Fig 8.3. Therefore, T1 must be found iteratively. The procedure is described in Fig. 8.4 and it can be solved by any root-finder algorithm. In this work, the function *fsolve* from the Scipy v1.6.2 optimizer package is used.

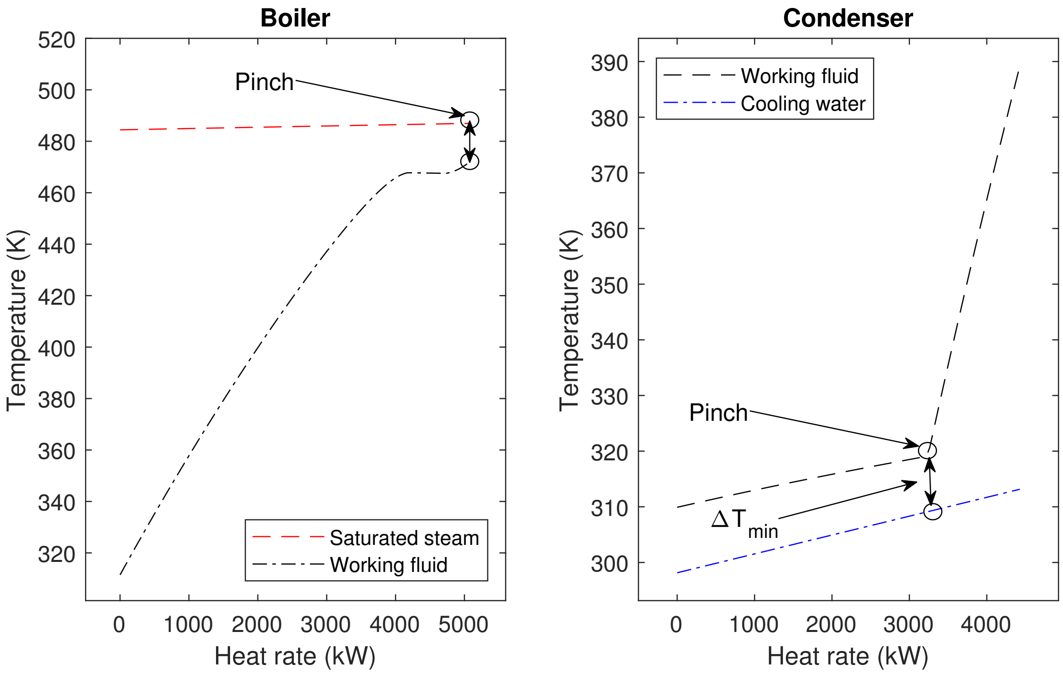

Figure 8.3: Usual pinch location in a boiler (left) and a condenser (right).

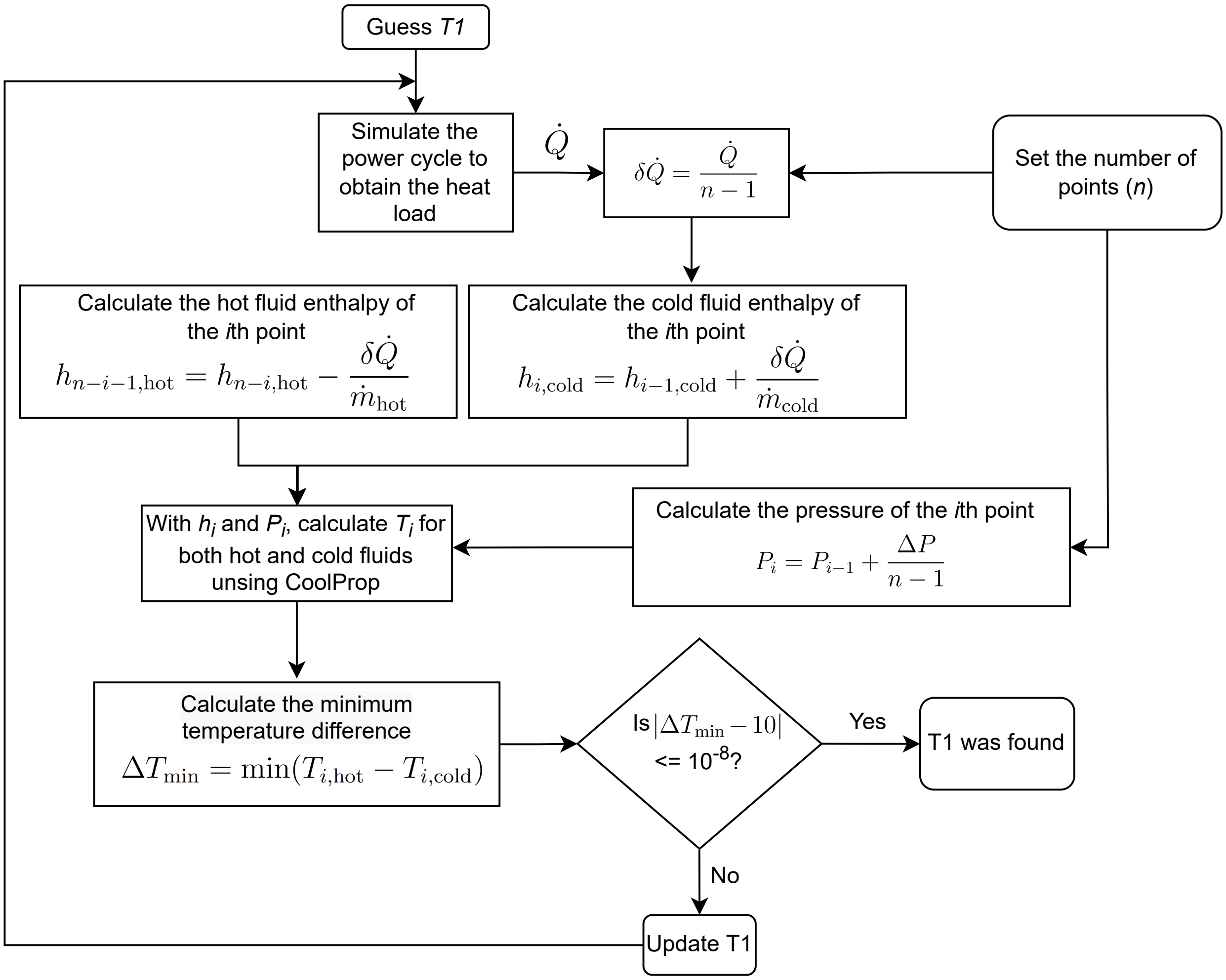

Figure 8.4: Iterative procedure to calculate stream 1 temperature.

For simulating the recuperative ORC (Fig. 8.2-b), the procedure is slightly different. Firstly, both the condenser outlet stream (T1) and recuperator cold stream (T3) temperatures must be found iteratively. The procedure executed for finding T3 is the same as previously explained for finding T1. Secondly, the boiler working fluid outlet stream temperature was set to be equal to 10 K below the heat source inlet temperature. Although only dry fluids are tested for the recuperative configuration, the use of a recuperator mitigates the jeopardizing effect of superheating the working fluid. Apart from those changes, the recuperative ORC simulation is performed the same manner as for the usual ORC.

The power cycles thermodynamic performance is assessed by calculating both First (η_{I}) and Second (η_{II}) Laws efficiencies. η_{I} is calculated using Eq. 7.1.1, where $\dot{Q}$ is the amount of energy transferred as heat from the saturated steam to the working fluid (Eq. 8.2.5), and $\dot{W}_{\mathrm{net}}$ is the difference between the amount of power generated by the turbine $\dot{W}_{\mathrm{turbine}}$ and consumed by the pump ($\dot{W}_{\text{pump}}$) (Eq. 8.2.6).

$$\dot{Q} = \dot{m}_{\text{steam}}(h_{\text{in}} - h_{\text{out}}) \tag{8.2.5}$$

$$\dot{W}_{\text{net}} = \dot{W}_{\text{turbine}} - \dot{W}_{\text{pump}} \quad \text{or} \quad \dot{W}_{\text{net}} = \dot{m}_{\text{fluid}}[(h_{\text{in}} - h_{\text{out}})_{\text{turbine}} - (h_{\text{out}} - h_{\text{in}})_{\text{pump}}] \tag{8.2.6}$$

η_{II} is calculated using Eq. 7.1.4, in which $\dot{E}_{\text{primary source}}$ is the difference between the steam exergy entering and exiting the boiler (Streams 7 and 8, and 9 and 10 in Figs. 8.2-a and 8.2-b, respectively), which can be estimated according to Eq. 7.1.2, considering the reference state (the environment) at 25 °C (T_0) and 101 kPa (P_0). Alternatively, η_{II} can be estimated according to Eq. 8.2.7 (Lee and Kim, 2015).

$$\eta_{\text{II}} = 1 - \sum_{i}^{\text{equipment}} \frac{\dot{E}_{\text{d},i}}{\dot{E}_{\text{primary source}}} - \sum_{j}^{\text{streams out}} \frac{\dot{E}_{\text{loss},j}}{\dot{E}_{\text{primary source}}} \tag{8.2.7}$$

where $\dot{E}_{\text{d},i}$ is the exergy destroyed in the ith equipment, which can be estimated for turbines, pumps, and heat exchangers according to Eqs. 8.2.8, 8.2.9, and 8.2.10, respectively. Eqs. 8.2.8, 8.2.9, and 8.2.10 are simplified versions of Eq. 7.1.3, considering that no heat is exchanged between the equipment and the environment. $\dot{E}_{\text{loss},i}$ is the exergy of the ith stream leaving the power cycle, which in this work is the cooling water stream exiting the condenser. The saturated liquid water exiting the boiler is used as the reactor cooling fluid, so it is a process constraint. Therefore, it is not regarded as exergy loss.

$$\dot{E}_{\text{d,turbine}} = \dot{E}_{\text{in}} - \dot{E}_{\text{out}} - \dot{W}_{\text{turbine}} \tag{8.2.8}$$

$$\dot{E}_{\text{d,pump}} = \dot{E}_{\text{in}} - \dot{E}_{\text{out}} + \dot{W}_{\text{pump}} \tag{8.2.9}$$

$$\dot{E}_{\text{d, heat exchanger}} = \sum_{j=1}^{\text{inlets}} \dot{E}_j - \sum_{k=1}^{\text{outlets}} \dot{E}_k \tag{8.2.10}$$

8.2.2 Power Cycle Thermodynamic Performance

From the power cycles simulations, their performances were assessed based on the First (η_{I}) and Second (η_{II}) Laws of thermodynamics. The results for both regular (ORC) and recuperative (RORC) configurations are depicted in Fig. 8.5 and Fig. 8.6 for η_{I} and η_{II}, respectively.

The highest efficiencies are obtained with either methanol or ethanol for ORC. That occurs due to two major reasons: Firstly, both are wet fluids and can be condensed at a lower pressure compared to the other fluids (0.4 bar against 1.3 bar on average). Therefore, they can be expanded to lower pressures in the turbine, which increases the power generation and, consequently, η_{I}; Secondly, they are superheated to avoid premature condensation inside the turbine whereas the dry fluids - in the ORC configuration, only - are limited to 5 K of superheating. Therefore, the boiler exergy destruction is much lower for wet fluids due to a better temperature match, which improves η_{II}.

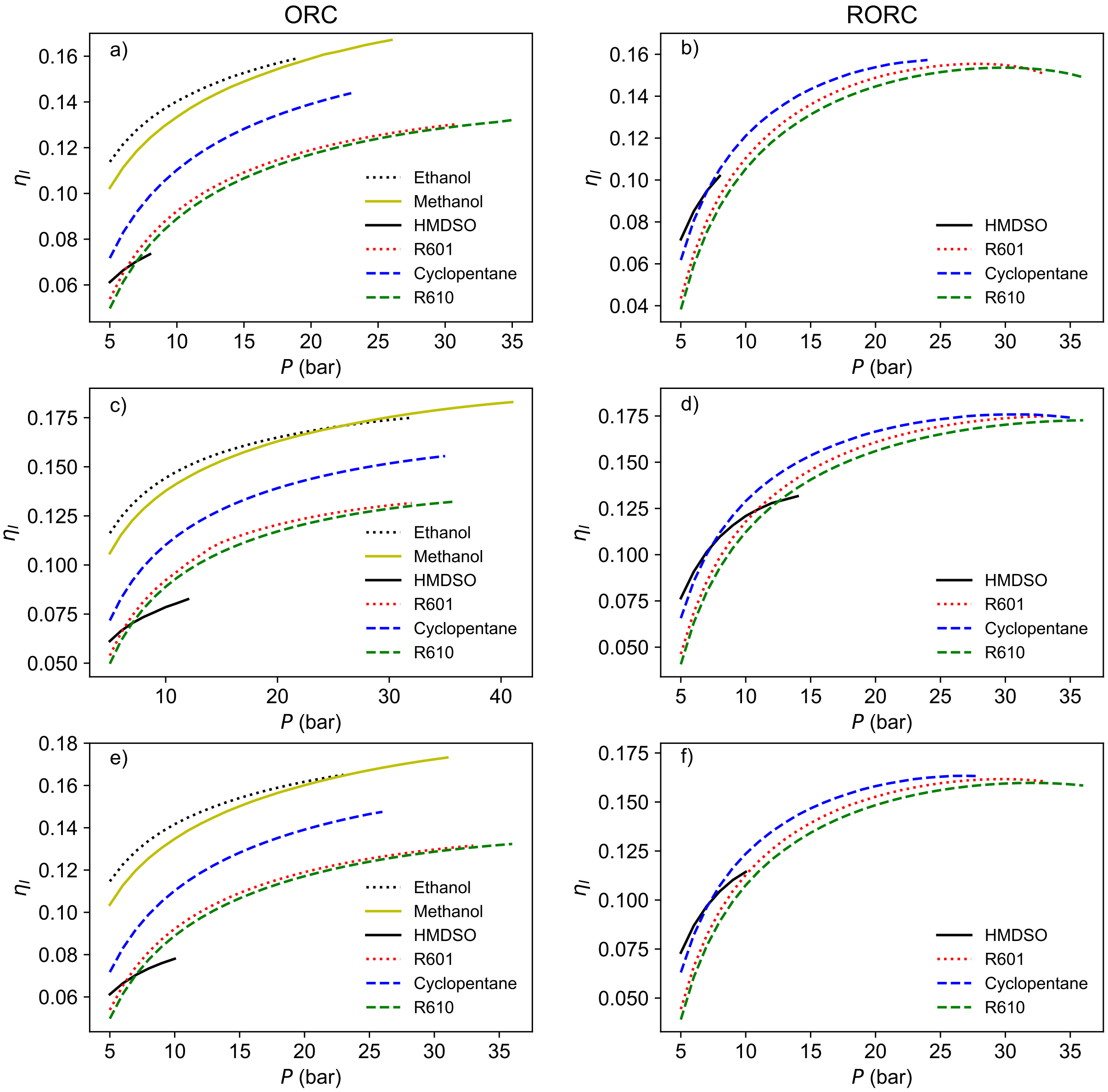

Figure 8.5: Power cycle First Law efficiency variation according to pump discharge pressure. Case OPT1: a) and b). Case OPT2: c) and d). Case OPT3: e) and f).

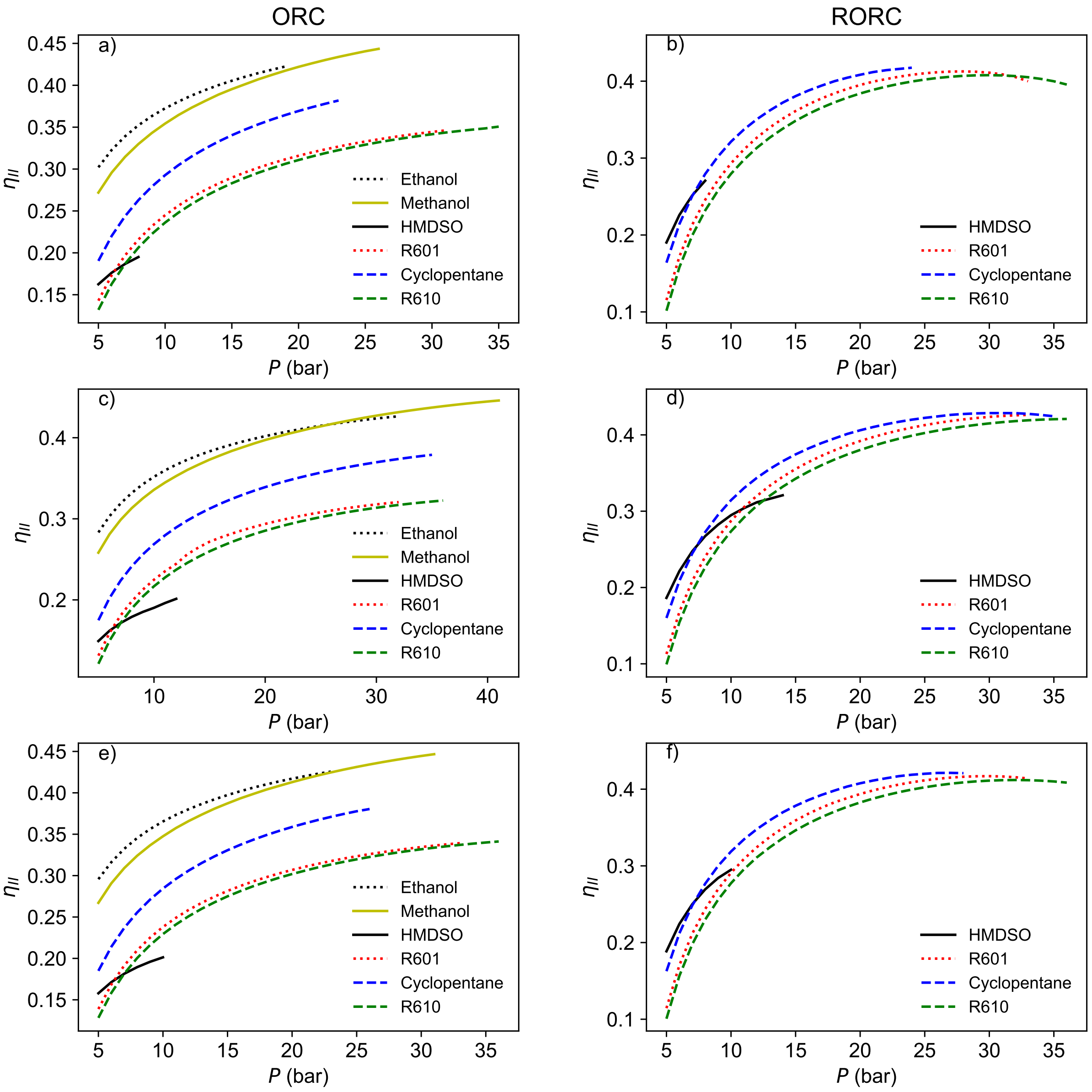

Figure 8.6: Power cycle Second Law efficiency variation according to pump discharge pressure. Case OPT1: a) and b). Case OPT2: c) and d). Case OPT3: e) and f).

The addition of a recuperator (RORC) drastically increases the power cycle efficiencies for dry fluids, which makes most of them competitive (compare Fig. 8.6 - a to b). Dry fluids are superheated at the turbine outlet and the recuperator is used to transfer this heat to the pressurized liquid from the pump exit. This considerably diminishes the amount of heat being wasted in the condenser. Nevertheless, as pointed out by Landelle et al. (2017), its positive effect is limited. Furthermore, it progressively decreases by increasing the pressure. That occurs because the degree of superheating at the turbine outlet decreases when the pressure increases for the same turbine inlet temperature. In addition, in Saleh et al. (2007)'s work, the recuperator improved the cycle performance by less than 1%, whereas in this work the improvement was on average approx. 15%. That occurred because the lower operation temperature (100 °C at the turbine inlet) led to a lower amount of heat to be recuperated. Therefore, the recuperator effect is limited, but tend to increase when the heat source temperature increases and the boiler pressure decreases.

Yu et al. (2016) have pointed out that, for latent heat sources, the fluid selection should be based only on its critical temperature (T_c). According to the authors, the fluid with the highest critical temperature would provide the highest power cycle efficiency. However, based on the results obtained in this work, this conclusion can be extended. Indeed, the performance of working fluids with the higher T_c was better, i.e., ethanol (T_c = 514 K), methanol (T_c = 513 K) and Cyclopentane (T_c = 511 K). However, HMDSO is the working fluid with the highest T_c (518 K) and had the worst performance. This led to a conclusion that not only critical temperature, but also critical pressure plays a vital role in selecting the most appropriate working fluid. HMDSO has the lowest critical pressure (19.1 bar) among all studied working fluids. Thus, for subcritical operation, it can not evaporate at elevated pressures. Lower pressure at turbine inlet means lower power generation and, consequently, lower efficiency.

From Fig. 8.5 and 8.6, both ethanol and methanol have similar performances and higher that the other fluids for the regular ORC. In the RORC configuration, the highest efficiency is achieved with Cyclopentane. In addition, the thermodynamic performance obtained with cyclopentane is comparable to that reported by Fierro et al., 2021 for recovering heat of a rotary kiln with the same working fluid.

By evaluating the equipment performance for the selected fluids in terms of exergy destruction (Tab. 8.3), it is noted that the greatest exergy destruction occurs in the boiler. That is due to the poor matching between the working fluid and the heat source temperature (Fig. 8.7). When the heat source is able to provide only sensible heat, the boiler exergy destruction is diminished by improving the temperature match either with transcritical operation or by means of different arrangements (Gleinser and Wieland, 2016). However, for latent heat sources, such changes have no effect because of the heat source constant temperature.

For cyclopentane in RORC configuration, exergy destruction in the boiler is much lower because the recuperator increases the working fluid inlet temperature, which improves the matching. However, the exergy once destructed in the boiler is now destructed in the recuperator. Therefore, the benefit of using a recuperator is limited to the reduced amount of heat that is rejected to the cooling water in the condenser.

Table 8.3: Equipment exergy destruction for ORC (Methanol and Ethanol) and RORC (Cyclopentane). Case OPT2 at 12 bar.

Working Fluid	Methanol	Ethanol	Cyclopentane
$\dot{E}x_{\text{d, boiler}}$ (kW)	186.14	175.98	136.39
$\dot{E}x_{\text{d, recuperator}}$ (kW)	-	-	68.07
$\dot{E}x_{\text{d, condenser}}$ (kW)	61.22	66.19	65.62
$\dot{E}x_{\text{d, pump}}$ (kW)	0.23	0.28	0.73
$\dot{E}x_{\text{d, turbine}}$ (kW)	72.49	70.33	54.02
$\dot{E}x_{\text{loss, cooling}}$ (kW)	26.09	25.92	26.20

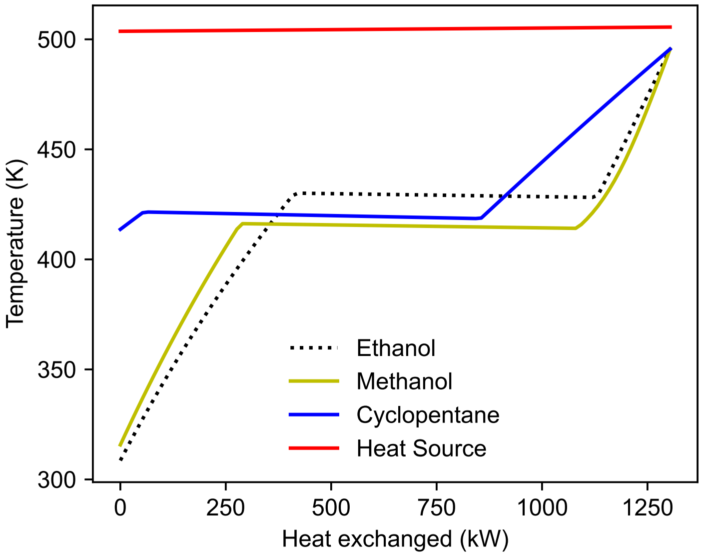

Figure 8.7: Boiler composite curve for a pump discharge pressure of 12 bar. Case OPT2.

8.2.3 Effect of the ds/dT Slope on RORC Performance

The power cycle η_{I} and η_{II} increase when the pump discharge pressure is increased for almost all working fluids. However, for some fluids in the recuperative configuration (RORC) there is an optimum, followed by a slight decrease, e.g., R601 and R610 in Fig. 8.5 -b).

Taking R610 saturation curve as example (Fig. 8.8), the optimum occurs when the slope ds/dT of the saturated vapor line is approx. 0 (30 bar in Fig. 8.5-b). By increasing the pump discharge pressure, increases the enthalpy change in the turbine ($\Delta H_{30\text{ bar}} > \Delta H_{25\text{ bar}}$) while d$s$/d$T$ is positive. When ds/dT becomes negative this trend changes, i.e., $\Delta H_{35\text{ bar}} <$

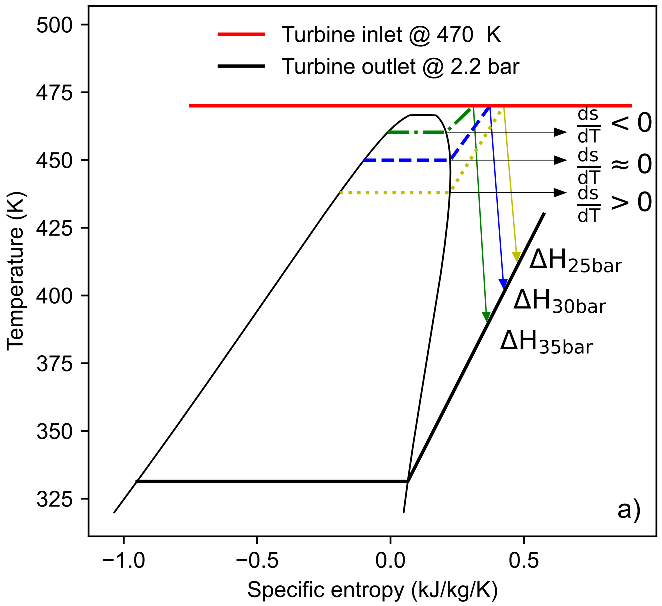

Figure 8.8: R610 saturation curve diagram. Different operating pressures for the same boiler heat load and working fluid exit temperature.

$\Delta H_{30\ \text{bar}}$. Consequently, since the boiler heat load is the same, a smaller value of η_{I} is obtained. This reverse behavior occurs from where ds/dT starts to become negative up to approx. 20 K above the working fluid T_c. In Fig. 8.5 -d, this behavior is not seen for R601 and R610 anymore. However, it appears for cyclopentane from 30 bar because ds/dT becomes negative. Therefore, by selecting working fluids with T_c up to 20 K below the heat source temperature, the best power cycle performance will be obtained when superheating starts where the slope ds/d$T \approx$ 0. This behavior is not seen in the usual ORC configuration because the superheated fluid exiting the turbine is directly cooled in the condenser without any heat recovery. For the ORC configuration, the higher the pump discharge pressure, the lower the amount of heat wasted in the condenser, thus, the higher the efficiency.

8.3 Power Cycle Economic Analysis

The Net Present Value (NPV) (Sec. 3.7) is used to assess the power cycle economic performance. To calculate the NPV, the cash flow (CF) must be known. However, some assumptions are made firstly:

- The electricity generated by the power cycle will be used elsewhere inside the chemical plat where it is supposed to be installed. Therefore, the income tax (IT) is set to be zero;

- Depreciation (D) is used in the cash flow to minimize taxation (Seider et al., 2003). Since IT is set to be zero, there is no need for estimating D and it is also set to be zero.

Therefore, Eq. 3.7.2 reduces to:

$$\mathrm{CF} = \mathrm{S} - \mathrm{TCI} - \mathrm{TCP} \tag{8.3.1}$$

The value obtained due to sales (S) is set to be equal to the value that would be paid if the generated electricity was purchased from the local grid, i.e., 0.0671 US\$ $\mathrm{kW^{-1}h^{-1}}$ (EIA, 2019).

To calculate the Total Capital Investment (TCI) (Eq. 8.3.2), the power plant Inside Battery Limits (ISBL) must be found. The ISBL is the summation of each equipment's bare module (Eq. 3.7.4) cost multiplied by an inflation factor, which is equal to 1.6045 (CEPCI from 2003 to February 2021) (Maxwell, 2021). Engineering (EC) and Contingency Cost (CC) are 20% and 10% of the ISBL, respectively. Start-up Cost is 2% of the summation among ISBL, EC, and CC. Outside Battery Limits (OSBL) cost was neglected since the power cycle is supposed to be install inside an existing chemical plant.

$$\mathrm{TCI} = \mathrm{ISBL} + \mathrm{EC} + \mathrm{CC} + \mathrm{SC} \tag{8.3.2}$$

The pump, turbine and heat exchangers (boiler, condenser, and recuperator) bare module cost are calculated according to Eq. 8.3.3 and Tab. 8.4 (Turton et al., 2012). Carbon steel is selected as the material of construction for all equipment because the fluids used in the power cycle are not corrosive.

$$C_{\mathrm{BM}} = 10^{(C1+C2\,\log_{10}(f_S))+C3[\log_{10}(f_S)]^2)}\left(f_{\mathrm{BM1}} + f_{\mathrm{BM2}} f_{\mathrm{m}} f_{\mathrm{P}}\right) \tag{8.3.3}$$

where f_P is the pressure factor, which is calculated according to Eq. 8.3.4 for heat exchangers if $P > 5$ barg, and for pumps if if $P > 10$ barg. Otherwise, it is equal 1. f_S is the size factor, which varies according to the equipment (Tab. 8.4).

$$\log_{10} f_P = f_{P1} + f_{P2}\log_{10} P + f_{P3}\left(\log_{10} P\right)^2 \tag{8.3.4}$$

Both $\dot{W}_{\mathrm{pump}}$ and $\dot{W}_{\mathrm{turbine}}$ (Tab. 8.4) are found during the power cycle simulation from Eqs. 8.2.1 and 8.2.2, respectively. However, the boiler, condenser and recuperator heat exchange area (A) are still unknown. The procedure to find A is somewhat more complex. Therefore, it is discussed separately in Section 8.3.1.

The Total Cost of Production is stipulated according to Eq. 8.3.5. The cost associated to the use of cooling water (C_{CW}) in the condenser is estimated according to Ulrich and

Table 8.4: Cost, pressure, material and bare module constants (Turton et al., 2012).

	Pump	Turbine	Heat exchanger
f_S	$\dot{W}_{\text{pump}}$ (kW)	$\dot{W}_{\text{turbine}}$ (kW)	A (m^2)
$C1$	3.4771	2.2476	4.8306
$C2$	0.135	1.4965	-0.8509
$C3$	0.1438	-0.1618	0.3187
f_{P1}	-0.245382	0	0.03881
f_{P2}	0.259016	0	-0.11272
f_{P3}	-0.01363	0	0.08183
f_m	1.5	1	1
f_{BM1}	1.89	3.63	1.63
f_{BM2}	1.35	0	1.66

Vasudevan (2006) (Appendix D.1). The labor cost (C_{L}) is estimated based on an annual average salary of US$ 45,000 (Payscale, 2021). Considering that the power cycle is remotely operated, 5 operators are required, taking into account shift rotation, allowance for holidays, vacations and weekends (Towler and Sinnott, 2012). Cost with benefits and training (C_{BT}) is set equal to 40% of C_{L}. Finally, the maintenance cost (C_{M}) is 4% of the ISBL.

$$\text{TCP} = C_{\text{CW}} + C_{\text{M}} + C_{\text{L}} + C_{\text{BT}} \tag{8.3.5}$$

The project lifetime is set to 25 years with 330 days of operation each year. According to Quoilin (2011),the risk of turbine blades corrosion for dry fluids due to condensation during expansion is much lower than for wet fluids. Therefore, turbine lifetime expectation for dry fluids is up to 30 years whereas for wet fluids it varies from 15 to 20 years. This is taken into account in the economic analysis by inserting a new turbine bare module cost in the cash flow at 17$^{\text{th}}$ year in case of working fluid condensation during expansion.

8.3.1 Heat Exchanger Area Calculation

The heat exchange area (A (m^2)) is found by the logarithmic mean temperature difference (ΔT_{LM} (K)) method (Eq. 8.3.6) (Smith, 2005). All calculations were performed in Python 3.8.6 and thermophysical properties were estimated using CoolProp 6.4.1 package (Bell et al., 2014).

$$\dot{Q} = UA\Delta T_{LM} \tag{8.3.6}$$

where U is the overall heat transfer coefficient (W·m^{-2}·K^{-1}).

To estimate A, the following assumptions are made:

1. The operation is in counter-current. Therefore, ΔT_{LM} can be calculated according to Eq. 8.3.7 (Bergman et al., 2011) ;

$$\Delta T_{LM} = \frac{\Delta T_1 - \Delta T_2}{\ln\left(\frac{\Delta T_1}{\Delta T_2}\right)} \tag{8.3.7}$$

$$\Delta T_1 = T_{\text{hot, in}} - T_{\text{cold, out}}$$

$$\Delta T_2 = T_{\text{hot, out}} - T_{\text{cold, in}}$$

2. All heat exchangers are of the Shell & Tubes (1-1) split-ring type with internal floating head. The floating head eases tube maintenance, replacement and cleaning. In addition, they can handle higher temperature differences than the fixed-tube type. Split-ring type requires a smaller shell-to-tube bundle clearance, which reduces the shell-side fluid bypass (Sinnott, 2005);

3. Both boiler and condenser are vertically-oriented. The heat transfer coefficient for vertical condensers are greater than for horizontal ones because the condensate is prevented from accumulating on the heat exchange surface both by fluid flow and by gravity (Kern, 1965). This diminishes the required exchanger area. Therefore, condensing fluids are assigned to flow downwards and boiling fluids upwards;

4. Tubes arrangement is 30° triangular and tube pitch is set equal to 1.25 times the tube external diameter. Triangular arrangement makes the shell-side fluid flow more turbulent, which, in turn, increases the heat transfer coefficient at the expense of a higher pressure drop. The assumed tube pitch is a value, which is normally used (Sinnott, 2005);

5. Baffle cut is set to the usual value of 25%. Optimal baffle spacing is usually between 0.3 and 0.5 times the shell internal diameter. Therefore, 0.4 is chosen in this work. For condensation in the shell-side, baffle spacing is higher, i.e., 1 (Sinnott, 2005).

6. Fluid allocation to either shell- or tube-side is made by following the guidelines presented by Seider et al. (2016) and Smith (2005):

    - Boiler: Condensing steam is assigned to the shell-side whereas working fluid flows inside the tubes. For most cases in this work, the working fluid pressure is higher than those of the steam;

- Condenser: Cooling water flows in the shell-side because it has a higher flowrate;
- Recuperator: Hotter fluid is assigned to the tube-side;

Both $\dot{Q}$ and ΔT_{LM} in Eq. 8.3.6 can be determined from the results obtained during the power cycle simulation. The overall heat transfer coefficient based on the tube external area is calculated according to Eq. 8.3.8 (Sinnott, 2005).

$$\frac{1}{U_{\mathrm{out}}} = \frac{1}{h_{\mathrm{out}}} + \frac{1}{f_{\mathrm{out}}} + \frac{d_{\mathrm{out}} \ln\left(\frac{d_{\mathrm{out}}}{d_{\mathrm{in}}}\right)}{2k_{\mathrm{w}}} + \frac{d_{\mathrm{out}}}{d_{\mathrm{in}} f_{\mathrm{in}}} + \frac{d_{\mathrm{out}}}{d_{\mathrm{in}} h_{\mathrm{in}}} \tag{8.3.8}$$

where the subscript "in" and "out" make reference to the tube interior and exterior, respectively. h is the fluid film coefficient (W·m^{-2}·K^{-1}), f is the fouling factor (W·m^{-2}·K^{-1}), d is the tube diameter (m), and k_{w} is the tube wall thermal conductivity, which is equal to 40 W·m^{-1}·K^{-1} for carbon steel (TEMA, 2007). The fouling factor varies according to the fluid. Values used in this work are presented in Table 8.5.

Table 8.5: Fouling factors (Sinnott, 2005).

Fluid	f (W·m^{-2}·K^{-1})
Steam	8,000
Cooling water	4,500
Organic evaporating	4,000
Organic condensing	5,000
Organic liquid or vapor	5,000

The correlations to estimate h are available in Appendix F along with the correlations used to estimate pressure drop. To use the appropriate correlation, it must be identified if phase change occurs within the heat exchanger. That is accomplished according to the procedure described in Fig. 8.9. An example of how the boiler is dived by applying the procedure in Fig. 8.9 is depicted in Fig 8.10. It can be seen that it shall be dived into 3 sections so that h can be properly estimated by the correct set of correlations. The calculations in each section will result in a corresponding A. The overall area is the summation of each section's area. The same is valid for the total pressure drop (ΔP).

Tube diameter is standardize. The diameters used for sizing the heat exchanger are shown in Table 8.6. To determine the internal diameter, the tube minimum thickness was estimated according to ASME (2013). To the found value, 0.5 mm was added as corrosion allowance. Then, with the external diameter and minimum thickness, the closest standard higher value for the internal diameter was selected from the manufacturer's list (ZP, 2021a). Although the tube length (L (m)) is also standardize (Table 8.7), it can also be manufacturer with a specified value upon request (ZP, 2021b). Therefore, to simplify the calculations, if the heat exchanger is divided into sections, to the first section a standardize value is assigned and the total number of tubes (N_t) is calculated (Eq. 8.3.9). To the subsequent sections, the tube length is determined by inserting the total number of tubes from the previous section into the same equation.

Table 8.6: Tube standard diameters (ZP, 2021a).

d_{out} (mm)	4.0	5.0	6.0	7.0	8.0	9.0	10.0	12.0	14.0	16.0	18.0	20.0	22.0
d_{in} (mm)	3.0	4.0	5.0	6.0	7.0	8.0	9.0	11.0	13.0	15.0	16.5	18.5	20.5

Table 8.7: Tube standard length (Sinnott, 2005).

L (m)	1.8288	2.4384	3.048	3.6576	4.8768	6.096	7.3152

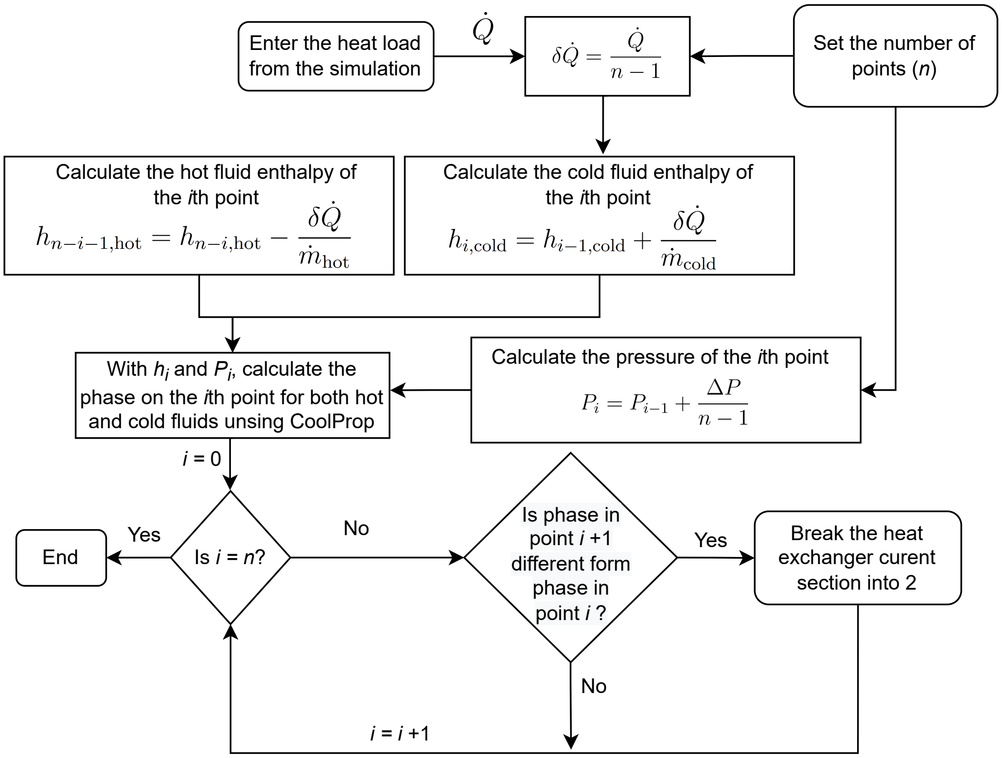

Figure 8.9: Procedure to identify phase change inside the heat exchangers.

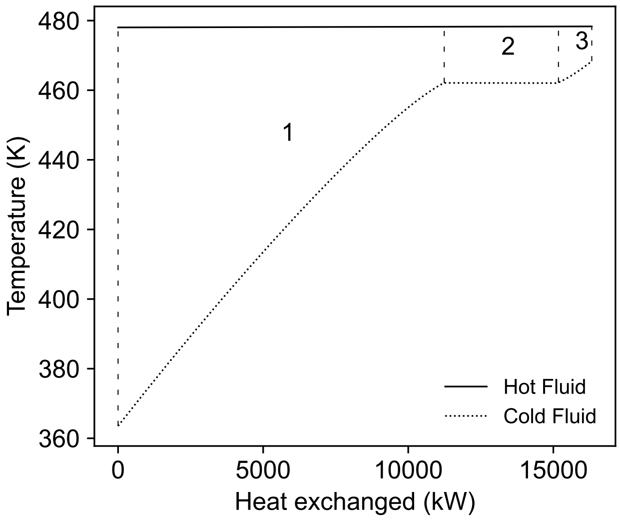

Figure 8.10: Boiler division into sections for film coefficient estimation.

$$N_t = \frac{\pi d_{\text{out}} L}{A} \tag{8.3.9}$$

In this work, the iterative procedure described by Ref. Sinnott, 2005 is adapted and used to calculate both A and ΔP (Fig. 8.11).

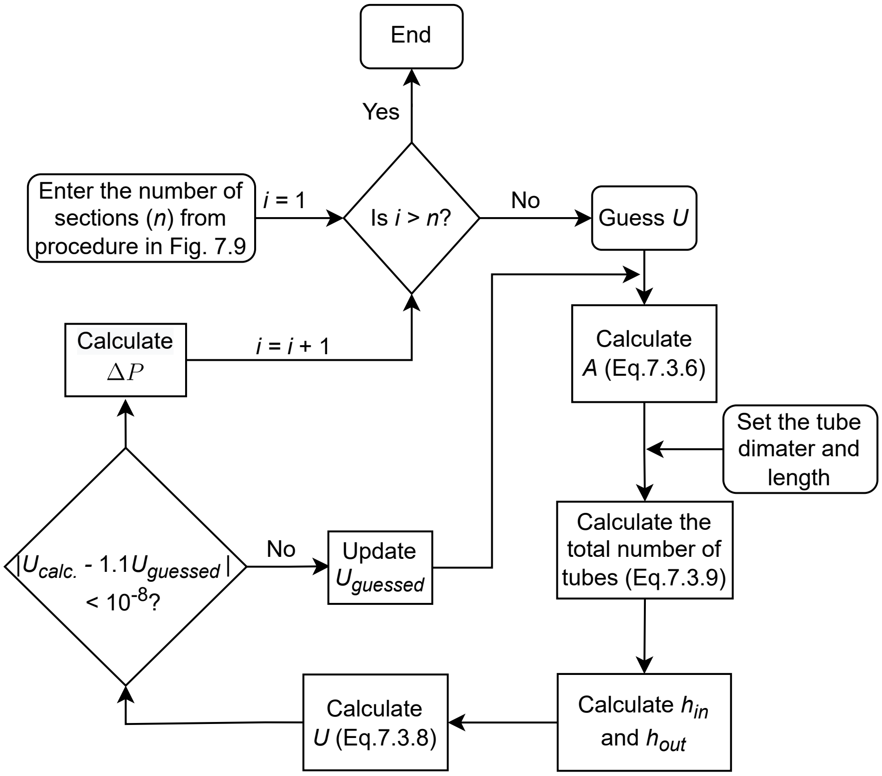

Figure 8.11: Heat exchanger design procedure. Adapted from Sinnott (2005).

The function *fsolve* from the Scipy v1.6.2 optimizer package is used to calculate U. In addition, as a safety measure, the procedure was set to stop if $U_{\text{calculated}}$ is 10% greater than the guessed value. Finally, the aforementioned procedure is performed for each tube diameter and each tube length. The chosen case will be the one with the smallest area and with a pressure drop equal or smaller assumption #5 in Subsec. 8.2.1.

8.3.2 Power Cycles Economic Performance

Methanol and ethanol in the usual configuration (ORC), and Cyclopentane in the recuperative configuration (RORC) yielded higher efficiencies during the thermodynamic performance assessment. Therefore, the economic analysis was carried out for those working fluids. In addition, the results presented in this subsection refers to Case OPT1. Despite the similarities between the efficiencies obtained for each case, power generation capacity has proved to play a major role in the power cycle economic feasibility.

For Case OPT2 and OPT3, by carrying out a preliminary evaluation, it was found that both cases result in unfeasible economic scenarios. The reason is due to the lower power production and mostly to the elevated labor cost. For example, the maximum power production is obtained with methanol for case OPT2 (Fig. 8.5 -b), which is equal to 238.5 kW. Considering the electricity cost of US$ 0.0671 per kW·h, it would be obtained US$ 126,700 yearly as revenue. However, the expense with salary is US$ 225,000 yearly. Therefore, such power cycle is unfeasible. Despite the higher power generation capacity (820 kW on average), a similar result is obtained for Case OPT3 because the revenue is still smaller than the operational expenses. Feasible ORCs with a lower power generation capacity (less than 50 kW) have been reported in the literature (Casci et al., 1981; Nguyen et al., 2001; Peris et al., 2015). Their feasibility, however, is attributed to its modularity. Such power cycles are manufactured on demand and delivered as plug-and-play units. Therefore, costs with engineering for on-site construction and personnel for operation are usually negligible, which make them feasible at such small scale. In addition, electricity price assumed in such evaluations are usually higher than the US$ 0.0671 per kW·h considered in this work.

According to Imran et al. (2014), the boiler pressure is the most influential variable on the power cycle capital cost. Therefore, for each working fluid, 3 different pump discharge pressures were selected, starting from the one where the highest η_{I} was obtained (Tab. 8.8). The boiler heat load is constant and equal to 16.42 MW.

Table 8.8: Selected scenarios simulation results.

	Methanol			Ethanol			Cyclopentane		
P (bar)	26	21	16	19	14	9	24	19	14
$\dot{W}_{\text{turbine}}$ (kW)	2,794	2,676	2,512	2,655	2,506	2,267	2,711	2,604	2,377
$\dot{W}_{\text{pump}}$ (kW)	50	39	29	42	30	19	128	101	75
$\dot{Q}_{\text{condenser}}$ (MW)	13.68	13.78	13.94	13.81	13.95	16.42	13.84	13.92	14.12
$\dot{Q}_{\text{recuperator}}$ (kW)	-	-	-	-	-	-	4,068	4,839	5,680

The NPV was calculated for each scenario for a rate of return varying from 1% to 15%. The results are depicted in Fig. 8.12. Despite the negative effect of the operating pressure on the equipment cost, it is promptly noted that the higher the pressure, the higher the NPV for all fluids. That occurs because more power is generated when the pressure increases, which is sufficient to pay off the equipment capital cost rise.

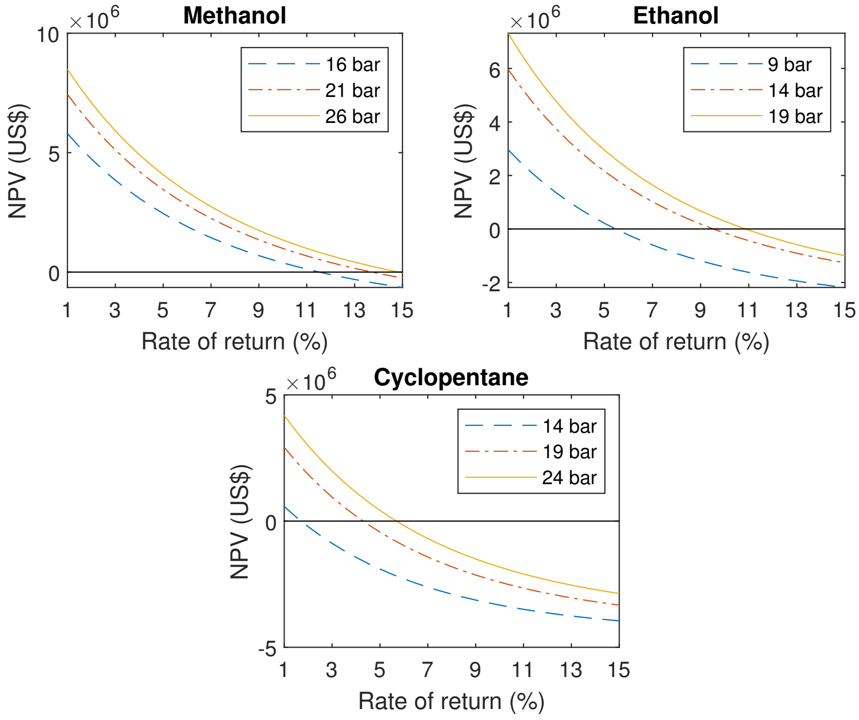

Figure 8.12: NPV *versus* rate of return at different pump discharge pressures.

The best economic performance was achieved with methanol with internal rates of return (rate of return when NPV equals zero) varying from 12% to 14.5%. The worst one was with cyclopentane. Despite the similar net power generation between cyclopentane and ethanol, the additional recuperator capital cost has led the power cycle with cyclopentane to present the worst economic performance. The power cycle cost summary for the best case of each working fluid is shown in Tab. 8.9.

The turbine is the most expensive equipment followed by the condenser. As a matter of fact, the condenser is twice as expensive as the boiler. That occurs due to the lower ΔT_{LM} in the condenser. In addition, ethanol condenser is the most expensive compared to the other fluids. At the turbine outlet, ethanol is still superheated and the overall heat transfer coefficient obtained for cooling ethanol until its condensation temperature is low. Thus, a greater heat exchange area is required. Similarly, in the recuperator, the hot fluid is cooled until its condenses whereas the cold fluid does not change phase. The design variables are available in Tabs. 8.10, 8.11 and 8.12 for condenser, boiler and recuperator, respectively.

Table 8.9: Power cycle cost summary for the best case of each working fluid.

Equipment	Methanol	Ethanol	Cyclopentane
Turbine $\times 10^{-6}$ (US\$)	1.77 (57%)	1.74 (47%)	1.75 (37%)
Pump $\times 10^{-6}$ (US\$)	0.09 (3%)	0.08 (2%)	0.17 (3%)
Boiler $\times 10^{-6}$ (US\$)	0.42 (13%)	0.43 (12%)	0.55 (11%)
Condenser $\times 10^{-6}$ (US\$)	0.85 (27%)	1.42 (39%)	1.25 (25%)
Recuperator $\times 10^{-6}$ (US\$)	-	-	1.22 (24%)
Total $\times 10^{-6}$ (US\$)	3.13 (100%)	3.67 (100%)	4.94 (100%)

The cumulative cash flow was plotted against the project lifetime (Fig. 8.13) for the best case of each working fluid. The total capital investment was US\$ 4.16 million for methanol, US\$ 4.86 million for ethanol and US\$ 6.57 million for cyclopentane (Year 1 in Fig. 8.13). From Fig. 8.13 it is also possible to see that the pay-back period is 7, 10 and 14 years for methanol, ethanol and cyclopentane, respectively. The cumulative cash flow for methanol drops from the 16th to 17th year. That occurs because methanol partially condenses during expansion inside the turbine. According to Quoilin (2011), this diminishes the turbine lifespan, which was set as 17 years if condensation occurs. The cumulative cash flow drop is caused by the capital cost of a new turbine.

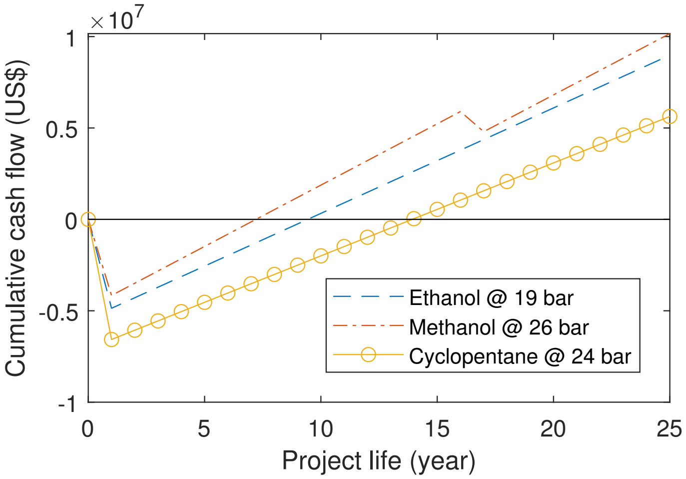

Figure 8.13: Cumulative cash flow *versus* project lifetime.

Finally, methanol is chosen as the most prominent fluid for heat recovery of latent heat sources in the temperature range of 200 - 230 °C (473 - 500 K) due to the best thermodynamic and economic performance obtained by using this working fluid. However, it is advisable to carry out laboratory trials not only to assess the working fluid thermal stability throughout the cycle but also to obtain a final validation of the power cycle thermodynamic performance.

Table 8.10: Condenser design parameters for the best scenario of each working fluid.

Zone	Parameter	Methanol	Ethanol	Cyclopentane
Cooling	d_{out} (mm)	-	8.00	-
	L_{tube} (m)	-	0.74	-
	A (m^2)	-	322	-
	U (W·m^{-2}·K^{-1})	-	49	-
	ΔT_{LM} (K)	-	13	-
	$\dot{Q}$ (MW)	-	0.21	-
Condensing	d_{out} (mm)	9.00	8.00	10.00
	L_{tube} (m)	3.66	3.66	4.88
	A (m^2)	1,157	1,598	1,700
	U (W·m^{-2}·K^{-1})	871	823	733
	ΔT_{LM} (K)	14	10	11
	$\dot{Q}$ (MW)	13.68	13.6	13.84

Table 8.11: Boiler design parameters for the best scenario of each working fluid.

Zone	Parameter	Methanol	Ethanol	Cyclopentane
Preheating	d_{out} (mm)	8.00	9.00	9.00
	L_{tube} (m)	2.44	3.66	4.88
	A (m^2)	187	267	348
	U (W·m^{-2}·K^{-1})	415	337	527
	ΔT_{LM} (K)	73	76	45
	$\dot{Q}$ (MW)	5.70	6.85	8.25
Boiling	d_{out} (mm)	8.00	9.00	9.00
	L_{tube} (m)	2.74	2.68	4.58
	A (m^2)	211	196	326
	U (W·m^{-2}·K^{-1})	1,652	1,666	1,637
	ΔT_{LM} (K)	27	27	14
	$\dot{Q}$ (MW)	9.41	8.83	7.68
Superheating	d_{out} (mm)	8.00	9.00	9.00
	L_{tube} (m)	1.88	1.3	0.72
	A (m^2)	144	95	51
	U (W·m^{-2}·K^{-1})	521.4	452	773
	ΔT_{LM} (K)	18	17	13
	$\dot{Q}$ (MW)	1.32	0.74	0.50

Table 8.12: Recuperator design parameters for the best scenario with cyclopentane.

Zone	Parameter	Cyclopentane
Cooling/Heating	d_{out} (mm)	14.00
	L_{tube} (m)	7.17
	A (m^2)	1,178
	U (W·m^{-2}·K^{-1})	173
	ΔT_{LM} (K)	17
	$\dot{Q}$ (MW)	3.54
Condensing/Heating	d_{out} (mm)	14.00
	L_{tube} (m)	2.44
	A (m^2)	401
	U (W·m^{-2}·K^{-1})	103
	ΔT_{LM} (K)	13
	$\dot{Q}$ (MW)	0.53

Chapter 9

Conclusions

In this part of the work, the usual (ORC) and the regenerative (RORC) organic Rankine cycle configurations were studied using different working fluids. The goal was to evaluate the feasibility of using such power cycles to transform the heat released by an exothermic reaction at a low temperature (473 - 500 K) into a more useful form of energy, i.e., electricity. The evaluation was carried out for the 3 different scenarios from Part I, namely, OPT1, OPT2 and OPT3.

From a wide range of different available working fluids, 6 were selected to be used in the simulations based on their critical temperature and pressure and on safety and environmental aspects. The power cycle was modeled in Python 3.8.10 and the thermophysical properties were estimated by the CoolProp 6.4.1 package. From the simulations results, the wet fluids, i.e., methanol and ethanol, have shown the best thermodynamic performance measured by the First (η_{I}) and the Second (η_{II}) law efficiencies. The dry fluids (*n*-pentane, dimethyl-ether, hexamethyldisiloxane and cyclopentane) have shown a poor performance in the ORC configuration, but with the addition of a recuperator (RORC), the performance considerably improved (15% increase on average), which made most of them competitive with the wet fluids. Despite the limited recuperator effect on the cycle's performance, the improvement caused by its use was found to increase as the heat source temperature increase and the evaporation pressure decreases.

The pump discharge pressure has also a positive effect on both η_{I} and η_{II}. However, for some dry working fluids in the RORC configuration there is a maximum after which any increase in the pump discharge pressure cause a slight efficiency decrease. This trend inversion is observed when superheating starts where the slope $\mathrm{d}s/\mathrm{d}T$ of the saturated vapor line becomes negative and extends for a heat source temperature up to 20 K above the working fluid critical temperature. Therefore, by selecting working fluids with T_c up to 20 K below the heat source temperature, the best power cycle performance will be obtained when superheating starts where the slope $\mathrm{d}s/\mathrm{d}T \approx 0$.

The highest exergy destruction occurs in the boiler. When only sensible heat is available, transcritical operation or the use of different power cycles arrangements usually improve the temperature match in the boiler, thus, the exergy destruction decreases. For latent heat sources, the temperature is almost constant so that none of the aforementioned changes would improve the scenario. For such heat sources, the lowest exergy destruction rate occurs when the working fluid is able to evaporate at a temperature as close as possible of the heat source's temperature and possesses the highest latent heat at the evaporation temperature.

After the thermodynamic evaluation, three different fluids were selected for the economic analysis, i.e., methanol (ORC), ethanol (ORC) and cyclopentane (RORC). For the scenarios OPT2 and OPT3, a preliminary analysis has demonstrated that it is not feasible to use the power cycles for electricity generation. The lower power generation capacity combined with high operational expenses render the power cycle unfeasible for such scenarios. For case OPT1, however, feasiablity was obtained for all 3 working fluids, even at low operating pressures, depending on the rate of return. The most profitable power cycle was ORC operating with methanol as working fluid at the highest pressure. For this working fluid, the internal rate of return varied from 12% to 14.5% with a pay-back period of 7 years. Although the cycles running with ethanol and cyclopentane have very similar net power generation capacity, the recuperator additional capital cost has led the one with cyclopentane to the show the worst economic performance.

References

Al-Janabi, Abdullah, Ghassan Al-Hajri, and Tariq Al-Maashani (2021). “Investigate the technical-economical feasibility of utilizing the available industrial waste thermal energy in Oman”. In: *Thermal Science and Engineering Progress* 21. DOI: 10.1016/j.tsep.2020.100778, p. 100778.

ASME (2013). *Boiler & Pressure Vessel Code. VIII Rules for Construction of Pressure vessels.* American Society of Mechanical Engineers.

Badr, O., S. D. Probert, and P. W. O’callaghan (1985). “Selecting a working fluid for a Rankine-cycle engine”. In: *Applied Energy* 21.1. DOI: 10.1016/0306-2619(85)90072-8, pp. 1–42.

Bao, J. and L. Zhao (2013). “A review of working fluid and expander selections for organic Rankine cycle”. In: *Renewable and sustainable energy reviews* 24. DOI: 10.1016/j.rser.2013.03.040, pp. 325–342.

Bell, Ian H. et al. (2014). “Pure and Pseudo-pure Fluid Thermophysical Property Evaluation and the Open-Source Thermophysical Property Library CoolProp”. In: *Industrial & Engineering Chemistry Research* 53.6. DOI: 10.1016/j.ijhydene.2008.08.039, pp. 2498–2508.

Bergman, Theodore L. et al. (2011). *Introduction to heat transfer.* Sixth Ed. John Wiley & Sons.

Braimakis, Konstantinos and Sotirios Karellas (2018). “Energetic optimization of regenerative Organic Rankine Cycle (ORC) configurations”. In: *Energy Conversion and Management* 159. DOI: 10.1016/j.enconman.2017.12.093, pp. 353–370.

Casci, Corrado et al. (1981). “Heat recovery in a ceramic kiln with an organic Rankine cycle engine”. In: *Journal of Heat Recovery Systems* 1.2. DOI: 10.1016/0198-7593(81)90027-8, pp. 125–131.

Çengel, Yunus A.. and Michael A. Boles (2007). *Thermodynamics: An Engineering Approach.* McGraw-Hill Higher Education.

Chevron-Phillips (2018). *Cyclopentane - Material Safety Data Sheet.* `http://www.cpchem.com/msds/100000014138_SDS_US_EN.PDF`. (accessed 21 August 2019).

Drescher, Ulli and Dieter Brüggemann (2007). “Fluid selection for the Organic Rankine Cycle (ORC) in biomass power and heat plants”. In: *Applied thermal engineering* 27.1. DOI: 10.1016/j.applthermaleng.2006.04.024, pp. 223–228.

EIA (2019). *Average Price of Electricity to Ultimate Customers by End-Use Sector*. `https://www.eia.gov/electricity/monthly/epm_table_grapher.php?t=epmt_5_6_a`. (accessed 26 August 2019).

Feng, Huijun et al. (2020). “Power and efficiency optimizations of an irreversible regenerative organic Rankine cycle”. In: *Energy Conversion and Management* 220. DOI: 10.1016/j.enconman.2020. p. 113079.

Fierro, José J et al. (2021). “Techno-economic assessment of a rotary kiln shell radiation waste heat recovery system”. In: *Thermal Science and Engineering Progress* 23. DOI: 10.1016/j.tsep.2021.100858, p. 100858.

Fisher (2009). *Hexamethyldisiloxane - Material Safety Data Sheet*. `https://www.fishersci.com/store/msds?partNumber=AC194790100&productDescription=HEXAMETHYLDISILOXANE+98+10ML&vendorId=VN00032119&countryCode=US&language=en`. (accessed 15th July 2021).

— (2014). *Ethanol - Material Safety Data Sheet*. `https://beta-static.fishersci.com/content/dam/fishersci/en_US/documents/programs/education/regulatory-documents/sds/chemicals/chemicals-e/S25309.pdf`. (accessed 21 August 2019).

— (2015a). *Methanol - Material Safety Data Sheet*. `https://beta-static.fishersci.com/content/dam/fishersci/en_US/documents/programs/education/regulatory-documents/sds/chemicals/chemicals-m/S25426A.pdf`. (accessed 21 August 2019).

— (2015b). *Pentane - Material Safety Data Sheet*. `https://beta-static.fishersci.com/content/dam/fishersci/en_US/documents/programs/education/regulatory-documents/sds/chemicals/chemicals-p/S25457.pdf`. (accessed 21 August 2019).

Gleinser, Moritz and Christoph Wieland (2016). “The misselhorn cycle: batch-evaporation process for efficient low-temperature waste heat recovery”. In: *Energies* 9.5. DOI: 10.3390/en9050337, p. 337.

Imran, Muhammad et al. (2014). “Thermo-economic optimization of Regenerative Organic Rankine Cycle for waste heat recovery applications”. In: *Energy Conversion and Management* 87. DOI: 10.1016/j.enconman.2014.06.091, pp. 107–118.

Kern, Donald Quentin (1965). *Process heat transfer*. International Ed. McGraw-Hill New York.

Landelle, Arnaud et al. (2017). “Organic Rankine cycle design and performance comparison based on experimental database”. In: *Applied energy* 204. DOI: 10.1016/j.apenergy.2017.04.012, pp. 1172–1187.

Lee, Ho Yong and Kyoung Hoon Kim (2015). "Energy and exergy analyses of a combined power cycle using the organic rankine cycle and the cold energy of liquefied natural gas". In: *Entropy* 17.9. DOI: 10.3390/e17096412, pp. 6412–6432.

Liu, Bo-Tau, Kuo-Hsiang Chien, and Chi-Chuan Wang (2004). "Effect of working fluids on organic Rankine cycle for waste heat recovery". In: *Energy* 29.8. DOI: 10.1016/j.energy.2004.01.004, pp. 1207–1217.

Mago, Pedro J et al. (2008). "An examination of regenerative organic Rankine cycles using dry fluids". In: *Applied thermal engineering* 28.8-9. DOI: 10.1016/j.applthermaleng.2007.06.025, pp. 998–1007.

Maizza, V. and A. Maizza (2001). "Unconventional working fluids in organic Rankine-cycles for waste energy recovery systems". In: *Applied thermal engineering* 21.3. DOI: 10.1016/S1359-4311(00)00044-2, pp. 381–390.

Maxwell, Charles (2021). *Cost Indices.* `https://www.toweringskills.com/financial-analysis/cost-indices/`. (accessed 24 June 2021).

Moran, Michael J et al. (2011). *Fundamentals of engineering thermodynamics.* Seventh Edition. John Wiley & Sons.

Muhammad, Usman et al. (2015). "Design and experimental investigation of a 1 kW organic Rankine cycle system using R245fa as working fluid for low-grade waste heat recovery from steam". In: *Energy Conversion and Management* 103. DOI: 10.1016/j.enconman.2015.07.045, pp. 1089–1100.

Nguyen, TQ, JD Slawnwhite, and K Goni Boulama (2010). "Power generation from residual industrial heat". In: *Energy Conversion and Management* 51.11. DOI: 10.1016/j.enconman.2010.03.016, pp. 2220–2229.

Nguyen, V. M., P. S. Doherty, and S. B. Riffat (2001). "Development of a prototype low-temperature Rankine cycle electricity generation system". In: *Applied Thermal Engineering* 21.2. DOI: 10.1016/S1359-4311(00)00052-1, pp. 169–181.

Payscale (2021). *Average Process Technician Hourly Pay.* `https://www.payscale.com/research/US/Job=Process_Technician/Hourly_Rate`. (accessed 24 June 2021).

Peris, Bernardo et al. (2015). "Experimental study of an ORC (organic Rankine cycle) for low grade waste heat recovery in a ceramic industry". In: *Energy* 85. DOI: 10.1016/j.energy.2015.03.065, pp. 534–542.

Pili, Roberto et al. (2017). "Techno-economic analysis of waste heat recovery with ORC from fluctuating industrial sources". In: *Energy Procedia* 129. DOI: 10.1016/j.egypro.2017.09.170, pp. 503–510.

Quoilin, Sylvain (2011). “Sustainable Energy Conversion Through the Use of Organic Rankine Cycles for Waste Heat Recovery and Solar Applications”. PhD thesis. Aerospace and Mechanical Engineering Department. University of Liegè. Belgium.

Saleh, Bahaa et al. (2007). “Working fluids for low-temperature organic Rankine cycles”. In: *Energy* 32.7. DOI: 10.1016/j.energy.2006.07.001, pp. 1210–1221.

Scaccabarozzi, Roberto et al. (2018). “Comparison of working fluids and cycle optimization for heat recovery ORCs from large internal combustion engines”. In: *Energy* 158. DOI: 10.1016/j.energy.2018.06.017, pp. 396–416.

Seider, Warren D., J.D. Seader, and Daniel R. Lewin (2003). *Product and Process Design Principles.* second ed. John Wiley & Sons, New York.

Seider, Warren D. et al. (2016). *Product and Process Design Principles: Synthesis Analysis and Evaluation.* fourth ed. John Wiley & Sons, New York.

Sigma-Aldrich (2015). *Diethylether - Material Safety Data Sheet.* `http://dept.harpercollege.edu/chemistry/sds/Diethyl%20ether.pdf`. (accessed 21 August 2019).

Sinnott, Raymond K. (2005). *Chemical engineering design.* Vol. 6. Coulson & Richardson’s Chemical Engineering. Elsevier Butterworth-Heinemann Oxford.

Smith, Robin (2005). *Chemical process: design and integration.* John Wiley & Sons.

Sun, Jian and Wenhua Li (2011). “Operation Optimization Of An Organic Rankine Cycle (orc) Heat Recovery Power Plant”. In: *Applied Thermal Engineering* 31.11-12. DOI: 10.1016/j.applthermaleng.2011.03.012, pp. 2032–2041.

Sun, Qingxuan et al. (2020). “Thermodynamic and economic optimization of a double-pressure organic Rankine cycle driven by low-temperature heat source”. In: *Renewable Energy* 147. DOI: 10.1016/j.renene.2018.11.093, pp. 2822–2832.

Tchanche, Bertrand Fankam et al. (2009). “Fluid selection for a low-temperature solar organic Rankine cycle”. In: *Applied Thermal Engineering* 29.11-12. DOI: 10.1016/j.applthermaleng.2008.12.025, pp. 2468–2476.

TEMA (2007). *Standards of the tubular exchanger manufacturers association.* Ninth Ed. Tubular exchanger manufacturers association Inc.

Tian, Zhen et al. (2020). “Thermo-economic analysis and optimization of a combined Organic Rankine Cycle (ORC) system with LNG cold energy and waste heat recovery of dual-fuel marine engine”. In: *International Journal of Energy Research* 44.13. DOI: 10.1002/er.5529, pp. 9974–9994.

Towler, Gavin and Raymond K Sinnott (2012). *Chemical engineering design: principles, practice and economics of plant and process design.* second ed. Elsevier, New York.

Turton, Richard et al. (2012). *Analysis, synthesis and design of chemical processes.* fourth ed. Pearson Education, New York.

Ulrich, G. D. and P. T. Vasudevan (2006). “How to estimate utility costs”. In: *Chemical Engineering* 113.4, p. 66.

Vélez, Fredy et al. (2012). “A technical, economical and market review of organic Rankine cycles for the conversion of low-grade heat for power generation”. In: *Renewable and Sustainable Energy Reviews* 16.6. DOI: 10.1016/j.rser.2012.03.022, pp. 4175–4189.

Wang, Huarong et al. (2015). “Organic Rankine cycle saves energy and reduces gas emissions for cement production”. In: *Energy* 86. DOI: 10.1016/j.energy.2015.03.112, pp. 59–73.

Wei, Donghong et al. (2007). “Performance analysis and optimization of organic Rankine cycle (ORC) for waste heat recovery”. In: *Energy conversion and Management* 48.4. DOI: 10.1016/j.enconman.2006.10.020, pp. 1113–1119.

Wolpert, JL and SB Riffat (1996). “Solar-powered Rankine system for domestic applications”. In: *Applied Thermal Engineering* 16.4. DOI: 10.1016/1359-4311(95)00032-1, pp. 281–289.

Yamamoto, Takahisa et al. (2001). “Design and testing of the organic Rankine cycle”. In: *Energy* 26.3. DOI: 10.1016/S0360-5442(00)00063-3, pp. 239–251.

Yu, Haoshui, Xiao Feng, and Yufei Wang (2016). “Working fluid selection for organic Rankine cycle (ORC) considering the characteristics of waste heat sources”. In: *Industrial & Engineering Chemistry Research* 55.5. DOI: 10.1021/acs.iecr.5b02277, pp. 1309–1321.

ZP (2021a). *Dimensions and weights of seamless tubes.* `https://www.steeltube.sk/zelpo/vyrobky.nsf/Tab5UK?OpenPage`. (accessed 15th July 2021).

— (2021b). *Seamless tubes for heat exchangers.* `https://www.steeltube.sk/for-heat-exchangers/`. (accessed 15th July 2021).

Part III

Closure

Chapter 10

Conclusions

In this work, the possibility of using the heat released by th WGSR to generate electricity for the chemical plant and also replace the usual HTSR-LTSR configuration by one single multitubular reactor with integrated heat exchange was evaluated.

To simulate the new reactor, a surrogate model was proposed to estimate the catalyst effectiveness factor. That was an alternative that improved simulations time because of the almost instantaneous effectiveness factor availability. In addition, non-ideal gas behavior was considered by PRSV-EoS. Most studies found in literature assume ideal gas behavior despite the elevated reactor operational pressure between 25 and 30 bar. After optimization, which were conducted considering PRSV-EoS, the optimized designs were simulated, but considering ideal gas behavior. The results indicated that it is plausible to assume ideal gas behavior for all three cases due to similar results obtained in comparison to the ones with PRSV-EoS. Also, the simulations are accomplished at least twice faster when ideal gas behavior is assumed. Therefore, assuming ideal gas behavior could improve the time spent to optimize each scenario, which were over a month. Regarding this matter, it is important to emphasize that the DIRECT algorithm, which was used to carry out the optimizations, suffers from the optimization problem dimension, i.e., the higher the number of decisions variables, the longer it will take to converge to the final solution. Considering that DIRECT has been proved to converge to a global optimum, even for objective functions with hundreds of local minima, it is advised to change the programming language to perform the optimization. In this work MATLAB® was used mostly because it has excellent features for solving differential equations. However, it has a slower performance when compared to C or Java, for example.

Despite the long time spent in the optimization, the reactor model developed with PRSV-EoS was validated and shall be useful in situations where ideal gas behavior is not a valid assumption. Furthermore, it is not limited to the WGSR, but it can be applied to any other gaseous systems or at least serve as a basis provided that pertinent adaptions related to the components are made.

The heat released by the reactor was used to generate saturated steam, which was then used in the power cycle's boiler as heat source. The power cycles were modeled in Python, mostly because of the thermophysical properties package CoolProp. From the thermodynamic analysis, to recover heat from almost constant temperature heat sources, it was observed that fluids with a wider $T \times s$ curve shape yield better efficiencies, which was the case for methanol and ethanol. That occurs because, considering that a poor temperature match between the primary energy source and the working fluid leads to a poor cycle performance due to a higher exergy destruction, better cycle performances are attained by working fluids with a higher vaporization heat, leaving the boiler as close as possible to the saturated vapor state. In terms of economic performance, only one of the 3 cases under consideration is feasible. However, it is import to bear in mind that such results are somewhat subjective and the final outcome depends utmost on the assumptions made for carrying out the economic assessment. Mostly on the operational cost and the electricity price. Furthermore, economic assessments changes throughout time and feasibility may be achieved in the future with further technology development and market demand. The built model, however, stands and shall be used for future analysis.

10.1 Suggestions for Future Work

- The surrogate model for the effectiveness factor prediction has shown good results in this work. However, an improvement can be made by applying machine learning techniques. The surrogate model is limited to be applied only within the range used to estimate its parameters. With well-trained machine learning models that drawback can be overcame and the model can serve for a wide range of different conditions;

- Replace water by the power cycle's working fluid so that the reactor can be the power cycle's boiler. Take into account the safety aspects related to this change. The elimination of water as intermediate might improve the power cycle's efficiency because of the heat source's temperature increase, which in this new scenario is the reacting gases mixture inside the reactors' tubes. Following the water replacement by the working fluid, a combined dynamic simulation, i.e., reactor and power cycle, can also be carried out so that the stability of such system can be evaluated, e.g., how a sudden temperature decrease inside the reactor affects the power cycle performance or how a failure in the cooling fluid/working fluid circulation affects the reactor. Afterwards, perform lab scale experiments to validate the system's performance can also be done.

References

Adams II, T. A. and P. I. Barton (2009). “A dynamic two-dimensional heterogeneous model for water gas shift reactors”. In: *International Journal of Hydrogen Energy* 34.21. DOI: 10.1016/j.ijhydene.2009.08.045, pp. 8877–8891.

Al-Janabi, Abdullah, Ghassan Al-Hajri, and Tariq Al-Maashani (2021). “Investigate the technical-economical feasibility of utilizing the available industrial waste thermal energy in Oman”. In: *Thermal Science and Engineering Progress* 21. DOI: 10.1016/j.tsep.2020.100778, p. 100778.

Amadeo, N. E. and M. A. Laborde (1995). “Hydrogen production from the low-temperature water-gas shift reaction: kinetics and simulation of the industrial reactor”. In: *International journal of hydrogen energy* 20.12. DOI: 10.1016/0360-3199(94)00130-R, pp. 949–956.

Appl, M. (1999). *Ammonia: principles and industrial practice.* Weinheim, Germany: Wiley-VCH.

ASME (2013). *Boiler & Pressure Vessel Code. VIII Rules for Construction of Pressure vessels.* American Society of Mechanical Engineers.

Badr, O., S. D. Probert, and P. W. O’callaghan (1985). “Selecting a working fluid for a Rankine-cycle engine”. In: *Applied Energy* 21.1. DOI: 10.1016/0306-2619(85)90072-8, pp. 1–42.

Banerjee, S. et al. (2013). “Technoeconomic analysis of biofuel production and biorefinery operation utilizing geothermal energy”. In: *Energy & Fuels* 27.3. DOI: 10.1021/ef301898n, pp. 1381–1390.

Bao, J. and L. Zhao (2013). “A review of working fluid and expander selections for organic Rankine cycle”. In: *Renewable and sustainable energy reviews* 24. DOI: 10.1016/j.rser.2013.03.040, pp. 325–342.

Bartholomew, Calvin H. and Robert J. Farrauto (2006). *Fundamentals of Industrial Catalytic Processes*. second ed. John Wiley & Sons, New York.

Bell, Ian H. et al. (2014). “Pure and Pseudo-pure Fluid Thermophysical Property Evaluation and the Open-Source Thermophysical Property Library CoolProp”. In: *Industrial*

& Engineering Chemistry Research 53.6. DOI: 10.1016/j.ijhydene.2008.08.039, pp. 2498–2508.

Bergman, Theodore L. et al. (2011). *Introduction to heat transfer*. Sixth Ed. John Wiley & Sons.

Bird, R. B., W. E. Stewart, and E. N. Lightfoot (2002). *Transport Phenomena*. Second Edition. John Wiley & Sons, Inc.

Braimakis, Konstantinos and Sotirios Karellas (2018). “Energetic optimization of regenerative Organic Rankine Cycle (ORC) configurations”. In: *Energy Conversion and Management* 159. DOI: 10.1016/j.enconman.2017.12.093, pp. 353–370.

Casci, Corrado et al. (1981). “Heat recovery in a ceramic kiln with an organic Rankine cycle engine”. In: *Journal of Heat Recovery Systems* 1.2. DOI: 10.1016/0198-7593(81)90027-8, pp. 125–131.

Çengel, Yunus A.. and Michael A. Boles (2007). *Thermodynamics: An Engineering Approach*. McGraw-Hill Higher Education.

Chanson, Hubert (1996). *Air Bubble Entrainment in Free-Surface Turbulent Shear Flows*. Chapter 12 - Air Entrainment in Partially-Filled Conduits. Academic Press.

Chen, Wei-Hsin et al. (2008). “Modeling and simulation of hydrogen generation from high-temperature and low-temperature water gas shift reactions”. In: *International Journal of Hydrogen Energy* 33.22. DOI: 10.1016/j.ijhydene.2008.08.039, pp. 6644–6656.

Chevron-Phillips (2018). *Cyclopentane - Material Safety Data Sheet*. `http://www.cpchem.com/msds/100000014138_SDS_US_EN.PDF`. (accessed 21 August 2019).

Choi, Yongtaek and Harvey G Stenger (2003). “Water gas shift reaction kinetics and reactor modeling for fuel cell grade hydrogen”. In: *Journal of Power Sources* 124.2. DOI: 10.1016/S0378-7753(03)00614-1, pp. 432–439.

Ding, OL and SH Chan (2008). “Water–gas shift reaction–A 2-D modeling approach”. In: *international journal of hydrogen energy* 33.16. DOI: 10.1016/j.ijhydene.2008.05.087, pp. 4325–4336.

Dong, Ying (2018). “Modeling Chemistry and Flow in Catalytic Fixed-Bed Reactors with Detailed Geometry”. PhD thesis. Technischen Universitat Hamburg. Hamburg, Germany.

Drescher, Ulli and Dieter Brüggemann (2007). “Fluid selection for the Organic Rankine Cycle (ORC) in biomass power and heat plants”. In: *Applied thermal engineering* 27.1. DOI: 10.1016/j.applthermaleng.2006.04.024, pp. 223–228.

Eggeman, T (2010). *Ammonia. Kirk-Othmer Encyclopedia of Chemical Technology*. 1–33.

EIA (2019). *Average Price of Electricity to Ultimate Customers by End-Use Sector*. `https://www.eia.gov/electricity/monthly/epm_table_grapher.php?t=epmt_5_6_a`. (accessed 26 August 2019).

Eigenberger, Gerhart and Wilhelm Ruppel (2012). “Catalytic Fixed-Bed Reactors”. In: *Ullmann’s Encyclopedia of Industrial Chemistry.*

Elnashaie, S. S. E. H. and Elshishini (1994). *Modelling, simulation and optimization of industrial fixed bed catalytic reactors.* Ed. by R. Hughes. Vol. 7. Topics in Chemical Engineering. Gordon and Breach Science.

Feng, Huijun et al. (2020). “Power and efficiency optimizations of an irreversible regenerative organic Rankine cycle”. In: *Energy Conversion and Management* 220. DOI: 10.1016/j.enconman.2020. p. 113079.

Fierro, José J et al. (2021). “Techno-economic assessment of a rotary kiln shell radiation waste heat recovery system”. In: *Thermal Science and Engineering Progress* 23. DOI: 10.1016/j.tsep.2021.100858, p. 100858.

Finkel, Daniel E. (2003). “DIRECT optimization algorithm user guide”. In: *Center for Research in Scientific Computation, North Carolina State University*, pp. 1–14.

Finlayson, Bruce A. (1980). *Nonlinear analysis in chemical engineering.* Chemical Engineering Series. McGraw-Hill.

Fisher (2009). *Hexamethyldisiloxane - Material Safety Data Sheet.* `https://www.fishersci.com/store/msds?partNumber=AC194790100&productDescription=HEXAMETHYLDISILOXANE+98+10ML&vendorId=VN00032119&countryCode=US&language=en`. (accessed 15th July 2021).

— (2014). *Ethanol - Material Safety Data Sheet.* `https://beta-static.fishersci.com/content/dam/fishersci/en_US/documents/programs/education/regulatory-documents/sds/chemicals/chemicals-e/S25309.pdf`. (accessed 21 August 2019).

— (2015a). *Methanol - Material Safety Data Sheet.* `https://beta-static.fishersci.com/content/dam/fishersci/en_US/documents/programs/education/regulatory-documents/sds/chemicals/chemicals-m/S25426A.pdf`. (accessed 21 August 2019).

— (2015b). *Pentane - Material Safety Data Sheet.* `https://beta-static.fishersci.com/content/dam/fishersci/en_US/documents/programs/education/regulatory-documents/sds/chemicals/chemicals-p/S25457.pdf`. (accessed 21 August 2019).

Francesconi, Javier A, Miguel C Mussati, and Pio A Aguirre (2007). “Analysis of design variables for water-gas-shift reactors by model-based optimization”. In: *Journal of Power Sources* 173.1. DOI: 10.1021/ie101137b, pp. 467–477.

Froment, Gilbert F., Kenneth B. Bischoff, and Juray De Wilde (2011). *Chemical Reactor Analysis and Design.* third ed. John Wiley & Sons Inc.

Giunta, P., N. Amadeo, and M. Laborde (2006). “Simulation of a low temperature water gas shift reaction using the heterogeneous model/application to a PEM fuel cell”. In: *Journal of Power Sources* 156. DOI: 10.1016/j.jpowsour.2005.04.036, pp. 489–496.

Gleinser, Moritz and Christoph Wieland (2016). "The misselhorn cycle: batch-evaporation process for efficient low-temperature waste heat recovery". In: *Energies* 9.5. DOI: 10.3390/en9050337, p. 337.

Hla, S. S. et al. (2011). "Investigation into the performance of a Co–Mo based sour shift catalyst using simulated coal-derived syngases". In: *International Journal of Hydrogen Energy* 36.11. DOI: 10.1016/j.ijhydene.2011.02.075, pp. 6638–6645.

Hunt, M. L. and C. L. Tien (1988). "Non-Darcian convection in cylindrical packed beds". In: *Journal of Heat Transfer* 110.2. DOI: 10.1115/1.3250495, pp. 378–384.

Imran, Muhammad et al. (2014). "Thermo-economic optimization of Regenerative Organic Rankine Cycle for waste heat recovery applications". In: *Energy Conversion and Management* 87. DOI: 10.1016/j.enconman.2014.06.091, pp. 107–118.

Insider (2019). *Natural Gas: Historical prices.* `https://markets.businessinsider.com/commodities/historical-prices/natural-gas-price/usd/1.1.2009_29.8.2019`. (accessed 29 August 2019).

Iordanidis, A. A. (2002). "Mathematical Modeling of Catalytic Fixed Bed Reactors". PhD thesis. University of Twente. URL: `https://ris.utwente.nl/ws/portalfiles/portal/6073612/t0000040.pdf`.

IPPC (2007). *Reference Document on Best Available Techniques for the Manufacture of Large Volume Inorganic Chemicals – Ammonia, Acids and Fertilisers.* Technical Report. `http://eippcb.jrc.ec.europa.eu/reference/BREF/lvic_aaf.pdf`. (accessed 24 September 2018). Integrated Pollution Prevention and Control. European Commission.

Jenkins, Scott (2019). *Chemical Engineering Plant Cost Index: 2018 Annual value.* `https://www.chemengonline.com/2019-cepci-updates-january-prelim-and-december-2018-final/`. (accessed 26 August 2019).

Jones, Donald R, Cary D Perttunen, and Bruce E Stuckman (1993). "Lipschitzian optimization without the Lipschitz constant". In: *Journal of Optimization Theory and Applications* 79.1. DOI: 10.1007/BF00941892, pp. 157–181.

Keiski, Riitta L, Tapio Salmi, and Veikko J Pohjola (1992). "Development and verification of a simulation model for a non-isothermal water-gas shift reactor". In: *The Chemical Engineering Journal* 48.1. DOI: 10.1016/0300-9467(92)85003-R, pp. 17–29.

Kern, Donald Quentin (1965). *Process heat transfer.* International Ed. McGraw-Hill New York.

Landelle, Arnaud et al. (2017). "Organic Rankine cycle design and performance comparison based on experimental database". In: *Applied energy* 204. DOI: 10.1016/j.apenergy.2017.04.012, pp. 1172–1187.

Lee, Ho Yong and Kyoung Hoon Kim (2015). “Energy and exergy analyses of a combined power cycle using the organic rankine cycle and the cold energy of liquefied natural gas”. In: *Entropy* 17.9. DOI: 10.3390/e17096412, pp. 6412–6432.

Leonzio, Grazia (2020). “Mathematical modeling of a methanol reactor by using different kinetic models”. In: *J. Ind. Eng. Chem.* 85. DOI: 10.1016/j.jiec.2020.01.033, pp. 120–140.

Liu, Bo-Tau, Kuo-Hsiang Chien, and Chi-Chuan Wang (2004). “Effect of working fluids on organic Rankine cycle for waste heat recovery”. In: *Energy* 29.8. DOI: 10.1016/j.energy.2004.01.004, pp. 1207–1217.

Mago, Pedro J et al. (2008). “An examination of regenerative organic Rankine cycles using dry fluids”. In: *Applied thermal engineering* 28.8-9. DOI: 10.1016/j.applthermaleng.2007.06.025, pp. 998–1007.

Maizza, V. and A. Maizza (2001). “Unconventional working fluids in organic Rankine-cycles for waste energy recovery systems”. In: *Applied thermal engineering* 21.3. DOI: 10.1016/S1359-4311(00)00044-2, pp. 381–390.

Marín, Pablo, Fernando V Díez, and Salvador Ordóñez (2012). “Fixed bed membrane reactors for WGSR-based hydrogen production: Optimisation of modelling approaches and reactor performance”. In: *International journal of hydrogen energy* 37.6. DOI: 10.1016/j.ijhydene.2011.12.027, pp. 4997–5010.

Markatos, N. C. et al. (2005). “Membrane reactor modelling: A comparative study to evaluate the role of combined mass and heat dispersion in large-scale adiabatic membrane modules”. In: *Chemical Engineering Research and Design* 83.10. DOI: 10.1205/cherd.04299, pp. 1171–1178.

Martinez, O. M., S. I. Pereira Duarte, and N. O. Lemcoff (1985). “Modeling of fixed bed catalytic reactors”. In: *Computers & chemical engineering* 9.5. DOI: 10.1016/0098-1354(85)80028-4, pp. 535–545.

Maxwell, Charles (2021). *Cost Indices.* `https://www.toweringskills.com/financial-analysis/cost-indices/`. (accessed 24 June 2021).

Mendes, Diogo et al. (2010). “Determination of the low-temperature water- gas shift reaction kinetics using a Cu-based catalyst”. In: *Industrial & Engineering Chemistry Research* 49.22. DOI: 10.1021/ie101137b, pp. 11269–11279.

Moe, J. M. (1962). “Design of water gas shift reactors”. In: *Chemical Engineering Progress* 58, pp. 33–36.

Moran, Michael J et al. (2011). *Fundamentals of engineering thermodynamics.* Seventh Edition. John Wiley & Sons.

Muhammad, Usman et al. (2015). “Design and experimental investigation of a 1 kW organic Rankine cycle system using R245fa as working fluid for low-grade waste heat recovery from steam". In: *Energy Conversion and Management* 103. DOI: 10.1016/j.enconman.2015.07.045, pp. 1089–1100.

Nauman, E Bruce (2008). *Chemical reactor design, optimization, and scaleup.* John Wiley & Sons.

Nguyen, TQ, JD Slawnwhite, and K Goni Boulama (2010). "Power generation from residual industrial heat". In: *Energy Conversion and Management* 51.11. DOI: 10.1016/j.enconman.2010.03.016, pp. 2220–2229.

Nguyen, V. M., P. S. Doherty, and S. B. Riffat (2001). "Development of a prototype low-temperature Rankine cycle electricity generation system". In: *Applied Thermal Engineering* 21.2. DOI: 10.1016/S1359-4311(00)00052-1, pp. 169–181.

Papageorgiou, JN and GF Froment (1995). "Simulation models accounting for radial voidage profiles in fixed-bed reactors". In: *Chemical Engineering Science* 50.19. DOI: 10.1016/0009-2509(95)00 pp. 3043–3056.

Pasel, J et al. (2005). "Test of a water–gas-shift reactor on a 3 kWe-scale—design points for high-and low-temperature shift reaction". In: *Journal of power sources* 152. DOI: 10.1016/j.jpowsour.2004.12.051, pp. 189–195.

Payscale (2021). *Average Process Technician Hourly Pay.* `https://www.payscale.com/research/US/Job=Process_Technician/Hourly_Rate`. (accessed 24 June 2021).

Peris, Bernardo et al. (2015). "Experimental study of an ORC (organic Rankine cycle) for low grade waste heat recovery in a ceramic industry". In: *Energy* 85. DOI: 10.1016/j.energy.2015.03.065, pp. 534–542.

Perry, Robert H. and Don W Green (1999). *Perry's chemical engineers'.* 7th Edition. McGraw Hill.

Pili, Roberto et al. (2017). "Techno-economic analysis of waste heat recovery with ORC from fluctuating industrial sources". In: *Energy Procedia* 129. DOI: 10.1016/j.egypro.2017.09.170, pp. 503–510.

Plaza, A et al. (2016). "Apparent kinetics of the catalyzed water–gas shift reaction in synthetic wood gas". In: *Chemical Engineering Journal* 301. DOI: 10.1016/j.cej.2016.04.152, pp. 222–228.

Poling, Bruce E., John M. Prausnitz, and John P. O'connell (2001). *The properties of gases and liquids.* 5th Edition. Mcgraw-hill New York.

Quoilin, Sylvain (2011). "Sustainable Energy Conversion Through the Use of Organic Rankine Cycles for Waste Heat Recovery and Solar Applications". PhD thesis. Aerospace and Mechanical Engineering Department. University of Liegè. Belgium.

Rase, Howard F (1990). *Fixed-bed reactor design and diagnostics: gas-phase reactions.* Butterworth-Heinemann.

Rase, Howard F. and James R. Holmes (1977). *Chemical reactor design for process plants.* Vol. 2. John Wiley & Sons, New York.

Roetzel, Wilfried and Bernhard Spang (2010). *VDI Heat Atlas.* Ed. by Peter Stephan. 2nd Edition. Part C3. Springer-Verlag Berlin Heidelberg. ISBN: 978-3-540-77877-6.

Saeidi, Samrand et al. (2017). "Hydrogen production: Perspectives, separation with special emphasis on kinetics of WGS reaction: A state-of-the-art review". In: *Journal of Industrial and Engineering Chemistry* 49. DOI: 10.1016/j.jiec.2016.12.003, pp. 1–25.

Saleh, Bahaa et al. (2007). "Working fluids for low-temperature organic Rankine cycles". In: *Energy* 32.7. DOI: 10.1016/j.energy.2006.07.001, pp. 1210–1221.

Scaccabarozzi, Roberto et al. (2018). "Comparison of working fluids and cycle optimization for heat recovery ORCs from large internal combustion engines". In: *Energy* 158. DOI: 10.1016/j.energy.2018.06.017, pp. 396–416.

Secchi, Argimiro R. (2019). *Receita do método de aproximação polinomial global aplicados a problemas unidimensionais sem simetria.* `http://www2.peq.coppe.ufrj.br/Pessoal/Professores/Arge/COQ862`. (accessed 2 April 2019).

Seider, Warren D., J.D. Seader, and Daniel R. Lewin (2003). *Product and Process Design Principles.* second ed. John Wiley & Sons, New York.

Seider, Warren D. et al. (2016). *Product and Process Design Principles: Synthesis Analysis and Evaluation.* fourth ed. John Wiley & Sons, New York.

Sigma-Aldrich (2015). *Diethylether - Material Safety Data Sheet.* `http://dept.harpercollege.edu/chemistry/sds/Diethyl%20ether.pdf`. (accessed 21 August 2019).

Sinnott, Raymond K. (2005). *Chemical engineering design.* Vol. 6. Coulson & Richardson's Chemical Engineering. Elsevier Butterworth-Heinemann Oxford.

Smirniotis, Panagiotis G. and Gunugunur K. Reddy (2015). *Water Gas Shift Reaction: Research Developments and Applications.* Elsevier.

Smith, Byron, Muruganandam Loganathan, and Murthy Shekhar Shantha (2010). "A review of the water gas shift reaction kinetics". In: *International Journal of Chemical Reactor Engineering* 8.1.

Smith, Joseph M., Hendrick C. Van Ness, and Michael M. Abbott (2007). *Introdução à termodinâmica da engenharia química.* 7th edition. Rio de Janeiro, Brasil: LTC.

Smith, Joseph Mauk (1970). *Chemical engineering kinetics.* 2nd Edition. McGraw-Hill.

Smith, Robin (2005). *Chemical process: design and integration.* John Wiley & Sons.

Souza, Renata N C de (2013). *Estudo e Simulação do Processo de Gaseificação.* Trabalaho de conclusão de curso. Escola de Química, Universidade Federal do Rio de Janeiro (EQ/UFRJ).

Stryjek, R and JH Vera (1986). “PRSV: An improved Peng—Robinson equation of state for pure compounds and mixtures”. In: *The canadian journal of chemical engineering* 64.2, pp. 323–333.

Sun, Jian and Wenhua Li (2011). “Operation Optimization Of An Organic Rankine Cycle (orc) Heat Recovery Power Plant”. In: *Applied Thermal Engineering* 31.11-12. DOI: 10.1016/j.applthermaleng.2011.03.012, pp. 2032–2041.

Sun, Qingxuan et al. (2020). “Thermodynamic and economic optimization of a double-pressure organic Rankine cycle driven by low-temperature heat source”. In: *Renewable Energy* 147. DOI: 10.1016/j.renene.2018.11.093, pp. 2822–2832.

Tchanche, Bertrand Fankam et al. (2009). “Fluid selection for a low-temperature solar organic Rankine cycle”. In: *Applied Thermal Engineering* 29.11-12. DOI: 10.1016/j.applthermaleng.2008.12.025, pp. 2468–2476.

TEMA (2007). *Standards of the tubular exchanger manufacturers association.* Ninth Ed. Tubular exchanger manufacturers association Inc.

Tester, J. W. and M. Modell (1997). *Thermodynamics and Its Applications.* Ed. by N. R. Amundson. 3rd. Prentice Hall PTR, New Jersey, USA.

Tian, Zhen et al. (2020). “Thermo-economic analysis and optimization of a combined Organic Rankine Cycle (ORC) system with LNG cold energy and waste heat recovery of dual-fuel marine engine”. In: *International Journal of Energy Research* 44.13. DOI: 10.1002/er.5529, pp. 9974–9994.

Tiemersma, T. P. et al. (2006). “Modelling of packed bed membrane reactors for autothermal production of ultrapure hydrogen”. In: *Chemical Engineering Science* 61.5. DOI: 10.1016/j.ces.2005.10.004, pp. 1602–1616.

Towler, Gavin and Raymond K Sinnott (2012). *Chemical engineering design: principles, practice and economics of plant and process design.* second ed. Elsevier, New York.

Tsotsas, Evangelos (2010). *VDI Heat Atlas.* Ed. by Peter Stephan. 2nd Edition. Part M7. Springer-Verlag Berlin Heidelberg. ISBN: 978-3-540-77877-6.

Turton, Richard et al. (2012). *Analysis, synthesis and design of chemical processes.* fourth ed. Pearson Education, New York.

Ulrich, G. D. and P. T. Vasudevan (2006). “How to estimate utility costs”. In: *Chemical Engineering* 113.4, p. 66.

Vélez, Fredy et al. (2012). “A technical, economical and market review of organic Rankine cycles for the conversion of low-grade heat for power generation”. In: *Renewable and Sustainable Energy Reviews* 16.6. DOI: 10.1016/j.rser.2012.03.022, pp. 4175–4189.

Villadsen, John and Michael L. Michelsen (1978). *Solution of differential equation models by polynomial approximation.* Prentice-Hall, Inc.

Vortmeyer, D., P. Wagner, and E. Haidegger (1992). “The interaction between temperature and flow in wall-cooled catalytic fixed-bed reactors”. In: *Chemical Engineering Science* 47.5. DOI: 10.1016/0009-2509(92)80256-C, pp. 1325–1328.

Wang, Huarong et al. (2015). “Organic Rankine cycle saves energy and reduces gas emissions for cement production”. In: *Energy* 86. DOI: 10.1016/j.energy.2015.03.112, pp. 59–73.

Wei, Donghong et al. (2007). “Performance analysis and optimization of organic Rankine cycle (ORC) for waste heat recovery”. In: *Energy conversion and Management* 48.4. DOI: 10.1016/j.enconman.2006.10.020, pp. 1113–1119.

Welty, James R et al. (2001). *Fundamentals of momentum, heat, and mass transfer*. 4th Edition. John Wiley & Sons.

Whiting, Larry F. and Peter W. Carr (1977). “A simple, fast numerical method for the solution of a wide variety of electrochemical diffusion problems”. In: *Journal of Electroanalytical Chemistry and Interfacial Electrochemistry* 81.1. DOI: 10.1016/S0022-0728(77)80355-0, pp. 1–20.

Wolpert, JL and SB Riffat (1996). “Solar-powered Rankine system for domestic applications”. In: *Applied Thermal Engineering* 16.4. DOI: 10.1016/1359-4311(95)00032-1, pp. 281–289.

Yamamoto, Takahisa et al. (2001). “Design and testing of the organic Rankine cycle”. In: *Energy* 26.3. DOI: 10.1016/S0360-5442(00)00063-3, pp. 239–251.

Yu, Haoshui, Xiao Feng, and Yufei Wang (2016). “Working fluid selection for organic Rankine cycle (ORC) considering the characteristics of waste heat sources”. In: *Industrial & Engineering Chemistry Research* 55.5. DOI: 10.1021/acs.iecr.5b02277, pp. 1309–1321.

ZP (2021a). *Dimensions and weights of seamless tubes*. `https://www.steeltube.sk/zelpo/vyrobky.nsf/Tab5UK?OpenPage`. (accessed 15th July 2021).

— (2021b). *Seamless tubes for heat exchangers*. `https://www.steeltube.sk/for-heat-exchangers/`. (accessed 15th July 2021).

Part IV

Appendix

Appendix A

Discrete Models

A.1 Catalyst Particle

Before applying any discretization technique, it is good practice to make the main model variables entirely dimensionless to facilitate its resolution. Therefore, the following dimensionless variables are introduced in the catalyst particle model: the particle radius $\left(x = \frac{r}{d_\mathrm{p}/2}\right)$, the temperature $\left(\theta = \frac{T}{T_\mathrm{ref}}\right)$ and the concentration $\left(C_i^* = \frac{C_i}{C_\mathrm{ref}}\right)$. The subscript "ref" identifies a reference value. Introducing the proposed changes, assuming that the diffusion coefficient derivative is negligible $\left(\frac{\mathrm{d}\mathscr{D}_{\mathrm{eff},i}}{\mathrm{d}r} \approx 0\right)$ and rewriting Eqs. 4.2.1 and 4.2.2, one can promptly obtain:

$$\mathscr{D}_{\mathrm{eff},i}\left(\frac{2}{x}\frac{\mathrm{d}C_i^*}{\mathrm{d}x} + \frac{\mathrm{d}^2C_i^*}{\mathrm{d}x^2}\right) + \left(\frac{d_\mathrm{p}}{2}\right)^2 \frac{\nu_i r_\mathrm{int}}{C_\mathrm{ref}} = 0 \tag{A.1.1}$$

$$\frac{\mathrm{d}C_i^*}{\mathrm{d}x}\Big|_{x=0} = 0 \qquad \frac{-2\mathscr{D}_{\mathrm{eff},i}|_{x=1}}{d_\mathrm{p}}\frac{\mathrm{d}C_i^*}{\mathrm{d}x}\Big|_{x=1} = \frac{\kappa_i}{C_\mathrm{ref}}\left(C_i|_{x=1} - C_{\mathrm{f},i}\right)$$

$$\frac{2}{x}\frac{\mathrm{d}\theta}{\mathrm{d}x} + \frac{\mathrm{d}^2\theta}{\mathrm{d}x^2} + \left(\frac{d_\mathrm{p}}{2}\right)^2 \frac{(-\Delta_\mathrm{r}h)}{\lambda_\mathrm{eff}T_\mathrm{ref}} r_\mathrm{int} = 0 \tag{A.1.2}$$

$$\frac{\mathrm{d}\theta}{\mathrm{d}x}\Big|_{x=0} = 0 \qquad \frac{-2\lambda_\mathrm{eff}}{d_\mathrm{p}}\frac{\mathrm{d}\theta}{\mathrm{d}x}\Big|_{x=1} = \frac{h}{T_\mathrm{ref}}\left(T|_{x=1} - T_\mathrm{f}\right)$$

The catalyst particle model after discretization by OC is represented in Eq. A.1.3 and A.1.4.

$$\mathscr{D}_{\mathrm{eff},k}\left(\frac{2}{x_i}\sum_{j=1}^{n+2} A_{i,j}C_{j,k}^* + \sum_{j=1}^{n+2} B_{i,j}C_{j,k}^*\right) + \left(\frac{d_\mathrm{p}}{2}\right)^2 \frac{\nu_k r_{\mathrm{int},i}}{C_\mathrm{ref}} = 0 \tag{A.1.3}$$

$$\text{B.C.:} \quad \sum_{j=1}^{n+2} A_{1,j} C^*_{j,k} = 0 \qquad \frac{-2\mathscr{D}_{\text{eff},k}|_{x=1}}{d_\text{p}} \sum_{j=1}^{n+2} A_{n+2,j} C^*_{j,k} = \frac{\kappa_k}{C_\text{ref}} \left(C_k|_{x=1} - C_{\text{f},k} \right)$$

$$i = 2, ..., n+1 \quad k = \text{H}_2,\ \text{CO},\ \text{CO}_2,\ \text{H}_2\text{O},\ \text{N}_2 \text{ and } \text{CH}_4$$

$$\frac{2}{x_i} \sum_{j=1}^{n+2} A_{i,j} \theta_j + \sum_{j=1}^{n+2} B_{i,j} \theta_j + \left(\frac{d_\text{p}}{2} \right)^2 \frac{(-\Delta_\text{r} h_i)}{\lambda_\text{eff} T_\text{ref}} r_{\text{int},i} = 0 \tag{A.1.4}$$

$$\text{B.C.:} \quad \sum_{j=1}^{n+2} A_{1,j} \theta_j = 0 \qquad \frac{-2\lambda_\text{eff}}{d_\text{p}} \sum_{j=1}^{n+2} A_{n+2,j} \theta_j = \frac{h}{T_\text{ref}} \left(T|_{x=1} - T_\text{f} \right)$$

$$i = 2, ..., n+1$$

A.2 Reactor

A.2.1 Momentum Balance

In the momentum balance Eq. 4.4.3, the dimensionless radial coordinate $\left(x = \frac{r}{R} \right)$ and velocity $\left(\omega = \frac{v}{v_{ref}} \right)$ are set and OC is applied in the radial coordinate, yielding the following discrete equation:

$$\begin{aligned} 0 = & \frac{\mu_\text{f}}{\varepsilon_i R^2} \left(\frac{1}{x_i} \sum_{j=1}^{n+2} A_{i,j} \omega_j + \sum_{j=1}^{n+2} B_{i,j} \omega_j \right) + \frac{\rho_\text{f} g_z}{v_{ref}} - \frac{1}{v_{ref}} \frac{\partial P}{\partial z} \\ & - \frac{150 \left(1 - \varepsilon\right)^2 \mu_\text{f} \omega_i}{\varepsilon_i^3 d_\text{p}^2} - \frac{1.75 \left(1 - \varepsilon\right) v_{ref} \omega_i^2 \rho_\text{f}}{\varepsilon_i^3 d_\text{p}} \end{aligned} \tag{A.2.1}$$

$$\text{B.C.:} \quad \sum_{j=1}^{n+2} A_{1,j} \omega_j = 0 \qquad \omega|_{r=R} = 0$$

$$i = 2, ..., n+1$$

where v_{ref} is the reference velocity (m·s^{-1}) and R is the reactor tube radius (m).

A.2.2 Energy Balance

The discrete energy balance is obtained after setting the dimensionless variables ($x = \frac{r}{R}$, $\zeta = \frac{z}{L}$, $\tau = \frac{t}{t_\text{ref}}$ and $\theta = \frac{T}{T_\text{ref}}$), applying forward first order finite differences to approximate the first order derivatives in the axial coordinate and the thermal conductivity coefficients derivatives; applying central second order finite differences to approximate the second order derivative in the axial coordinate and applying OC in the radial coordinate.

$$
\begin{aligned}
\frac{\partial \theta_{(j,i)}}{\partial \tau} = & \left(\frac{t_{\mathrm{ref}}}{\varepsilon_{(j)} C_{\mathrm{f}(j,i)} c_{p_{\mathrm{f}(j,i)}} + \left(1 - \varepsilon_{(j)}\right) \rho_{\mathrm{s}} c_{p_{\mathrm{s}}}} \right) \left\{ - \frac{C_{\mathrm{f}(j,i)} c_{p_{\mathrm{f}(j,i)}} v_{(j)}}{L} \left(\frac{\theta_{(j,i+1)} - \theta_{(j,i)}}{\Delta \zeta} \right) \dots \right. \\
& + \frac{1}{L^2} \left[\left(\frac{\lambda_{z(j,i+1)} - \lambda_{z(j,i)}}{\Delta \zeta} \right) \left(\frac{\theta_{(j,i+1)} - \theta_{(j,i)}}{\Delta \zeta} \right) \dots \right. \\
& \left. + \lambda_{z(j,i)} \left(\frac{\theta_{(j,i+1)} - 2\theta_{(j,i)} + \theta_{(j,i-1)}}{\Delta \zeta^2} \right) \right] \dots \\
& + \frac{1}{R^2} \left[\left(\frac{\lambda_{r(j,i+1)} - \lambda_{r(j,i)}}{x_{(j+1)} - x_{(j)}} \right) \sum_{j=1}^{NR+2} A_{(k,j)} \theta_{(j,i)} \dots \right. \\
& \left. + \frac{\lambda_{r(j,i)}}{x_{(j)}} \sum_{j=1}^{NR+2} A_{(k,j)} \theta_{(j,i)} + \lambda_{r(j,i)} \sum_{j=1}^{NR+2} B_{(k,j)} \theta_{(j,i)} \right] \dots \\
& \left. \frac{-v_{(j)} \theta_{(j,i)}}{C_{\mathrm{f}(j,i)} L} \left(\frac{\partial C_{\mathrm{f}}}{\partial T} \right)_{P(j,i)} \left(\frac{P_{(i+1)} - P_{(i)}}{\Delta \zeta} \right) + \frac{(-\Delta h_{\mathrm{r}})_{(j,i)} \left(1 - \varepsilon_{(j)}\right) \eta_{(j,i)}\, r_{\mathrm{int}(j,i)}}{T_{\mathrm{ref}}} \right\}
\end{aligned}
\tag{A.2.2}
$$

$$j = 2, ..., NR+1 \qquad i = 2, ..., NZ+1 \qquad k = 1, ..., NR+2$$

$$
\begin{aligned}
\text{B.C.1: } \left[c_{p_{\mathrm{f}}} T \frac{\dot{n}}{A_{\mathrm{t}}} + \frac{\dot{n} T}{A_{\mathrm{t}} C_{\mathrm{f}}^2} \left(\frac{\partial C_{\mathrm{f}}}{\partial T} \right) P \right]_{inlet} = & C_{\mathrm{f}(j,1)} c_{p_{\mathrm{f}(j,1)}} T_{\mathrm{ref}} \theta_{(j,1)} v_{(j)} - \frac{\lambda_{z(j,1)} T_{\mathrm{ref}}}{L} \left(\frac{\theta_{(j,2)} - \theta_{(j,1)}}{\Delta \zeta} \right) \\
& + v_{(j)} \frac{T_{\mathrm{ref}} \theta_{(j,1)}}{C_{\mathrm{f},(j,1)}} \left(\frac{\partial C_{\mathrm{f}}}{\partial T} \right)_{P(j,1)} P_1
\end{aligned}
$$

$$j = 1, ..., NR+2$$

$$\text{B.C.2: } \theta_{(j,NZ+2)} - \theta_{(j,NZ+1)} = 0 \qquad j = 1, ..., NR+2$$

$$\text{B.C.3: } \sum_{j=1}^{NR+2} A_{(1,j)} \theta_{(j,i)} = 0 \qquad i = 2, ..., NZ+1$$

$$\text{B.C.4: } \sum_{j=1}^{NR+2} A_{(NR+2,j)} \theta_{(j,i)} = \ddot{q} \qquad i = 2, ..., NZ+1$$

A.2.3 Material Balance

The discrete mass balnace is obtained after setting the dimensionless variables ($x = \frac{r}{R}$, $\zeta = \frac{z}{L}$, $\tau = \frac{t}{t_{\text{ref}}}$ and $C^* = \frac{C_l}{C_{l,\text{ref}}}$), applying forward first order finite differences to approximate the first order derivatives in the axial coordinate and the diffusion coefficients derivatives; applying central second order finite differences to approximate the second order derivative in the axial coordinate and applying OC in the radial coordinate.

$$\begin{aligned}\frac{1}{t_{\text{ref}}}\frac{\partial C^*_{l(j,i)}}{\partial \tau} = & -\frac{v_{(j)}}{L}\left(\frac{C^*_{l(j,i+1)} - C^*_{l(j,i)}}{\Delta\zeta}\right) + \frac{1}{L^2}\left[\left(\frac{D_{z(j,i+1)} - D_{z(j,i)}}{\Delta\zeta}\right)\left(\frac{C^*_{l(j,i+1)} - C^*_{l(j,i)}}{\Delta\zeta}\right)\dots\right.\\ & \left. + D_{z(j,i)}\left(\frac{C^*_{l(j,i+1)} - 2C^*_{l(j,i)} + C^*_{l(j,i-1)}}{\Delta\zeta^2}\right)\right]\dots\\ & + \frac{1}{R^2}\left[\left(\frac{D_{r(j,i+1)} - D_{r(j,i)}}{x_{(j+1)} - x_{(j)}}\right)\sum_{j=1}^{NR+2} A_{(k,j)}C^*_{l(j,i)}\dots\right.\\ & \left. + \frac{D_{r(j,i)}}{x_{(j)}}\sum_{j=1}^{NR+2} A_{(k,j)}C^*_{l(j,i)} + D_{r(j,i)}\sum_{j=1}^{NR+2} B_{(k,j)}C^*_{l(j,i)}\right]\dots\\ & + \frac{\nu_l\left(1-\varepsilon_{(j)}\right)\eta_{(j,i)}\,r_{\text{int}(j,i)}}{C_{\text{ref}}}\end{aligned} \tag{A.2.3}$$

$j = 2, ..., NR+1 \quad i = 2, ..., NZ+1 \quad k = 1, ..., NR+2 \quad l =$ H_2, CO, CO_2, H_2O, N_2 and CH_4

$$\text{B.C.1: } \left[\frac{\dot{n}_i}{A_{\text{t}}}\right]_{inlet} = C_{l(j,1)}v_{(j)} - \frac{C_{\text{ref}}D_{z(j,1)}}{L}\frac{C^*_{l(j,2)} - C^*_{l(j,1)}}{\Delta\zeta} \quad j = 1, ..., NR+2$$

$$\text{B.C.2: } C^*_{l(j,NZ+2)} - C^*_{l(j,NZ+1)} = 0 \qquad j = 1, ..., NR+2$$

$$\text{B.C.3: } \sum_{j=1}^{NR+2} A_{(1,j)}C^*_{l(j,i)} = 0 \qquad i = 2, ..., NZ+1$$

$$\text{B.C.4: } \sum_{j=1}^{NR+2} A_{(NR+2,j)}C^*_{l(j,i)} = 0 \qquad i = 2, ..., NZ+1$$

Appendix B

Thermodynamic and Physical Properties

B.1 Diffusion Coefficient

B.1.1 Catalyst Particle

The effective diffusion of the jth component inside the catalyst particle ($\mathscr{D}_{\text{eff}}$)(m^2·s^{-1}) is calculated according to Eq. B.1.1 (Perry and Green, 1999).

$$\mathscr{D}_{\text{eff}_j} = 1 \times 10^{-4} \frac{\varepsilon_{\text{p}}}{\gamma} D_{j,e} \tag{B.1.1}$$

where ε_{p} and γ are the catalyst particle void fraction (0.55) and the tortuosity (5) (Adams II and Barton, 2009). $D_{j,e}$ (cm^2·s^{-1}) is calculated by Eq. B.1.2 as a resistance in series between the Knudsen diffusion (D_{K}) (cm^2·s^{-1}) (Eq. B.1.3) and the diffusion of the jth component in the fluid mixture ($D_{\text{m},j}$) (cm^2·s^{-1}), which is calculated by the Wilke correlation (Eq B.1.4) (Welty et al., 2001).

$$\frac{1}{D_{j,e}} = \frac{1}{D_{\text{K},j}} + \frac{1}{D_{\text{m},j}} \tag{B.1.2}$$

$$D_{\text{K},j} = 4850 d_{\text{p}} \sqrt{\frac{T}{M_j}} \tag{B.1.3}$$

$$D_{\text{m},j} = \frac{1}{\sum\limits_{i \neq j}^{NC} \frac{y_i}{D_{ji}}} \tag{B.1.4}$$

where M is the molecular weight (kg·kmol^{-1}), d_{pore} is the pore diameter (cm), T must be in K and y_i is the mole fraction of the ith component on a component-j-free basis. D_{ji} is the binary diffusion coefficient calculated by the Fuller, Schettler, and Giddings correlation (cm^2·s^{-1}) (Eq. B.1.5) (Welty et al., 2001).

$$D_{ji} = \frac{1 \times 10^{-3} T^{1.75} \left(\frac{1}{M_j} + \frac{1}{M_i}\right)^{0.5}}{P\left[(\sum V)_j^{1/3} + (\sum V)_i^{1/3}\right]^2} \tag{B.1.5}$$

where P must be in atm and T must be in K. The diffusion volumes ($\sum V$) for the components considered in this work are given in Table B.1.

Table B.1: Diffusion volumes (Welty et al., 2001).

Component	Diffusion volume ($\sum V$)
H_2	6.12
N_2	17.9
CO	18.9
CO_2	26.9
H_2O	12.7
CH_4	25.14

B.2 Mass Transfer Coefficient

For spherical particles, *Sh* can be calculated by the Wakao correlation (Eq. B.2.2) (Iordanidis, 2002).

$$Sh = \frac{\kappa\, d_{\mathrm{p}}}{D_{j,m}} \tag{B.2.1}$$

$$Sh = 2 + 1.1 Re^{0.6} Sc^{0.33} \tag{B.2.2}$$

where d_{p} is the catalyst particle diameter (m), Re is the Reynolds number $\left(Re = \frac{\rho_{\mathrm{f}} v_0 d_{\mathrm{p}}}{\mu_{\mathrm{f}}}\right)$, Sc is the Schmidt number $\left(Sc = \frac{\mu_{\mathrm{f}}}{\rho_{\mathrm{f}} D_{\mathrm{m},j}}\right)$ and μ is the viscosity (Pa·s).

B.3 Fluid Viscosity

The fluid viscosity μ_f (Pa s) of a gas mixture is estimated by the Lucas method (Eq. B.3.1) (Poling et al., 2001).

$$\mu_\mathrm{f} = 1 \times 10^{-7} \frac{Z_2 F_\mathrm{P} F_\mathrm{Q}}{\xi} \tag{B.3.1}$$

where Z_2 is a factor estimated by Eq. B.3.2, F_Q (Eq. B.3.3) and F_P (Eq. B.3.4) are correction factors for quantum effects and polarity, respectively. ξ (Eq. B.3.5) is the reduced inverse viscosity (μPa^{-1}).

$$\begin{gathered}
Z_2 = 0.6 + 0.76 P_\mathrm{r,m}^{\alpha} + \left(6.99 P_\mathrm{r,m}^{\beta} - 0.6\right)\left(1 - T_\mathrm{r,m}\right) \qquad T_\mathrm{r,m} \leq 1 \\
\alpha = 3.262 + 14.98 P_\mathrm{r,m}^{5.508} \\
\beta = 1.39 + 5.746 P_\mathrm{r,m} \\
Z_2 = Z_1 \left(1 + \frac{a P_\mathrm{r,m}^{e}}{b P_\mathrm{r,m}^{f} + \left(1 + c P_\mathrm{r,m}^{d}\right)^{-1}}\right) \qquad 1 < T_\mathrm{r,m} \leq 40 \\
a = \left(\frac{1.245 \times 10^{-3}}{T_\mathrm{r,m}}\right) \exp\left(5.1726 T_\mathrm{r,m}^{-0.3286}\right) \\
b = a \left(1.6553 T_\mathrm{r,m} - 1.2723\right) \\
c = \left(\frac{0.4489}{T_\mathrm{r,m}}\right) \exp\left(3.0578 T_\mathrm{r,m}^{-37.7332}\right) \\
d = \left(\frac{1.7368}{T_\mathrm{r,m}}\right) \exp\left(2.231 T_\mathrm{r,m}^{-7.6351}\right) \\
e = 1.3088 \\
f = 0.9425 \exp\left(-0.1853 T_\mathrm{r,m}^{0.4489}\right)
\end{gathered} \tag{B.3.2}$$

$$F_\mathrm{Q} = \frac{1 + \left(F_\mathrm{Q,m}^{0} - 1\right)\left(Y^{-1} - 0.007\ [\ln(Y)]^4\right)}{F_\mathrm{Q,m}^{0}} \tag{B.3.3}$$

$$F_\mathrm{P} = \frac{1 + \left(F_\mathrm{P,m}^{0} - 1\right) Y^{-3}}{F_\mathrm{P,m}^{0}} \tag{B.3.4}$$

$$\xi = 0.176 \left(\frac{T_\mathrm{c,m}}{M_\mathrm{m}^{3} P_\mathrm{c,m}^{4}}\right)^{1/6} \tag{B.3.5}$$

where the subscript "m" refers to the mixture, $Y = \frac{Z_2}{Z_1}$, $T_{\mathrm{r,m}}$ and $P_{\mathrm{r,m}}$ are the reduced temperature and reduced pressure, respectively. $T_{\mathrm{r,m}}$ and $P_{\mathrm{r,m}}$ are calculated based on the critical properties of the mixture, namely, $T_{\mathrm{c,m}}$ (Eq. B.3.7) and $P_{\mathrm{c,m}}$(Eq. B.3.8).

$$Z_1 = \left(0.807T_{\mathrm{r,m}}^{0.618} - 0.357\exp\left(-0.449T_{\mathrm{r,m}}\right) + 0.34\exp\left(-4.058T_{\mathrm{r,m}}\right) + 0.018\right) F_{\mathrm{P,m}}^0 F_{\mathrm{Q,m}}^0 \tag{B.3.6}$$

$$T_{\mathrm{c,m}} = \sum_{i=1}^{NC} y_i T_{\mathrm{c},i} \tag{B.3.7}$$

$$P_{\mathrm{c,m}} = 10T_{\mathrm{c,m}}R\frac{\sum\limits_{i=1}^{NC} y_i Z_{\mathrm{c},i}}{\sum\limits_{i=1}^{NC} y_i V_{\mathrm{c},i}} \tag{B.3.8}$$

where $F_{\mathrm{P,m}}^0$ and $F_{\mathrm{Q,m}}^0$ are calculated by Eq. B.3.9 and B.3.10, respectively. The components critical properties are available at Table B.2 along with other relevant parameters. The dimension of the variables presented in Table B.2 shall not be altered while using the equations in this subsection.

$$F_{\mathrm{P,m}}^0 = \sum_{i=1}^{NC} y_i F_{\mathrm{P},i}^0 \tag{B.3.9}$$

$$F_{\mathrm{Q,m}}^0 = \left(\sum_{i=1}^{NC} y_i F_{\mathrm{Q},i}^0\right) A \tag{B.3.10}$$

where $A = 1 - 0.01\left(\frac{M_H}{M_L}\right)$ if the ratio between the molecular weight of the heavier compound and the lighter compound $\left(\frac{M_H}{M_L}\right)$ is greater than 9. Otherwise $A = 1$. $F_{\mathrm{P},i}^0$ is calculated according to Eq. B.3.11 and $F_{\mathrm{Q},i}^0$ is calculated according to Eq. B.3.12. $F_{\mathrm{Q},i}^0$ is calculated only for H_2, He and D_2. For other elements, it is equal to 1.

$$F_{\mathrm{P},i}^0 = 1 \qquad 0 \leq RDM < 0.0222$$

$$F_{\mathrm{P},i}^0 = 1 + 30.55\left(0.292 - Z_{\mathrm{c},i}\right)^{1.72} \qquad 0.0222 \leq RDM < 0.075 \tag{B.3.11}$$

$$F_{\mathrm{P},i}^0 = 1 + 30.55\left(0.292 - Z_{\mathrm{c},i}\right)^{1.72} \left|0.96 + 0.1\left(T_{\mathrm{r},i} - 0.7\right)\right| \qquad 0.075 \leq RDM$$

$$F^0_{\mathrm{Q},i} = 1.1708\left(1 + 0.00385\left(\left(T_{\mathrm{r},i} - 12\right)^2\right)^{(1/M_i)} \operatorname{sign}\left(T_{\mathrm{r},i} - 12\right)\right) \tag{B.3.12}$$

where RDM is the reduced dipole moment (Eq. B.3.13) and $\operatorname{sign}\left(T_{\mathrm{r},i} - 12\right)$ means that only the sign of the mathematical operation between the brackets must be considered.

$$RDP = 52.46\frac{DM_i^2 P_{\mathrm{c},i}}{T^2_{\mathrm{c},i}} \tag{B.3.13}$$

Table B.2: Parameters used for fluid viscosity and fluid thermal conductivity calculation (Poling et al., 2001).

Component	M (g mol^{-1})	T_c (K)	V_c (cm^3 mol^{-1})	P_c (bar)	Z_c	DM (debye)	ω
H_2	2.016	33.25	65	12.97	0.305	0	-0.216
CO	28.01	132.85	193.1	34.94	0.292	0.1	0.045
CO_2	44.01	304.12	94.07	73.74	0.274	0	0.225
H_2O	18.015	647.14	55.95	220.64	0.229	1.8	0.344
N_2	28.014	126.2	90.1	33.98	0.289	0	0.037
CH_4	16.043	190.56	98.6	45.99	0.286	0	0.011

B.4 Fluid Thermal Conductivity

The fluid thermal conductivity of gas mixture is calculated using firstly the mixing rules proposed by Stiel and Thodos (from Eq. B.4.1 to Eq. B.4.10) (Poling et al., 2001).

$$V_{\mathrm{c},ij} = \frac{\left(V^{1/3}_{\mathrm{c},i} + V^{1/3}_{\mathrm{c},j}\right)^3}{8} \tag{B.4.1}$$

$$V_{\mathrm{c},ii} = V_{\mathrm{c},i} \tag{B.4.2}$$

$$T_{\mathrm{c},ij} = \left(T_{\mathrm{c},i}T_{\mathrm{c},j}\right)^{0.5} \tag{B.4.3}$$

$$T_{\mathrm{c},ii} = T_{\mathrm{c},i} \tag{B.4.4}$$

$$V_{\mathrm{c,m}} = \sum_{i=1}^{NC}\sum_{j=1}^{NC} y_i y_j V_{\mathrm{c},ij} \tag{B.4.5}$$

$$M_{\mathrm{m}} = \sum_{i=1}^{NC} y_i M_i \tag{B.4.6}$$

$$\omega_{\mathrm{m}} = \sum_{i=1}^{NC} y_i \omega_i \tag{B.4.7}$$

$$Z_{\mathrm{c,m}} = 0.291 - 0.08\omega_{\mathrm{m}} \tag{B.4.8}$$

$$P_{\mathrm{c,m}} = \frac{Z_{\mathrm{c,m}} R T_{\mathrm{c,m}}}{V_{\mathrm{c,m}}} \tag{B.4.9}$$

$$T_{\mathrm{c,m}} = \left(\sum_{i=1}^{NC}\sum_{j=1}^{NC} y_i y_j V_{\mathrm{c},ij} T_{\mathrm{c},ij}\right) V_{\mathrm{c,m}}^{-1} \tag{B.4.10}$$

Using the mixing rules presented above, the thermal conductivity of the fluid at low pressure (λ_{m}^{0}) can be estimated using Chung's correlation (Eq. B.4.11) (Poling et al., 2001). In Eq. B.4.11 all variables are in SI units, however, M_{m} must be in kg mol^{-1}. The mixture viscosity at low pressure (μ_{m}^{0}) is found by dividing Z_1 (Eq. B.3.6) by ξ (Eq. B.3.5) and multiplying by 1×10^{7} to convert from μP to Pa s.

$$\frac{\lambda_{\mathrm{m}}^{0} M_{\mathrm{m}}}{\mu_{\mathrm{m}}^{0} c_{v,\mathrm{m}}} = \frac{3.75\Psi}{c_{v,\mathrm{m}}/R_{\mathrm{g}}} \tag{B.4.11}$$

where $c_{v,\mathrm{m}}$ is the ideal gas mixture specific heat at constant volume ($c_{v,\mathrm{m}} = c_{p,\mathrm{m}} - R_{\mathrm{g}}$). Values for$c_p$ are given in Table B.3. Ψ is found by Eq. B.4.12.

Table B.3: Ideal gas specific heat at constant pressure coefficients ($T_{\mathrm{reference}} = 298.15\mathrm{K}$). $c_p = R_{\mathrm{g}}\left(a_0 + a_1 T + a_2 T^2 + a_3 T^3 + a_4 T^4\right)$ (Poling et al., 2001).

Component	a_0 (K^0)	$a_1 \times 10^3$ (K^{-1})	$a_2 \times 10^5$ (K^{-2})	$a_3 \times 10^8$ (K^{-3})	$a_4 \times 10^{11}$ (K^{-4})
H_2	2.883	3.681	-0.772	0.692	-0.213
CO	3.912	-3.913	1.182	-1.302	0.515
CO_2	3.259	1.356	1.502	-2.374	1.056
H_2O	4.395	-4.186	1.405	-1.564	0.632
N_2	3.539	-0.261	0.007	0.157	-0.099
CH_4	4.568	-8.975	3.631	-3.407	1.091

$$\Psi = 1 + \alpha\left(\left(0.215 + 0.28288\alpha - 1.061\beta + 0.26665\varphi\right)/\left(0.6366 + \beta\varphi + 1.061\alpha\beta\right)\right) \qquad \text{(B.4.12)}$$

where $\alpha = (c_{v,\mathrm{m}}/R) - 1.5$, $\beta = 0.7862 - 0.7109\omega_{\mathrm{m}} + 1.3168\omega_{\mathrm{m}}^2$ and $\varphi = 2 + 10.5T_{\mathrm{r,m}}^2$. At pressures higher than atmospheric, λ_{f} can be found through the correlations proposed by Stiel and Thodos (Eq. B.4.13) (Poling et al., 2001).

$$\left(\lambda_{\mathrm{f}} - \lambda_{\mathrm{m}}^0\right)\Gamma Z_{\mathrm{c,m}}^5 = 1.22 \times 10^{-2}\left(\exp\left(0.535\rho_{\mathrm{r,m}}\right) - 1\right) \qquad \rho_{\mathrm{r,m}} < 0.5$$

$$\left(\lambda_{\mathrm{f}} - \lambda_{\mathrm{m}}^0\right)\Gamma Z_{\mathrm{c,m}}^5 = 1.14 \times 10^{-2}\left(\exp\left(0.67\rho_{\mathrm{r,m}}\right) - 1.069\right) \qquad 0.5 \leq \rho_{\mathrm{r,m}} < 2 \qquad \text{(B.4.13)}$$

$$\left(\lambda_{\mathrm{f}} - \lambda_{\mathrm{m}}^0\right)\Gamma Z_{\mathrm{c,m}}^5 = 2.6 \times 10^{-3}\left(\exp\left(1.155\rho_{\mathrm{r,m}}\right) + 2.016\right) \qquad 2 \leq \rho_{\mathrm{r,m}} < 2.8$$

where $\Gamma = 210\left(\frac{T_{\mathrm{c,m}}M_{\mathrm{m}}^3}{P_{\mathrm{c,m}}^4}\right)^{(1/6)}$ and $\rho_{\mathrm{r,m}}$ is the mixture reduced molar density.

B.5 Concentration Variation with Temperature at Constant Pressure

The term $\left(\frac{\partial C_{\mathrm{f}}}{\partial T}\right)_P$ is estimated using PRSV-EoS as follows:

$$\left(\frac{\partial C_{\mathrm{f}}}{\partial T}\right)_P = \frac{\frac{A'_m C_{\mathrm{f}}^2}{1+2bC_{\mathrm{f}}-\left(bC_{\mathrm{f}}\right)^2} - \frac{C_{\mathrm{f}}^2 R\mathrm{g}}{C_{\mathrm{f}}-C_{\mathrm{f}}^2 b}}{\frac{2C_{\mathrm{f}} R\mathrm{g} T}{C_{\mathrm{f}}-C_{\mathrm{f}}^2 b} - \frac{C_{\mathrm{f}}^2 R\mathrm{g} T}{\left(C_{\mathrm{f}}-C_{\mathrm{f}}^2 b\right)^2} + 2\frac{C_{\mathrm{f}}^3 b R\mathrm{g} T}{\left(C_{\mathrm{f}}-C_{\mathrm{f}}^2 b\right)^2} - 2\frac{A_m C_{\mathrm{f}}}{1+2bC_{\mathrm{f}}-(bc)^2} + 2\frac{bC_{\mathrm{f}}^2-b^2C_{\mathrm{f}}^3}{\left[1+2bC_{\mathrm{f}}-(bc)^2\right]^2}} \tag{B.5.1}$$

A_m is given by Eq. B.5.2 and its derivative by Eq. B.5.3. b is the same as defined in Stryjek and Vera (1986).

$$A_m = \sum_{i=1}^{NC}\sum_{j=1}^{NC} y_i y_j \left[\sqrt{a_i a_j}\,(1-k_{ij})\right] \tag{B.5.2}$$

$$\begin{aligned} &\text{if}\,, \quad A'_m = \sum_{i=1}^{NC}\sum_{j=1}^{NC} y_i y_j \left\{\frac{0.5\left(a'_i a_j - a_i a'_j\right)}{\sqrt{a_i a_j}} - \left[\frac{0.5\left(a'_i a_j - a_i a'_j\right)k_{ij}}{\sqrt{a_i a_j}} + \sqrt{a_i a_j}\,k'_{ij}\right]\right\} \\ &\text{else} \qquad \frac{\mathrm{d}A_m}{\mathrm{d}T} = \sum_{i=1}^{NC}\sum_{j=1}^{NC} y_i y_j \left[\frac{0.5(1-k_{ij})\left(a'_i a_j - a_i a'_j\right)}{\sqrt{a_i a_j}}\right] \end{aligned} \tag{B.5.3}$$

where a is the same as defined in Stryjek and Vera (1986), $k_{i,j}$ is the binary interaction parameter, which were retrieved from Aspen Hysys v10 database.

B.6 Real Gas c_p

The following deduction is based on Poling et al. (2001) and Smith et al. (2007). It starts by defining that the enthalpy is a function of the temperature and pressure ($H = f\,(T, P)$). The partial derivative of this function yields:

$$\mathrm{d}H = \left(\frac{\partial H}{\partial T}\right)_P \mathrm{d}T + \left(\frac{\partial H}{\partial P}\right)_T \mathrm{d}P \tag{B.6.1}$$

Since $H = U + PV$:

$$\mathrm{d}H = \mathrm{d}U + V\mathrm{d}P + P\mathrm{d}V \tag{B.6.2}$$

Inserting Eq. B.6.2 into Eq. B.6.1 and considering the heat capacity at constant pressure definition ($c_p = \left(\frac{\partial H}{\partial T}\right)_P$) yields:

$$\mathrm{d}U + V\mathrm{d}P + P\mathrm{d}V = c_p\mathrm{d}T + \left(\frac{\partial H}{\partial P}\right)_T \mathrm{d}P \tag{B.6.3}$$

Considering that the internal energy is a function of the temperature and volume ($U = f(T, V)$), its partial derivative is:

$$\mathrm{d}U = \left(\frac{\partial U}{\partial T}\right)_V \mathrm{d}T + \left(\frac{\partial U}{\partial V}\right)_T \mathrm{d}V \tag{B.6.4}$$

Inserting Eq. B.6.4 into Eq. B.6.3 and considering the heat capacity at constant volume definition ($c_v = \left(\frac{\partial U}{\partial T}\right)_V$) yields:

$$c_v\mathrm{d}T + \left(\frac{\partial U}{\partial V}\right)_T \mathrm{d}V = c_p\mathrm{d}T + \left(\frac{\partial H}{\partial P}\right)_T \mathrm{d}P \tag{B.6.5}$$

Deriving the correlations $\mathrm{d}H = T\mathrm{d}S + V\mathrm{d}P$ and $\mathrm{d}U = T\mathrm{d}S - P\mathrm{d}V$ with respect to the pressure and the volume, respectively, yields:

$$\left(\frac{\partial H}{\partial P}\right)_T = T\left(\frac{\partial S}{\partial P}\right)_T + V \tag{B.6.6}$$

$$\left(\frac{\partial U}{\partial V}\right)_T = T\left(\frac{\partial S}{\partial V}\right)_T - P \tag{B.6.7}$$

By replacing Eq. B.6.6 and Eq. B.6.7 into Eq. B.6.5, the following equation is obtained:

$$c_v\mathrm{d}T + \left(T\left(\frac{\partial S}{\partial V}\right)_T - P\right)\mathrm{d}V = c_p\mathrm{d}T + \left(T\left(\frac{\partial S}{\partial P}\right)_T + V\right)\mathrm{d}P \tag{B.6.8}$$

It is known that the Gibbs energy ($\mathrm{d}G = -S\mathrm{d}T + V\mathrm{d}P$) and the Helmholtz energy ($\mathrm{d}A = -S\mathrm{d}T - P\mathrm{d}V$) are exact differentials. Therefore, the following Maxwell's relations are obtained:

$$-\left(\frac{\partial S}{\partial P}\right)_T = \left(\frac{\partial V}{\partial T}\right)_P \tag{B.6.9}$$

$$\left(\frac{\partial P}{\partial T}\right)_V = \left(\frac{\partial S}{\partial V}\right)_T \tag{B.6.10}$$

Introducing Eq. B.6.9 and Eq. B.6.10 into Eq. B.6.8 and rearranging it yields:

$$c_p = c_v + T\left(\frac{\partial V}{\partial T}\right)_P \left(\frac{\partial P}{\partial T}\right)_V \tag{B.6.11}$$

Considering the residual property definition, c_p can also be found by the following correlation:

$$c_p = c_p^{\mathrm{IG}} + c_p^{\mathrm{R}} \tag{B.6.12}$$

where the superscripts IG and R stand for ideal gas and residual, respectively. To obtain a useful form of the Eq. B.6.12, some algebraic arrangement must be performed as follows:

$$c_p = c_p^{\mathrm{IG}} - c_p^{\mathrm{IG}} + c_p \tag{B.6.13}$$

$$c_p = c_p^{\mathrm{IG}} - c_v^{\mathrm{IG}} - R_{\mathrm{g}} + c_p \tag{B.6.14}$$

$$c_p = c_p^{\mathrm{IG}} + (c_p - c_v) + c_v^{\mathrm{R}} - R_{\mathrm{g}} \tag{B.6.15}$$

Replacing the term $(c_p - c_v)$ by Eq. B.6.11 and the volume by the concentration $\left(C = \frac{1}{V}\right)$ yields:

$$c_p = c_p^{\mathrm{IG}} - R_{\mathrm{g}} + c_v^{\mathrm{R}} - \frac{T}{C^2}\left(\frac{\partial P}{\partial T}\right)_V \left(\frac{\partial C}{\partial T}\right)_P \tag{B.6.16}$$

The ideal gas heat capacity at constant pressure c_p^{IG} is obtained from Table.B.3, $\left(\frac{\partial P}{\partial T}\right)_V$ is calculated by Eq. B.6.17 from PRSV-EoS, and $\left(\frac{\partial C}{\partial T}\right)_P$ is calculated by Eq. B.5.1.

$$\left(\frac{\partial P}{\partial T}\right)_V = \frac{R_{\mathrm{g}}}{V - b} - \frac{A'_m}{V^2 + 2bV - b^2} \tag{B.6.17}$$

where the term A'_m is defined in Eq. B.5.3.

To calculate c_p in Eq. B.6.16, the term c_v^{R} still has to be determined. This is accomplished by replacing Eq. B.6.7 and Eq. B.6.10 into Eq. B.6.4. Thus:

$$\mathrm{d}U = c_v \mathrm{d}T + \left[T\left(\frac{\partial P}{\partial T}\right)_V - P\right]\mathrm{d}V \tag{B.6.18}$$

Since for an ideal gas $\mathrm{d}U = c_v \mathrm{d}T$, the last term in Eq. B.6.18 can only be the residual value. Therefore, by using the property of an exact differential, the c_v^{R} can be defined as:

$$c_v^{\mathrm{R}} = \int_{\infty}^{V} \left[T\left(\frac{\partial^2 P}{\partial T^2}\right)_V\right]_T \mathrm{d}V \tag{B.6.19}$$

where the term $\left(\frac{\partial^2 P}{\partial T^2}\right)_V$ is derived from PRSV-EoS and defined in Eq. B.6.20.

$$\left(\frac{\partial^2 P}{\partial T^2}\right)_V = -\frac{A''_m}{V^2 + 2bV - b^2} \tag{B.6.20}$$

Inserting Eq. B.6.20 into Eq. B.6.19 and solving the integral yields:

$$c_v^{\mathrm{R}} = -A''_m \left\{ \left[\frac{1}{\left(1-\sqrt{2}\right)b - \left(1+\sqrt{2}\right)b} \right] \ln \left[\frac{V + \left(1-\sqrt{2}\right)b}{V + \left(1+\sqrt{2}\right)b} \right] \right\} \tag{B.6.21}$$

where A''_m is the second derivative of A_m (Eq. B.5.2) with respect to the temperature. If the binary interaction parameters k_{ij} are temperature dependent, then:

$$\begin{aligned} A''_m = &\sum_{i=1}^{NC}\sum_{j=1}^{NC} y_i y_j \left\{ \frac{-0.25}{\left(a_i a_j\right)^{1.5}} \left(a'_i a_j + a_i a'_j\right)^2 + \frac{0.5}{\left(a_i a_j\right)^{0.5}} \left(a''_i a_j + 2a'_i a'_j + a - ia''_j\right) + \dots \right. \\ & - \left[\frac{-0.25 k_{ij}}{\left(a_i a_j\right)^{1.5}} \left(a'_i a_j + a_i a'_j\right)^2 + \frac{0.5 k_{ij}}{\left(a_i a_j\right)^{0.5}} \left(a''_i a_j + 2a'_i a'_j + a - ia''_j\right) + \dots \right. \\ & \left.\left. + \frac{k'_{ij}}{\left(a_i a_j\right)^{0.5}} \left(a'_i a_j + a_i a'_j\right) + \left(a_i a_j\right)^{0.5} k''_{ij} \right] \right\} \end{aligned} \tag{B.6.22}$$

If the binary interaction parameters k_{ij} are not temperature dependent, then:

$$A''_m = \sum_{i=1}^{NC}\sum_{j=1}^{NC} y_i y_j \left[\frac{-0.25\left(1-k_{ij}\right)}{\left(a_i a_j\right)^{1.5}} \left(a'_i a_j + a_i a'_j\right)^2 + \frac{0.5\left(1-k_{ij}\right)}{\left(a_i a_j\right)^{0.5}} \left(a''_i a_j + 2a'_i a'_j + a - ia''_j\right) \right] \tag{B.6.23}$$

B.7 Enthalpy of Reaction

The enthalpy of reaction ($\Delta_\mathrm{r} h$) is calculated according to Eq. B.7.1. The standard enthalpy of reaction ($\Delta_\mathrm{r} h^0$ at 289.15 K and 1 bar) is equal to -41.1 kJ·mol^{-1}. The ideal gas specific heat at constant pressure is available at Table B.3, and the residual enthalpy (h^R) is calculated according to Eq. B.7.2 (Tester and Modell, 1997).

$$\Delta_\mathrm{r} h = \Delta_\mathrm{r} h^0 + \int_{298.15}^{T} c_p^{\mathrm{IG}} \mathrm{d}T + h^\mathrm{R} \tag{B.7.1}$$

$$h^\mathrm{R} = \left(\frac{A_m - TA'_m}{2\sqrt{2}b}\right) \ln \left[\frac{V + \left(1-\sqrt{2}\right)b}{V + \left(1+\sqrt{2}\right)b} \right] + PV - RT \tag{B.7.2}$$

Appendix C

Orthogonal Collocation

Orthogonal Collocation (OC) is a numerical technique in which the solution of a differential equation is approximated by an orthogonal polynomial (for example, Eq. C.0.1) (Finlayson, 1980). The internal collocation points are defined as the roots of this polynomial so that the residuals at the collocation points are zero (Whiting and Carr, 1977).

$$y_i = P_n\left(x_i\right) \qquad i = 1, ..., n+2 \tag{C.0.1}$$

where n is the degree of the polynomial ($P(x)$), y is the dependent variable at the x_i collocation point.

In this work, the Shifted Legendre Polynomial (SLP) is used as interpolating polynomial. The SLP is a specific case of the Shifted Jacobi Polynomial (SJP) ($P_n^{\alpha,\beta}(x)$) with $\alpha = \beta = 0$, i.e., the weighting function is equal to unit. The SJP can be determined by Eq. C.0.2, where c_i are constants calculated using the orthogonality property (Eq. C.0.3) (Villadsen and Michelsen, 1978).

$$P_n^{\alpha,\beta}\left(x\right) = \sum_{i=0}^{n} c_i \left(-1\right)^{(n-1)} x^i \tag{C.0.2}$$

$$\int_0^1 W x^j P_n^{\alpha,\beta}\left(x\right) \mathrm{d}x = 0 \qquad j = 1, ..., n-1 \tag{C.0.3}$$

where W is the weighting function ($W = x^\beta \left(1-x\right)^\alpha$).

The derivatives of the dependent variable (y) can also be determined either by deriving Eq. C.0.1 or in matrix form as expressed by Eq. C.0.4 and C.0.5, respectively.

$$\frac{\mathrm{d}y_j}{\mathrm{d}x} = \frac{\mathrm{d}P_n\left(x_j\right)}{\mathrm{d}x} = \sum_{j=1}^{n+2} A_{i,j} y_j \tag{C.0.4}$$

$$\frac{\mathrm{d}^2 y_j}{\mathrm{d}x^2} = \frac{\mathrm{d}^2 P_n\left(x_j\right)}{\mathrm{d}x^2} = \sum_{j=1}^{n+2} B_{i,j} y_j \tag{C.0.5}$$

where A and B are matrices $(n+2, n+2)$ determined as follows (Finlayson, 1980):

(i) Set α, β and n and expand Eq. C.0.2;

(ii) Calculate c_i using Eq. C.0.3 and find the n roots of the polynomial (for example, by Newton-Raphson algorithm);

(iii) Expand Eq. C.0.1 and find the system $\mathbf{C} = \mathbf{X}^{-1}\mathbf{Y}$, which is shown below:

$$\begin{array}{cccc} \mathbf{Y} & & \mathbf{X} & \mathbf{C} \\ \begin{bmatrix} y_1 \\ y_2 \\ \vdots \\ y_{n+2} \end{bmatrix} & = & \begin{bmatrix} 1 & x_1 & x_1^2 & \cdots & x_1^n \\ 1 & x_2 & x_2^2 & \cdots & x_2^n \\ \vdots & \vdots & \vdots & \vdots & \vdots \\ 1 & x_{n+2} & x_{n+2}^2 & \cdots & x_{n+2}^n \end{bmatrix} & \begin{bmatrix} c_1 \\ c_2 \\ \vdots \\ c_{n+2} \end{bmatrix} \end{array} \tag{C.0.6}$$

(iv) Derive Eq. C.0.6 and replace $\mathbf{C}$ by $\mathbf{X}^{-1}\mathbf{Y}$ to find:

$$\frac{\mathrm{d}\mathbf{Y}}{\mathrm{d}x} = \frac{\mathrm{d}\mathbf{X}}{\mathrm{d}x}\mathbf{X}^{-1}\mathbf{Y} = \mathbf{A}_{(n+2,n+2)}\mathbf{Y}_{(n+2,1)} \tag{C.0.7}$$

(v) Derive Eq. C.0.6 twice and replace $\mathbf{C}$ by $\mathbf{X}^{-1}\mathbf{Y}$ to find:

$$\frac{\mathrm{d}^2\mathbf{Y}}{\mathrm{d}x^2} = \frac{\mathrm{d}^2\mathbf{X}}{\mathrm{d}x^2}\mathbf{X}^{-1}\mathbf{Y} = \mathbf{B}_{(n+2,n+2)}\mathbf{Y}_{(n+2,1)} \tag{C.0.8}$$

Another way to find c_i and the matrices $\mathbf{A}$ and $\mathbf{B}$ is by using recursion formulas such those shown elsewhere (Secchi, 2019).

Appendix D

Economic Analysis

D.1 Utilities Cost

The utilities cost are estimated by means of Eq. D.1.1 according to Ulrich and Vasudevan (2006). The fuel cost (C_{fuel}) is 3.19 US\$·GJ^{-1} (average since 2009) for natural gas as the primary fuel source (Insider, 2019). The 2018 average CEPCI is equal to 601.3 (Jenkins, 2019). Eq. D.1.1 constants are depicted in Table D.1.

$$C_{\text{utility}} = a_1(\text{CEPCI}) + a_2(C_{\text{fuel}}) \tag{D.1.1}$$

Table D.1: Parameters for utilities cost calculation.

Utilities	a_1	a_2	Range
Steam (US\$·kg^{-1})	$2,3 \times 10^{-5}\dot{m}^{-0,9}$	$0,0034P^{0,05}$	$1 < P < 46$ barg; $0,06 < \dot{m} < 40$ kg·s^{-1}
Cooling water (US\$·m^{-3})	$0,00007 + 2.5 \times 10^{-5}\dot{V}^{-1}$	0,003	$0,01 < \dot{V} < 10$ m^{3}s^{-1}

Appendix E

Results

E.1 Model Validation: Isothermal Operation

The effectiveness factor (η) was estimated so that a comparison between the experimental data of Choi and Stenger (2003) and the values predicted by the model developed in this work could be made. The results are shown in Eq. E.1.1 and in Fig.

$$\begin{aligned}\eta = &-1.6438 + 0.6659 y_{\mathrm{CO}} + 0.8017 y_{\mathrm{H_2O}} + 0.01226 T - 1.4219 \times 10^{-5} T^2 \\ &- 1.6582 \times 10^{-3} T y_{\mathrm{CO}} - 1.9971 \times 10^{-3} T y_{\mathrm{H_2O}}\end{aligned} \tag{E.1.1}$$

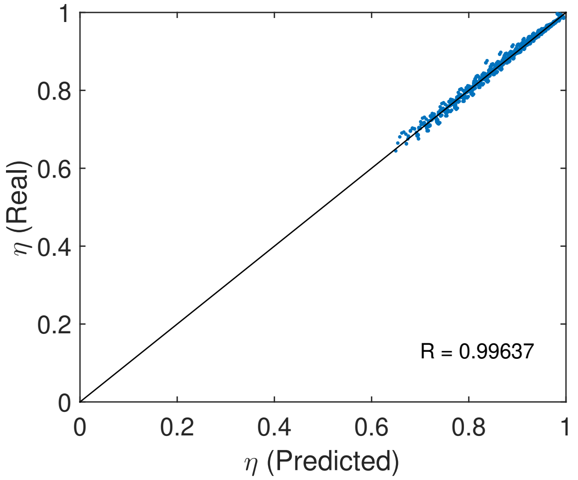

Figure E.1: Comparison between the predicted value of η by the proposed empiric model (Eq. E.1.1) with η calculated by Eq. 4.3.2

.

Appendix F

Fluid Film Coefficient and Pressure Drop Correlations

In this chapter, all equations used to estimate both the shell- and tube-side film coefficients (h), which are used to estimate the heat exchangers overall heat transfer coefficients are presented. Correlations used to estimate pressure drop (ΔP) are also presented. Fluid thermal conductivity (k (W·m^{-1}·K^{-1})), viscosity (μ (Pa·s)), mass specific heat capacity at constant pressure (c_p (J·kg^{-1}·K^{-1})) and density (ρ (kg·m^{-3})) are retrieved from the CoolProp 6.4.1 package. Reynolds and Prandtl numbers are defined in Eq. F.0.1 and Eq. F.0.2, respectively.

$$Re = \frac{\rho\, d\, v}{\mu} \tag{F.0.1}$$

$$Pr = \frac{c_p\, \mu}{k} \tag{F.0.2}$$

F.1 Single Phase: Tube-Side

The single-phase heat transfer coefficient is estimated by Eq. F.1.1. The tube internal diameter (d_{in}) should be used to calculate Re. μ_{w} is the fluid viscosity at the tube wall. The parameter C is equal to 0.021 for gases and 0.023 for liquids (Sinnott, 2005).

$$h = \left(\frac{k}{d_{\text{in}}}\right) C\, Re^{0.8} Pr^{0.33} \left(\frac{\mu}{\mu_{\text{w}}}\right)^{0.14} \tag{F.1.1}$$

The tube-side pressure drop (Pa) is estimated according to Eq. F.1.2, already considering 2.5 velocity heads due to contraction and expansions. L is the tube length (m), m is either equal to 0.25 for $Re < 2{,}100$ or equal to 0.14, and the j_f factor value depends on the Reynolds number as shown in Eq. F.1.3 (Sinnott, 2005).

$$\Delta P = \left[8 j_f \left(\frac{L}{d_{\text{in}}}\right) \left(\frac{\mu}{\mu_{\text{w}}}\right)^{-m} + 2.5\right] \frac{\rho v^2}{2} \tag{F.1.2}$$

$$\begin{aligned}
j_f &= 8.04472280\, Re^{-1.00066413} && 10 \leq Re < 100 \\
j_f &= 6.59026088\, Re^{-0.96691370} && 100 \leq Re < 1{,}000 \\
j_f &= 0.06262020\, Re^{-0.27977183} && 1{,}000 \leq Re < 10{,}000 \\
j_f &= 0.04267642\, Re^{-0.23829432} && 10{,}000 \leq Re < 100{,}000 \\
j_f &= 0.03109749\, Re^{-0.20999410} && 100{,}000 \leq Re \leq 1{,}000{,}000
\end{aligned} \tag{F.1.3}$$

F.2 Single Phase: Shell-Side

Both heat transfer coefficient (Eq. F.2.1) and pressure drop are calculated according to Kern's method (Kern, 1965; Sinnott, 2005). The equations presented in this section are for 25% baffle cut and 30° tube arrangement.

$$h = \left(\frac{k}{D_{\text{equ}}}\right) j_h\, Re Pr^{0.33} \left(\frac{\mu}{\mu_{\text{w}}}\right)^{0.14} \tag{F.2.1}$$

$$D_{\text{equ}} = \frac{4\, A_{\text{free}}}{0.5 \pi d_{\text{out}}} \tag{F.2.2}$$

$$A_{\text{free}} = 0.5\, S^2 \cos\left(\frac{\pi}{6}\right) - 0.125 \pi d_{\text{out}}^2 \tag{F.2.3}$$

where D_{equ} is the equivalent diameter (m) and j_h is a factor that depends on Re (Eq. F.2.4). d_{out} is the tube external diameter (m). The free-flow area (A_{free}) is calculated according to Eq. F.2.3 and S is the tube pitch ($1.25\, d_{\text{out}}$).

$$\begin{aligned}
j_h &= 0.76129008\, Re^{-0.59064041} && 10 \leq Re < 100 \\
j_h &= 0.40491433\, Re^{-0.45403545} && 100 \leq Re < 1{,}000 \\
j_h &= 0.62640383\, Re^{-0.50926370} && 1{,}000 \leq Re < 10{,}000 \\
j_h &= 0.37812975\, Re^{-0.45327416} && 10{,}000 \leq Re < 100{,}000 \\
j_h &= 0.57893001\, Re^{-0.48673003} && 100{,}000 \leq Re \leq 1{,}000{,}000
\end{aligned} \tag{F.2.4}$$

Re is based on D_{equ} and v, which is calculated based on the cross-flow area (A_{cross}).

$$v = \frac{\dot{m}}{A_{\text{cross}} \rho} \tag{F.2.5}$$

$$A_{\text{cross}} = \frac{D_{\text{shell, in}} S_b \left(S - d_{\text{out}}\right)}{S} \tag{F.2.6}$$

where S_b is the baffle spacing and $D_{\text{shell, in}}$ is the shell internal diameter.

$$D_{\text{shell,in}} = 1.02766722 \left[d_{\text{out}} \left(\frac{N_t}{0.319} \right)^{\left(\frac{1}{2.142}\right)} \right] + 0.0446806 \tag{F.2.7}$$

where N_t is the total number of tubes.

The shell-side pressure drop (Pa) is estimated according to Eq. F.2.8.

$$\Delta P = 8 j_f \left(\frac{D_{\text{shell, in}}}{D_{\text{equ}}} \right) \left(\frac{L}{S_b} \right) \left(\frac{\mu}{\mu_{\text{w}}} \right)^{-0.14} \frac{\rho\, v^2}{2} \tag{F.2.8}$$

$$\begin{aligned}
j_f &= 19.65431064\, Re^{-0.93918730} && 10 \leq Re < 100 \\
j_f &= 3.02140425\, Re^{-0.55802026} && 100 \leq Re < 1,000 \\
j_f &= 0.20084676\, Re^{-0.15148830} && 1,000 \leq Re < 10,000 \\
j_f &= 0.15882600\, Re^{-0.12759458} && 10,000 \leq Re < 100,000 \\
j_f &= 0.23565566\, Re^{-0.16281872} && 100,000 \leq Re \leq 1,000,000
\end{aligned} \tag{F.2.9}$$

F.3 Condensation: Shell-Side

The heat transfer coefficient for condensation outside vertical tubes is calculated according to Eq. F.3.1. The subscripts "liq" and "vap" stand for liquid and vapor phases, respectively. The tube loading (Γ) is calculated based on the condensate mass flow rate ($\dot{m}_{\text{condensate}}$) according to Eq. F.3.2 (kg m^{-1} s^{-1}) (Sinnott, 2005).

$$h = 0.926\, k_{\text{liq}} \left[\frac{\rho_{\text{liq}}\, g \left(\rho_{\text{liq}} - \rho_{\text{vap}}\right)}{\mu_{\text{liq}} \Gamma} \right]^{0.33} \tag{F.3.1}$$

$$\Gamma = \frac{\dot{m}_{\text{condensate}}}{N_t\, \pi\, d_{\text{in}}} \tag{F.3.2}$$

The shell-side pressure drop for condensation is taken as 50% of the single-phase pressure drop calculated based on the vapor phase properties (Sinnott, 2005).

F.4 Evaporation: Tube-Side

The heat transfer coefficient for evaporation inside vertical tubes is calculated according to Chen's method for forced-convection boiling (Eq. F.4.1) (Sinnott, 2005). It takes into account the effect of both forced-convection ($h_{\text{fc, cor}}$) and nucleate boiling ($h_{\text{nb, cor}}$). Each corrected by the respective factor (f_{fc} and f_{nb}).

$$h = h_{\text{fc, cor}} + h_{\text{nb, cor}} \tag{F.4.1}$$

$$h_{\text{fc, cor}} = h_{\text{fc}}\, f_{\text{fc}} \tag{F.4.2}$$

$$h_{\text{nb, cor}} = h_{\text{nb}}\, f_{\text{nb}} \tag{F.4.3}$$

h_{fc} is calculated considering that only the liquid phase is flowing, thus, it is estimated using the correlations presented in Sec. F.1. f_{fc} can be estimated using Eq. F.4.4. The parameter X_{tt} depends on the vapor fraction (x) and on the properties of both liquid ("liq") and vapor ("vap") phases (Eq. F.4.5).

$$f_{\text{fc}} = 4.601\times10^{-5}\left(\frac{1}{X_{tt}}\right)^3 - 9.87074\times10^{-3}\left(\frac{1}{X_{tt}}\right)^2 + 1.21896836\left(\frac{1}{X_{tt}}\right) + 1.19994673 \tag{F.4.4}$$

$$\frac{1}{X_{tt}} = \left(\frac{x}{1-x}\right)^{0.9}\left(\frac{\rho_{\text{liq}}}{\rho_{\text{vap}}}\right)^{0.5}\left(\frac{\mu_{\text{vap}}}{\mu_{\text{liq}}}\right)^{0.1} \tag{F.4.5}$$

h_{nb} is estimated by Mostinski's correlation (Eq. F.4.6) (Sinnott, 2005). P_c is the fluid's critical pressure (bar), P is the operating pressure (bar), T_{w} is the tube wall temperature (K) and T_{sat} is the fluid's saturation temperature (K) at the operating pressure.

$$h_{\text{nb}}^{0.3} = 0.104 P_c^{0.69}\left(T_{\text{w}} - T_{\text{sat}}\right)\left[1.8\left(\frac{P}{P_c}\right)^{0.17} + 4\left(\frac{P}{P_c}\right)^{1.2} + 10\left(\frac{P}{P_c}\right)^{10}\right] \tag{F.4.6}$$

f_{nb} depends both on f_{fc} and on Re_{liq} (Eq. F.4.7). Re_{liq} is the Reynolds number calculated based on the liquid phase, including the fluid flow velocity ($v_{\text{liq}} = v(1-x)$).

$$\begin{aligned} f_{\text{nb}} &= -0.22830319\ln\left(Re_{\text{liq}}\, f_{\text{fc}}^{1.25}\right) + 3.02398149 & 10^4 \le Re_{\text{liq}}\, f_{\text{fc}}^{1.25} < 4\times10^5 \\ f_{\text{nb}} &= 7.608339\times10^6\left(Re_{\text{liq}}\, f_{\text{fc}}^{1.25}\right)^{-1.40769749} & 4\times10^5 \le Re_{\text{liq}}\, f_{\text{fc}}^{1.25} \le 10^6 \end{aligned} \tag{F.4.7}$$

Pressure drop is estimated as the average between inlet and outlet values, obtained from the single-phase correlations.